DYNAMIC MODELING AND MODEL-FREE REAL-TIME OPTIMIZATION

FOR COLD CLIMATE HEAT PUMP SYSTEMS

by

Wenyi Wang

APPROVED BY SUPERVISORY COMMITTEE:

__________________________________________

Yaoyu Li, Chair

__________________________________________

Fatemeh Hassanipour

__________________________________________

Zhenpeng Qin

__________________________________________

Jie Zhang

To my beloved family

DYNAMIC MODELING AND MODL-FREE REAL-TIME OPTIMIZATION

FOR COLD CLIMATE HEAT PUMP SYSTEMS

by

WENYI WANG, BS, MS

DISSERTATION

Presented to the Faculty of

The University of Texas at Dallas

in Partial Fulfillment

of the Requirements

for the Degree of

DOCTOR OF PHILOSOPHY IN

MECHANICAL ENGINEERING

THE UNIVERSITY OF TEXAS AT DALLAS

December 2019

# ACKNOWLEDGMENTS

My sincere gratitude goes to my advisor Dr. Yaoyu Li, for his valuable guidance, understanding, patience and consistent support for my PhD study at The University of Texas at Dallas. Dr. Li's insightful view of optimal control and HVAC has helped me gain a deeper understanding in HVAC control. I truly appreciate that he showed me the way to a confident, independent and well-rounded researcher. I would also like to express my gratitude to Beijing Comfort Technology, Inc. for their substantial financial support.

I am also thankful for other members of my dissertation committee: Prof. Fatemeh Hassanipour, Prof. Zhenpeng Qin and Prof. Jie Zhang, for their precious time serving in my dissertation committee and providing valuable comments and inputs to my dissertation research.

Finally, I would like to thank all the members of the Energy System Controls Laboratory at The University of Texas at Dallas, for all their help and assistance during my PhD study.

August 2019

DYNAMIC MODELING AND MODEL-FREE REAL-TIME OPTIMIZAITION

FOR COLD CLIMATE HEAT PUMP SYSTEMS

Wenyi Wang, PhD
The University of Texas at Dallas, 2019

Supervising Professor: Yaoyu Li

Air source heat pump (ASHP) has been a well-received technology to provide space and/or water heating for building and industrial applications, while its efficiency and heating capacity can be severely limited when operated in cold climate. Various modifications have been proposed for cold-climate operation of ASHP over the single-stage refrigeration cycle, such as vapor injection techniques and cascade configuration. However, there has been a lack of effective control strategies for such systems to maintain the optimal energy efficiency for operations across different combinations of ambient and load conditions. Previous work has paid great efforts in model based strategies, anchored on deriving system models with simulation and experimental testing. Such approaches can be prohibitively expensive due to the inherent nonlinear nature of refrigeration systems and unmeasurable equipment degradation.

This dissertation investigates on model-free control strategies for real-time efficiency optimization for several configurations of cold-climate ASHP, by use of Extremum Seeking Control (ESC). By utilizing periodic dither inputs for online gradient estimation, ESC bears significant robustness against process variation and external disturbance, which has proved to be more advantageous in handling the challenging applications like heating, ventilation and air conditioning (HVAC) systems. Three types of ASHP configurations are studied in this dissertation: the internal heat exchanger vapor injection, flash-tank vapor injection, and cascade configuration. For both vapor injection ASHP configurations, the intermediate pressure setpoint is optimized by standard ESC and Newton-based ESC based on the feedback of the total power consumption, with the constant heating load considered. For the cascade ASHP, multivariable ESC is designed to handle two operational scenarios: minimizing the total power for fixed heating capacity and maximizing the coefficient of performance (COP) for variable heating capacity. For the power based ESC, the manipulated inputs include the intermediate temperature, high temperature cycle superheat and low temperature cycle superheat; while for the COP based ESC, the high- and low-temperature cycle compressor speeds and evaporator fan mass flow rate are adopted as inputs. The proposed ESC strategies are evaluated with Modelica based dynamic simulation models of the three system configurations. Simulations have been conducted under both fixed and realistic ambient temperature profiles. The simulation results show good steady-state and transient performance of real-time efficiency optimization with the proposed strategies, in terms of tracking unknown and dynamic optimum settings.

TABLE OF CONTENTS

## LIST OF FIGURES

LIST OF TABLES

**CHAPTER 1**

**INTRODUCTION**

## 1.1 Overview of Air Source Heat Pump

Space and water heating in residential and commercial buildings is a basic need for operational and occupants' need, which is a major aspect of energy consumption. According to the survey from U.S. Energy Information Administration (EIA) [1], space and water heating accounts for nearly two-thirds of the U.S. home energy use, as shown in Figure 1.1. Although fossil fuels remain dominant for space and water heating for the nations with abundant supply of such resources, combustion based heating generally features low energy efficiency and undesirable emissions. Heat pump technology has been considered an effective, economic and environmentally more friendly alternative for space and water heating.

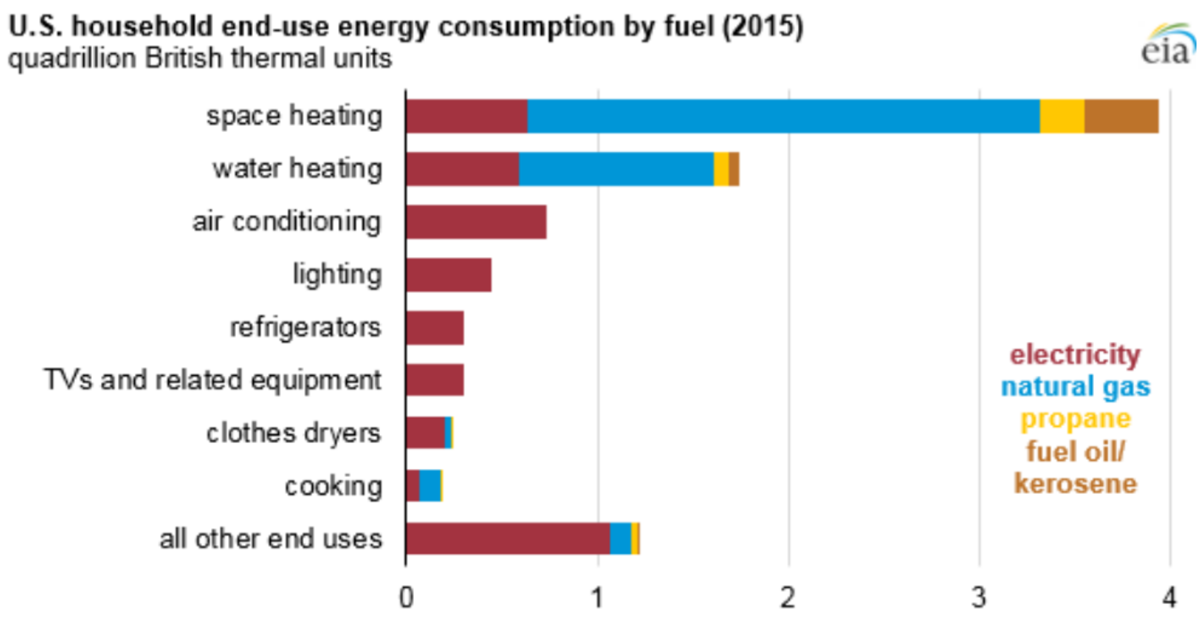


Figure 1.1. U.S. household end-use energy consumption by fuel (2015) [1].

In addition, heat pumps have provided an appealing category of sources of heating or preheating in various industrial applications, with substantial reduction in energy consumption and emissions, in the sectors of food and beverage processing, forest products, textiles and chemicals [2].

Over the past decades, the air source heat pump (ASHP) has become a major substitute for space and water heating for several advantages [3-5]:

1) The electrically driven ASHP can greatly improve the energy efficiency and reduce emissions than combustion of fossil fuels due to the commercially achievable coefficient of performance (COP).
2) Ease of installation and space saving. Comparing to the combustion heating and ground-source heat pump systems, ASHP is easier and cheaper to install, without any need for the fuel storage.
3) Long life-span and safe operation. ASHP is exceptionally reliable and steady source of heat, it can be operational for up to 20 years with proper care. There is no combustion involved and no fuels are required, so the operation of ASHP is very safe.

These merits have led to significant adoption of ASHP as residential buildings' heating source. The U.S. EIA estimated that [6], of the 11.8 million households in 2015 that used heat pumps in the U.S., 8.4 million (71%) were in the South. In Europe, the ASHP market is expected to exceed $7 billion by 2024 due to the ever-decreasing cost of manufacturing and maintenance [7]. In China [8], the ASHP market has observed an accelerating growth, having reached 12.8 billion RMB by 2016. Among these, a 57.8% year-over-year growth from 2015 to 2016 as shown in Figure 1.2.

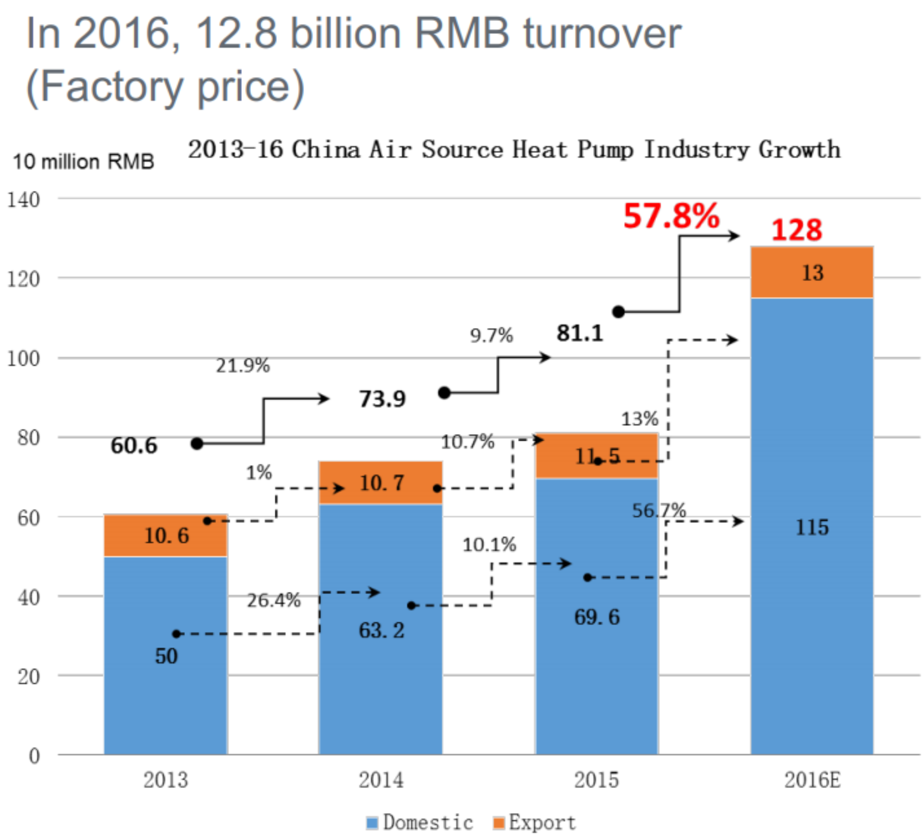


Figure 1.2. 2013-2016 China ASHP Industry Growth [8].

Figure 1.3 shows the schematic of a typical single-stage ASHP water heater, it consists of compressor, condenser, evaporator and an expansion valve. The refrigerant coming out from the expansion valve is low pressure, temperature liquid. Then it goes through the evaporator and turns into the low pressure, superheated vapor in the evaporator, in which the refrigerant absorbs heat through heat transfer with the ambient air. Then the low pressure, superheated vapor is compressed in the compressor to high pressure, temperature vapor, which pass through the condenser to release heat to the water going through the condenser in the other side. After releasing the heat, the refrigerant turns into the high pressure, supercooled liquid, and then pass through the expansion valve to finish a complete cycle.

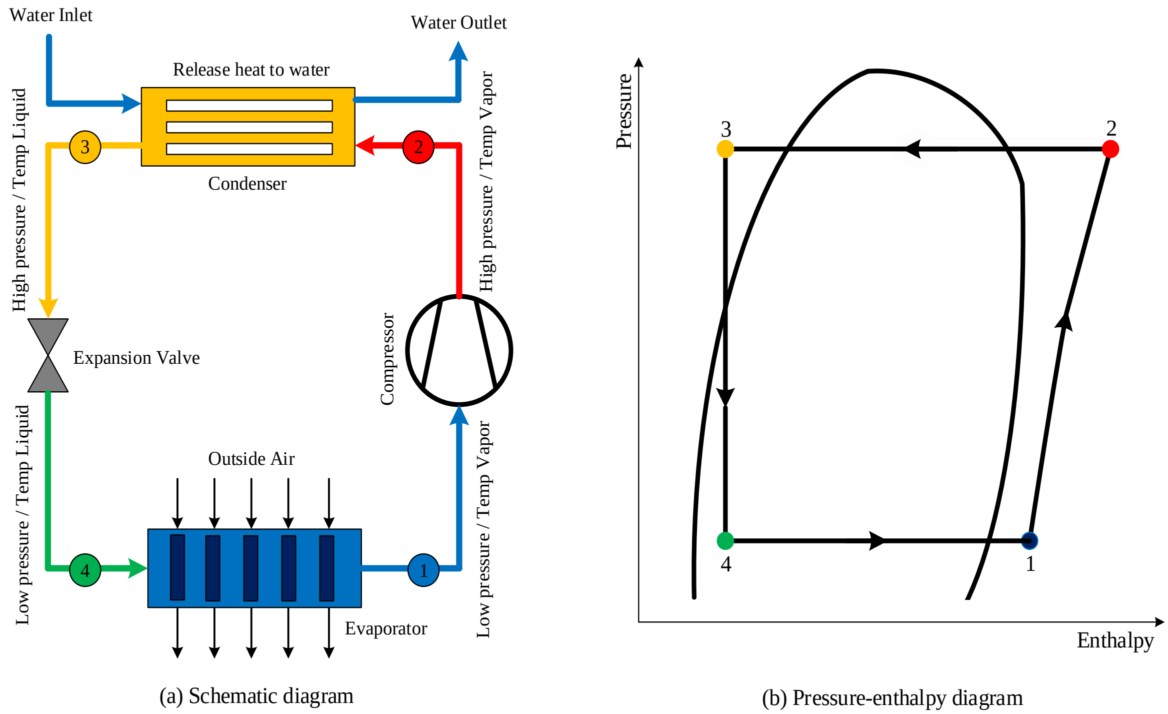


Figure 1.3. Schematic of a typical single-stage air source heat pump water heater.

In the community of heating, ventilation and air conditioning (HVAC), the 'cold climate' refers to that the ambient air temperature during the coldest month is between 0°C and –17.8°C, while the 'very cold climate' refers to the ambient air temperature between –17.8°C and –32 °C [9]. However, for the cold climate areas, the ramification and adoption of the ASHP has been greatly limited. Bertsch and Groll [10] pointed out four main problems for ASHP operated in cold climates:

1) The heating capacity can be insufficient under increasing heating demand. Due to the high pressure ratio of compressor operation, the resultant low refrigerant mass flow rates can significantly reduce the achievable heat pump capacity.

2) The compressor discharge temperature can be excessively high due to the low suction pressure and high pressure ratio across the compressor.

3) The COP can be greatly reduced under high pressure ratios.

4) Heat pumps designed for low ambient temperature conditions usually have oversized capacities at medium ambient temperatures. For heat pumps with on/off actuators, the system needs to be cycled on and off more often at higher ambient temperatures, due to the relatively lower heating loads. Such cycling increases the component wear, decreases the system efficiency due to the frequent transient operation as opposed to steady-state operation, and also possibly lowers the thermal comfort for occupants.

These operational issues indicate that it is necessary to optimize the operation of cold-climate ASHP in real time to maintain the best possible efficiency. In past decades, many advanced techniques have been proposed to modify the system configuration and operation of ASHP, such as vapor injection (VI) techniques, cascade configurations [11-12]. These proposed advanced heat pumps have been proved that they can be successful used in the cold climate to provide heat demand. For the VI techniques, the heat pump capacity can be enhanced with the increasing refrigerant flow, thus improving the heat transfer through the condenser. For the cascade configuration, smaller compression ratio and then higher compressor volumetric in each stage of compression will lead to a higher operation performance. However, the existing current control methods used by these systems may not realize the potential for these innovations for ASHP. In the open literatures, the state-of-the-art control strategies are essentially based on calibration of system characteristics under the nominal or at most limited scenarios of operating conditions for a specific equipment status, as the highly nonlinear nature of ASHP makes it prohibitively expense to conduct a complete model calibration. The calibrated settings may not be applicable to the realistic working condition for an ASHP, as the actual optimum can be drastically different. Therefore, development of online and cost-effective approaches to real-time optimization of ASHP system efficiency is of keen need for practice.

This dissertation research aims to apply a class of model-free control strategies, known as the Extremum Seeking Control (ESC), to improve and optimize the operating efficiency for the vapor injection, and cascade ASHP systems. In essence, this dissertation research is a proof-of-concept effort, with the proposed control strategies evaluated with Modelica based dynamic simulation models of the associated ASHP configurations, using the Dymola platform and TIL Library [13-15].

### 1.2 Vapor Injection ASHP: Challenge and Opportunity for Efficiency Improvement

Vapor injection is a major class of heat pump configuration for improving efficiency under low ambient temperature operation, which involves injecting the superheated or saturated vapor to the intermediate location for a two-stage ASHP, or the sealed compressor pocket for a vapor compression system. By far, there have been two major configurations of vapor injection: the internal heat exchanger cycle (IHXC) and the flash tank cycle (FTC), as shown in Figure 1.4. From a thermodynamics point of view, the IHXC and the FTC have similar mechanism in efficiency improvement. However, the IHXC system features a lower operation efficiency but easier control strategy; the FTC system features a higher operation efficiency but more challenged control strategy.

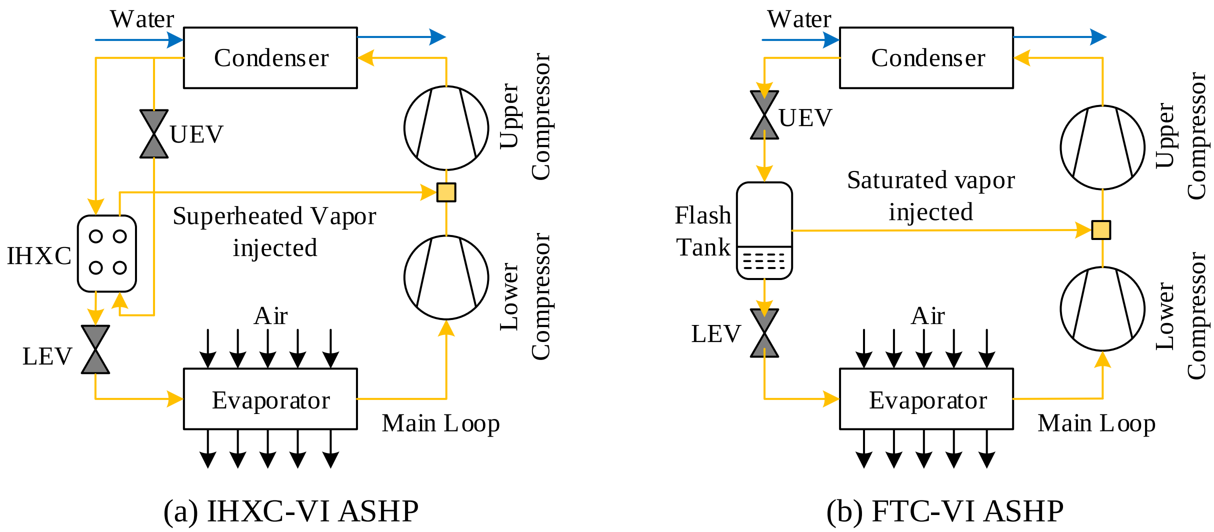


Figure 1.4. Schematic of diagrams for two VI configurations.

It has proven that the vapor injection techniques can improve the performance of vapor compression systems with the reliable cycle operation. Compared to conventional single-stage vapor compression systems, several advantages have been found for the vapor injection based systems [16]:

1) The heating capacity can be greatly improved in cold climate (lower than 0°C). As mentioned earlier, the increase of refrigerant flow through the condenser enhances the heat transfer.
2) The system COP can be improved. For a vapor injection ASHP operated in the cold climate, the heating output and the total power both increase, while the heating capacity increases more than the increase in total power. Therefore, the COP is improved.
3) The compressor discharge temperature can be greatly reduced for a vapor injection cycle comparing to a conventional single-stage cycle. For a conventional single-stage ASHP water heater operated in cold climate, the high compression ratio will cause high discharge temperature of the compressor, which will greatly decrease the system COP. More seriously,

the high temperature can lead to chemical degradation of lubrication fluid and exacerbate component wear and/or failure. The VI techniques can reduce the discharge temperature of compressor since the injected vapor has lower temperature than the vapor inside the compressor, thus making the compression process more like an isentropic one as opposed to the single-stage vapor compression process.

In spite of these advantages, however, the control strategies of current VI-based ASHP systems cannot release the potential for the thermal performance of the VI techniques in practice. As the realistic operation of ASHP systems is subject a large range of ambient and load conditions, the optimal setting of key operational variables can vary significantly. It is critical to maintain the system operation at its optimal efficiency in real time. However, to accomplish this, model-based control/optimization techniques require intensive efforts in model development and calibration due to the nonlinear and time-varying nature of ASHP systems. Such situation has limited the adoption and ramification of the vapor injection based ASHP systems. Therefore, more effective and low-cost control strategies are more desirable for the efficiency operation of the VI ASHP systems.

### 1.2.1 Efficient operation of VI ASHP with IHXC

Figure 1.5 shows the typical schematic diagram of IHXC heat pump system and pressure - enthalpy (p-h) diagram [16]. The VI loop is realized by drawing a small portion of the liquid refrigerant at the condenser outlet and passing it through the upper expansion valve (UEV). Then it enters an internal heat exchanger, turned into the vapor phase while sub-cooling the main-loop refrigerant flow coming from the condenser. The refrigerant vapor of the VI loop enters the intermediate compression chamber of the compressor. The subcooled main-loop refrigerant is expanded by the lower expansion valve (LEV), goes through the evaporator, and then enters the suction port of the compressor. The two channels of refrigerant flow are mixed at the intermediate chamber of the compressor.

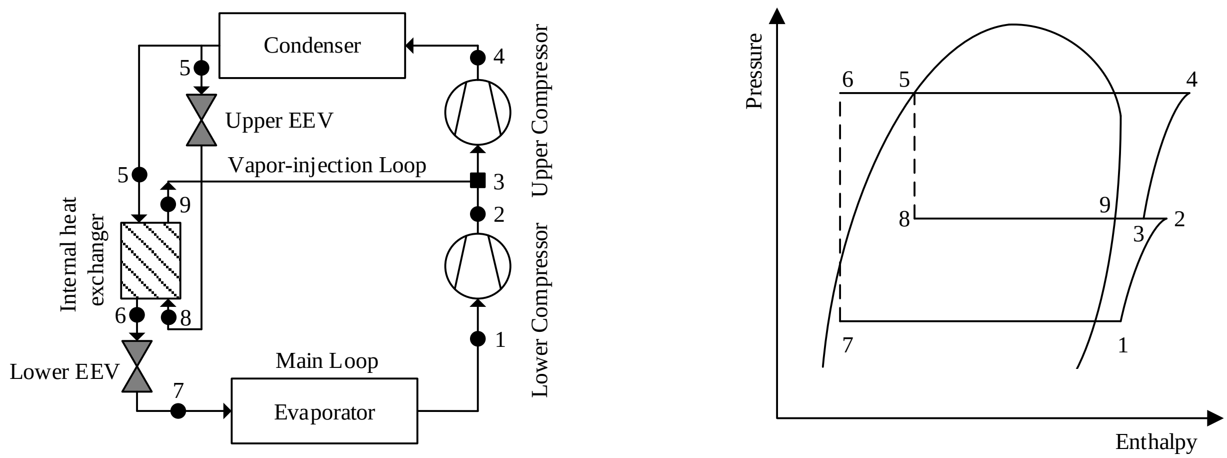


(a) Schematic diagram (b) p-h diagram

Figure 1.5. Schematic diagram and p-h diagram of IHXC VI ASHP.

As shown in Figure 1.5 for the IHXC ASHP water heater, the main loop liquid refrigerant that enters the internal heat exchanger is sub-cooled by the two-phase refrigerant entering the internal heat exchanger from the injection loop [16]. The p-h diagram shows that State 5 is extended to State 6. After the lower expansion valve, the enthalpy difference across the evaporator is greater than the configuration without two-stage expansion. That means the increased enthalpy difference increase the two-phase heat transfer are in the evaporator. However, the vapor injection reduces the refrigerant flow through the evaporator. Therefore, the system heat capacity and performance improvement is determined by a proper injected mass flow rate. For a fixed ambient temperature and load demand, there existing an optimal injected refrigerant mass flow rate, which can make the system operating with the best performance.

For the IHXC ASHP water heater, the current control strategy is to calibrate an optimal superheat under the specific nominal condition, and then this degree of superheat thus calibrated is maintained by a thermostatic expansion valves (TXV) across different operating conditions. The superheat at the internal heat exchanger outlet is manipulated by regulating the upper expansion valve opening so as to control the injected refrigerant mass flow rate. This method has been proven to be reliable and safe in operation [17]. However, the optimal injected refrigerant mass flow rate varies as the ambient temperature and heating load vary. So this method leads to suboptimal efficiency under the conditions other than the nominal. Again, for a practical ASHP system operated in realistic ambient and load conditions throughout its life cycle, frequent calibration is virtually impossible due to the prohibitively high cost.

In the dissertation, the standard ESC is proposed as a model-free real-time optimize control strategy for an ASHP with IHXC vapor injection. The effectiveness is validated by a Modelica model under fixed and realistic ambient condition. The simulation results show that the ESC can indeed optimize the system with the best performance in real-time in cold climates under a realistic ambient temperature.

### 1.2.2 Efficient operation of VI ASHP with FTC

The FTC is another VI configuration. Figure 1.6 shows the specific schematic diagram and p-h diagram. The refrigerant out of the condenser enters the flash tank through the upper expansion valve (UEV). The refrigerant in the flash tank consists of liquid and saturated vapor phases. The liquid refrigerant is drawn from the lower port of the flash tank, enters the evaporator via the lower expansion valve (LEV), and is then circulated to the lower compressor. The saturated-vapor refrigerant in the flash tank is relieved from the upper port of the flash tank, and then mixed with the refrigerant from the lower compressor. Finally, the mixed refrigerant is compressed in the upper compressor and then reject heat through the condenser to complete the cycle [16].

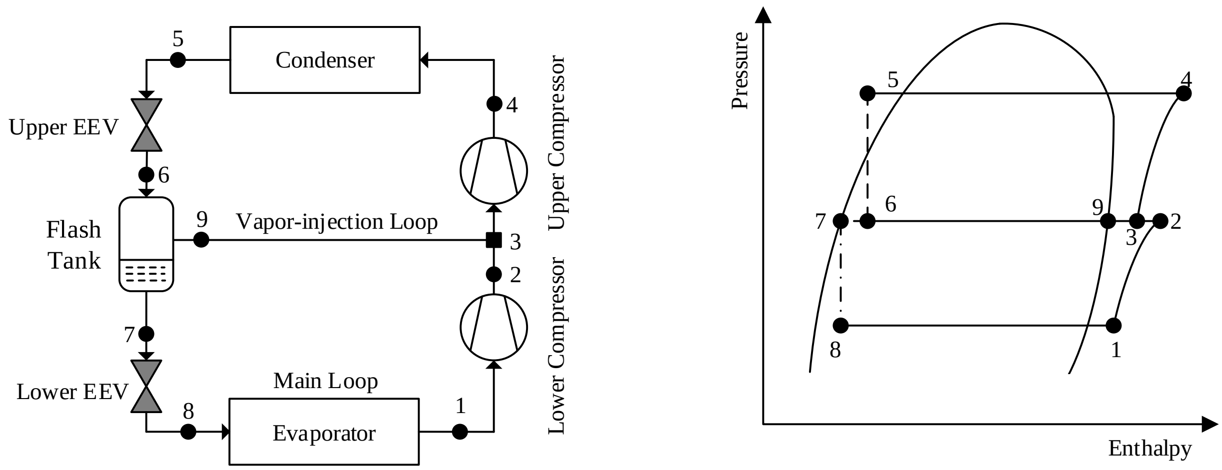


(a) Schematic diagram (b) p-h diagram

Figure 1.6. Schematic diagram and p-h diagram of FTC VI ASHP.

From a thermodynamics point of view, the IHXC and the FTC should have similar performance. The p-h diagrams in Figures 1.5 and 1.6 show that, the two schemes share the same working principle of decreasing the evaporator inlet enthalpy via two-stage expansion. The only discrepancy lies in how the decrease of evaporator inlet enthalpy is achieved: by sub-cooling through the additional heat exchanger, or by two-phase separation in the flash tank [16]. Such difference in configuration results in that the superheat of the injected vapor of the FTC is typically lower than that of the IHXC, which yields more efficient compression process; thus the FTC can achieve higher efficiency than the IHXC.

Compared to the IHXC, an ASHP equipped with flash tank cycle have the following merits.

1) The flash tank cycle has the higher heating capacity and COP. The injected medium for FTC is the saturated vapor, which in principle bears a lower temperature than the superheated vapor being injected for the case of IHXC. This helps reduce the compressor discharge temperature and yield more efficient compression process. Wang [17] has experimentally shown that the

FTC has 2-5% higher heating capacity and COP than those of the IHXC. Ma and Zhao [18] concluded that the heating capacity and COP of the FTC were 10.5% and 4.3% higher than those of the IHXC.

2) The cost of a flash tank is typically less than that of a heat exchanger.

However, the use of flash tank brings forth some difficulty for the controls of FTC. In spite of the appealing performance and cost-effectiveness, the FTC is far behind IHXC in practical adoption, mainly due to the lack of proper control/operational strategy for its vapor injection loop. As mentioned before, the injected refrigerant flow obtained from the flash tank is exclusively saturated vapor, so it is impossible to manipulate/control its superheat by a thermostatic expansion valves as what is typically done for the IHXC configuration. For the IHXC system, even though the superheat manipulation via TXV control is a low-efficiency control method, it remains a safe and reliable control strategy. However, for the FTC system, such a control strategy is infeasible. As indicated in [16], "the major challenge faced by the flash tank cycle is the system control strategy… however, there is no open publication on the detailed control logic for such system…developing a cost-effective system control strategy would be an important topic for the future research." Further, the future work suggested by the authors is that "the current focus of academic researchers and industrial manufacturers is on exploring the challenges facing the flash tank cycle."

In this dissertation, the Newton-based ESC is proposed as a novel control strategy for the flash tank cycle on how to control the upper control value for the vapor injection loop. To the authors' best knowledge, this is the first time to propose a detailed control strategy for such system without elevating the superheat. This control strategy can provide a proper and safe liquid level for the flash tank. Additionally, the optimum system performance can be obtained so that the full potential for the FTC-VI two-stage ASHP system can be realized.

### 1.3 Efficient Operation of a Cascade ASHP

A cascade ASHP (CASHP) water heater system, as shown in Figure 1.7, consists of two independently operated (but thermally coupled) single-stage cycles: the Low Temperature Cycle (LTC) and the High Temperature Cycle (HTC). The LTC absorbs heat from the ambient through the evaporator, and then transfers heat to the HTC through an intermediate heat exchanger known as the Cascade Heat Exchanger (CHE). The refrigerant in the HTC evaporates in the CHE, and is then compressed before entering the condenser where the refrigerant rejects the heat to the water. The CHE works as a condenser for the LTC and evaporator for the HTC. The LTC condensing temperature or the HTC evaporating temperature is known as 'Intermediate Temperature' [19].

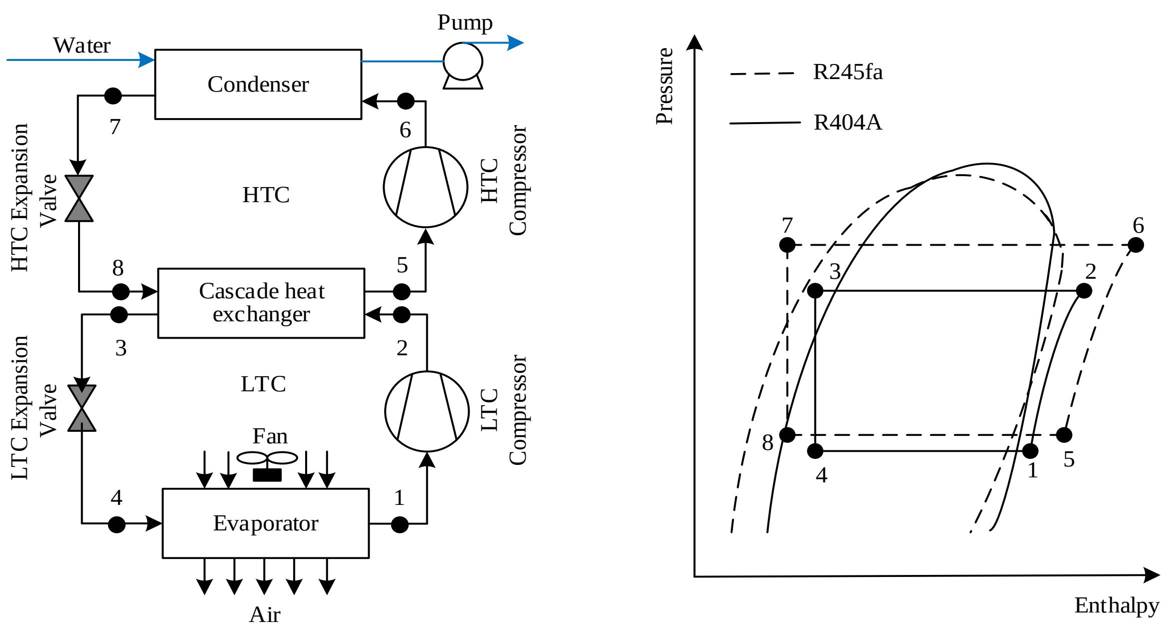


(a) Schematic diagram (b) p-h diagram

Figure 1.7. Schematic diagram and p-h diagram of a cascade heat pump water heater.

Compared to the conventional single-stage system and the aforementioned VI ASHP, the CASHP system has the following characteristics:

1) High system performance. Compared to a single-stage system, the cascade system has a smaller compression ratio and then higher compressor volumetric in each stage of compression. Therefore, it permits an overall higher efficiency higher system performance for the whole system.

2) Higher temperature lift. Compared to the single-stage system or the VI ASHP systems, a CASHP water heater can provide significantly higher water outlet temperature (e.g. above 100°C) even operated in cold climate. Thus, the application of CASHP has been widely expanded to many industrial sectors such as food, beverage and wood products [2].

3) Compared to the VI ASHP systems, the CASHP system offers the flexibility of choosing different working fluid/refrigerant in each cycle. Each fluid/refrigerant can be selected for the optimum performance for the whole system within the specified temperature range.

4) The cascade system involves higher cost and complexity than a single-stage system and the VI systems. In addition, the heat transfer in the CHE between the evaporating process in the HTC and the condensing process in the LTC reduces the efficacy of the cascade system. However, the disadvantage can be partially mitigated by employing a high efficiency plate heat exchanger for CHE.

As the CASHP is beneficial in cold-climate heating with high water temperature demand and high capacity, a great deal of research has been conducted to improve its performance [20-31]. It has become a consensus that the intermediate temperature be the key parameter for the CASHP performance. It is noteworthy that the optimal intermediate temperature change for the different combinations of working fluids, e.g. R134a/R410a or R134a/$CO_2$, among others. In addition, for a CASHP with a specific fluid combination, the optimum intermediate temperature varies with ambient temperature and heating load, similar to what has been described for the VI ASHP system operations. According to the literatures on CASHP research, determination of the optimal intermediate temperature for CASHP systems has been mostly by numerical modeling and/or experimental calibration, which can be performed for only a limited number of operation conditions and specific equipment status. For a practical CASHP system operated in realistic ambient and load conditions throughout its life cycle, the effectiveness of such optimization strategies can be rather limited due to the prohibitively high cost incurred. Therefore, it is desirable to optimize the operation of cascade heat pump systems in real time without the need for modeling and calibration.

In this dissertation, a model-free real-time optimization control strategy is proposed for the CASHP water heater using a multivariable extremum seeking control strategy, with two scenarios handled separately: 1) power minimization for fixed heat capacity operation, in which the optimal intermediate temperature, the HTC and LTC superheat are adopted as the three manipulated inputs, the total power is the only feedback; and 2) COP maximization for variable heat capacity operation, in which the system COP is the only feedback, and the manipulated inputs are the HTC compressor speed, LTC compressor speed and the evaporator fan air mass flow rate.

## 1.4 Research Statement and Dissertation Organization

Based on the introduction of research background in the previous sections, the research problems of interest for this dissertation are summarized as follows:

1) For efficient operation of an air-source heat pump water heater with internal heat exchanger

cycle, develop the dynamic simulation model for such a system, then design and evaluate the ESC based strategy with simulation study.

2) For efficient operation of an air-source heat pump water heater with flash tank cycle, develop a dynamic simulation model for such a system, then design and evaluate an ESC strategy for the system operation.

3) For efficient operation of a cascade air-source heat pump water heater, develop a dynamic simulation model for such a system, then design and simulate the two ESC strategies for power minimization and COP maximization.

The remainder of this dissertation is organized as follows.

Chapter 2 presents the literature review relevant to the aforementioned topics include in this dissertation.

Chapter 3 presents a standard extremum seeking control framework as a model-free optimal control strategy for internal heat exchanger based VI-ASHP, minimizing the total power consumption in real time. The ESC takes the total power as the only feedback, and the intermediate pressure as the manipulated input. A Modelica-based dynamic simulation model of an IHXC-VI ASHP water heater is developed. The water outlet temperature is regulated by the compressor capacity, while the injection-loop expansion valve regulates the intermediate pressure. Under fixed, staircase and realistic ambient temperature profiles, simulation results show that ESC can optimize the intermediate pressure for system efficiency with good steady-state and transient performance.

Chapter 4 presents a novel control strategy for a two-stage air source heat pump water heater with flank-tank-cycle vapor injection. The intermediate pressure setpoint for the injection loop is regulated by the upper electronic expansion valve. Then, a real-time optimization or optimal control framework adjusts the intermediate pressure setpoint to minimize the total power consumption, with the compressor capacity used to satisfy the load demand via an inner-loop controller. In particular, the Newton-based extremum seeking controller is applied as a model-free real-time optimization strategy for such purpose. To evaluate the proposed control strategy, a Modelica based dynamic simulation model is developed for such system. Simulations under fixed, staircase and realistic ambient temperature profiles validate the effectiveness of the proposed control strategy. Besides real-time optimization of system efficiency, a major merit of this strategy is to retain the use of saturated vapor for the injection line, instead of levitating the superheat. The inherent efficiency of the flash tank cycle is thus maintained without additional devices, and the liquid level can be maintained in a proper range.

In Chapter 5, the multivariable extremum seeking control is proposed as a model-free strategy for real-time optimization for a cascade air source heat pump water heater. Two scenarios are considered in this chapter: i) power minimization for fixed heating capacity operation, and ii) COP maximization for variable heat capacity operation. For power minimization, the ESC optimizes the setpoints of intermediate temperature and the superheat setpoints for the high-temperature and low temperature cycles; while for COP maximization, the manipulated inputs are the compressor speeds of the high-temperature and low-temperature cycles and the evaporator fan speed. The proposed strategy is evaluated by simulation studies with the Modelica model, under both fixed and realistic ambient temperature profiles. The simulation results validate its effectives.

Chapter 6 summarizes the contributions of the dissertation research, along with the future work recommended.

# CHAPTER 2

# LITERATURE REVIEW

This chapter reviews the literatures relevant to the dissertation research. The previous research on the IHXC-VI ASHP is first reviewed, followed by that for the FTC-VI ASHP. Then the research on the CASHP is reviewed. As the model-free control scheme adopted in this dissertation research, the extremum seeking control strategy and its applications to the heating, ventilation and air conditioning (HVAC) are reviewed. Finally, the Modelica based dynamic modeling for HVAC systems is reviewed.

## 2.1 Research Review on ASHP with IHXC Vapor Injection

The vapor injection technique, marketed since 1979 for room air conditioners [15, 16], has been received as a mature and effective solution to improving the efficiency and heating capacity of ASHP operation in the cold climates. For the ASHPs with IHXC vapor injection, the working principle and schematic have been introduced in Chapter 1. Most former studies for IHXC-VI ASHP have primarily focused on following respects: (i) system configuration, (ii) component design, and (iii) development of control strategies.

The system level research mostly focuses on performance evaluation for specific system configurations and the impacts of the different refrigerants to IHXC-VI ASHPs [34-37]. Ma et al. [38] tested an ASHP with IHXC vapor injection through an entire winter in Beijing, China. Reliable system operation was demonstrated at the ambient temperature as low as −15°C. The heating capacity and COP were remarkably improved compared to the conventional heat pump system. The discharge temperature was steady and remained below 130°C for low ambient temperatures. Later, Ma et al. [39] tested a prototype ASHP water heater with IHXC which was able to supply high temperature water under low ambient temperature, and the results showed that the intermediate pressure needs to be higher than 1.2 times the square root of the product of the condensing pressure and evaporating pressure for the system operation. In an experiment study on an ASHP with IHXC, Tian et al. [40] showed that the heating COP could exceed 2.0 with the condensing temperature of 50°C and the evaporating temperature as low as −25°C. Wang [17] performed experimental studies using the IHXC-VI technique, achieving maximum improvements in heating capacity and COP of 33% and 23%, respectively, with the ambient temperature of −18°C. Roh et al. [41] evaluated the impact of the intermediate pressure on the heating performance under various injection ratios, with the compressor frequencies varying from 60 to 100 Hz. It was found that the injection ratio was highly affected by the intermediate pressure, which suggested the need for properly designed operating strategy for the VI cycles.

As for the impacts of different refrigerants to IHXC-VI ASHP systems, Cao et al. [42] presented an experimental study of an IHXC-VI ASHP water heater using the R22/R600a mixture. Compared with the operation using R22, the heating capacity and COP of this choice of refrigerant were higher. In addition, the experimental results showed that this mixture refrigerant had a better performance under low ambient temperature with R600a of 15% mass ratio. Joppolo et al. [43] carried out an experimental study for a 20 kW air-to-water heat pump equipped with IHXC vapor injection using R-407C as refrigerant. The results showed that the trend of heating capacity and COP in terms of ambient temperature are almost the same, for both the vapor injection system and a conventional ASHP. However, the vapor injection system performed better when the water outlet temperate increased, and the compressor discharge temperature was greatly reduced due to the vapor injection. Hwang et al. [44] tested the operation efficiency of four different configurations that include a basic single-stage cycle, a vapor injection cycle with IHXC, a basic cycle equipped with an intercooler and a two-stage split cycle with CO2 refrigerant, the results showed that the IHXC performed the best.

The component level research has mostly focused on the development of vapor injection compressors, including screw, rotary, scroll and reciprocating compressor, from the model building to the experiment validation [45-50]. Among the available types of compressor, the scroll compressor is found to be easier for vapor injection development. The scroll compressor has several independent compression chambers, featuring the smallest volume compression gradient. Such merits can handle the slugging problem in vapor injection, and the injection pressure can be controllable with changing the injection port position [51, 52]. Therefore, the scroll compressor appears to have been more adopted [53-58]. Chen et al. [59] developed a detailed model for a scroll compressor, by using the first law of thermodynamics for open control volumes to calculate the instantaneous refrigerant states as a function of the orbiting angle. Individual processes within the compression process have been modeled respectively, including refrigerant leakage and heat transfer with the scroll wrap. This model facilitates the studies on the influences of heat transfer, leakage, and compressor geometry on the compressor performance, thus helping improve the compressor design. Later, Chen et al. [60] continued to develop an overall model for a horizontal scroll compressor using finite volume analysis, where the compression path was divided into nine different elements. By establishing the steady-state energy balance via the lumped capacitance method, the temperature and pressure of the refrigerant in different compressor chambers, the temperature distributions in the scroll wraps, and the temperatures of the other compressor elements can all be obtained, along with the calculation of the power consumption and compressor efficiency. Wang et al. [61] presented an integrated bench design method for refrigerant injection in scroll compressor, which included the location design of injection ports and measuring ports, frequency spectrum analysis of pressure signal, sensor selection and deployment, and design of the pressure-leading system. Wang et al. [62] proposed a general model for a scroll compressor with refrigerant injection, with which the macro performance was predicted along with inner compression process of the injected scroll compressor. The experimental results validated the accuracy of the model. It was found that the refrigerant injection process could be considered as a continual parameter-varying "adiabatic throttling + isobaric mixture" time-varying process. Tello-Oquendo et al. [63] presented a correlation model for a vapor-injection scroll compressor parameterized by the condensing pressure, evaporating pressure and the superheat at the compressor inlet. In particular, the injection mass flow rate was linearly correlated with the intermediate pressure, with the compressor power estimated with a modified polynomial model.

Controls of IHXC-VI ASHP involves the use of novel schemes of sensor, actuator and control logic. Leimbach and Heffner [64] proposed a refrigerant injection valve based on temperature responsive sensor. The opening of injection port can thus be controlled by the measurement of the compressor discharge temperature. Lifson and Taras [65] developed a time dependent vapor injection scheme to reduce losses and thus enhance the performance. By placing a fast-acting control valve on the vapor injection line near the vapor injection port, a good control was realized for the timing during which vapor injection would occur.

A major strategy reported for controlling the IHXC-VI ASHP system is the superheat control by the thermostatic expansion valve (TXV). Wang et al. [66] pointed out that the IHXC had a much wider operating range, and therefore the superheat control by TXV can be a safe and reliable strategy. Tests were conducted on an IHXC-VI ASHP with the R410A refrigerant. Nguyen et al. [67] also conducted a series of experiments in an ASHP with both IHXC and FTC with R407C as refrigerant. It was also found that the IHXC demonstrated a wider injection operating range than the FTC.

## 2.2 Research Review on ASHP with FTC Vapor Injection

With better performance and lower cost than the IHXC, the FTC has drawn significant attention by academia and industry. The past research on FTC can be classified into the three categories similar to IHXC: (i) system performance research, (ii) component level research, and (iii) the control strategy research. For the FTC, the component research mostly focus on the flash tank design. A well-designed flash tank, which can realize the ideal separation of the liquid and vapor, is desirable for system development. In addition, effective control strategies are critical for the FTC.

The system performance research for the FTC systems has mostly focused on the experimental comparison between FTC and IHXC.  Wang et al. [66] gave experimental evaluation for an 11 kW R410A heat pump system with a two-stage VI compressor model with FTC and IHXC. It was found that the IHXC has a wider operating range of the injection pressure than the FTC due to its freedom of manipulating the degree of superheat for the injected refrigerant vapor. However, Compared to a conventional single-stage ASHP, the maximum heating capacity improvement of 34% is achieved by the FTC compared to the 26% of IHXC, and the maximum COP improvement of 23% is achieved by the FTC compared to the 19% of IHXC at the ambient temperature of

17.8°C. Heo *et al*. [68] studied the effects of FTC-VI on the heating performance of a two-stage ASHP with an inverter-driven twin rotary compressor. The experimental results showed that the COP and heating capacity of the injection cycle were enhanced by 10% and 25% respectively compared to the conventional single-stage ASHP (without vapor injection), at the ambient temperature of −15°C. For compressor frequencies ranging from 50 to 100 Hz, the total mass flow rate of the injection loop was 30-38% higher than that of the non-injection cycle. The increase of the total mass flow rate by vapor injection contributed to the enhancement of the heating capacity. Ma et al. [69] experimentally compared an ASHP with FTC and IHXC. The FTC prototype with capacity of 8.15 kW can work for a condensation temperature of 45°C under the evaporation temperature of −25°C. The results also showed that the FTC-VI ASHP system is more efficient than that with IHXC at low ambient temperatures. Heo et al. [70] evaluated the performance of various VI cycles for an ASHP water heater at the ambient temperature of −15°C and concluded that FTC can achieve the highest heating capacity. Ko *et al*. [71] studied an FTC-VI air-to-water heat pump (AWHP) system with an inverter-driven two-stage rotary compressor. By optimizing the volume ratio of the two-stage rotary compressor, the AWHP system showed a 48% increase in heating capacity and a 36% increase in COP over the conventional ASHP, at water temperature of 60°C and ambient temperature of −15°C. Redon *et al*. [72] analyzed the influence of the design parameters and the injection conditions for the two-stage vapor injection heat pump for both FTC and IHXC. The design parameters such as displacement ratio for the two compressors are optimized in terms of COP in ideal conditions. This study also concluded the following: 1) The FTC systems enable operation close to the achievable optimum, resulting in greater capacities and lower discharge temperatures. 2) The FTC systems have the disadvantage of having constrained manipulation due to the use of saturated vapor as the injected medium, while the IHXC is more flexible with the allowable intermediate working conditions. A hybrid heat pump with FTC and subcooler is proposed in [73] to reduce the irreversible thermodynamic loss and improve the system performance, especially at low ambient temperature. Xu et al. [74] performed an experimental comparison for the performance of a VI heat pump system using R410A and R32, which the use of R32 led to 10% and 9% improvements in the capacity and COP, respectively, as compared to R410A. To study the transient behavior of FTC system, Qiao *et al*. [75] investigated dynamic simulation modeling of an FTC-VI heat pump system. A first-principles transient model was developed for the heat transfer and flow processes involved. The lumped-parameter models were developed for the flash tank and expansion devices, with experimental validations in a later study [76]. The injection pressure showed a significant impact on the system performance and the liquid level in the flash tank, but exhibited little effect on the suction pressure.

As for the component perspective, the design of flash tank has attracted the major attention. Although the liquid and vapor separated in the flash tank can theoretically remain single-phase at their respective exits of the flash tank, the liquid-vapor separation cannot be perfect in practice. The design of the flash tank can be traced back to the 1950s [77, 78]. In order to release the potential benefit of the flash tank VI cycle in air conditioning and the heat pump systems, more research and patented work has been reported [79-82]. Pham et al. [83] proposed a flash tank design, in which the refrigerant inlet is located at the middle part of the flash tank. The refrigerant flows along the tangential surface of the wall, which facilitates liquid-vapor separation. Wang et al. [84] proposed a hybrid flash tank that utilizes a floating ball as the device to control the expansion valve opening.

Similarly, the vapor-injection compressor was also another theme for the FTC system research. Wang *et al*. [85] built a thermodynamic model to find the exhaustive relationship between the compressor performance and the injection-loop variables, e.g. the pressure and enthalpy of injected vapor, the area and position of injection port. For an FTC-VI heat pump with a twin rotary compressor, Heo *et al*. [86] built a numerical simulation model which gave the optimum cylinder volume ratios for various design conditions. Park *et al*. [87] developed a thermodynamic model for a variable-speed scroll compressor with refrigerant injection to study the injection conditions and injection geometry as functions of compressor frequency. Li et al. [88] investigated the optimal configurations of heat exchanger and compressor in a two-stage compression ASHP with FTC.

Although the design and analysis for the FTC has been studied extensively, both at the component and system level, its wide adoption in practice has been hampered, mainly due to the lack of effective control strategies. For the IHXC system, the TXV control strategy is a safe and reliable control strategy, in spite of the lower efficiency that can be accomplished. However, for the FTC, the TXV control strategy is no longer feasible: the injected refrigerant flow is exclusively saturated vapor. The FTC control problem has turned into how to control the opening of the upper expansion valve for the vapor injection loop, and some efforts have been reported. Hwang *et al*. [89] presented a control strategy for FTC with experimental study. To maintain the desired liquid level through manipulation of the UEV, certain degree of superheat is managed for the injected vapor by deploying a heat exchanger between the injected vapor and the liquid exiting the condenser. Xu *et al*. [90] proposed to use an electric heater in the vapor injection line in order to reinforce certain degree of superheat as a control signal for the UEV. Both transient and steady-state system behaviors were studied. The proposed cycle control strategy was shown to demonstrate reasonable manipulation of the system operation. However, both methods work by heating the injected vapor from the flash tank to achieve some degree of superheat. Such levitation of the temperature of the injection medium inherently leads to lower thermodynamic efficiency compared to the use of saturated vapor in the standard FTC design, in addition to the efficiency loss due to additional heating. Also, the use of a heating element increases the system complexity and cost.

### 2.3 Research Review on Cascade Air Source Heat Pump

The cascade system configuration was firstly introduced for applications in low-temperature refrigeration systems, as the temperature range of −30°C to −100°C is required in food, chemical and other industries [91]. Under such circumstance, there would be large compression ratio between the condensing side and the evaporating side with a single-stage compression process. The major merit for the cascade systems is the relatively smaller compression ratio for each stage of compression, compared to a conventional single-stage system. Such advantage was later transplanted to the heat pump heating systems for cold-climate operation or offering a higher temperature lift.

Numerous research has been reported on optimizing the performance of CASHP. Bhattacharyya et al. [20] presented an analytical study on the performance of a CASHP refrigeration system with modeling efforts that included both internal and external irreversibility. Wu et al. [21] designed a CASHP water heater combined with phase change material as thermal storage, which was intended for reliable operation against fluctuations in ambient conditions, and especially better performance under low ambient temperature. Roh et al. [22] integrated an IHXC-

VI technique into a CASHP system, for both high- and low-temperature cycles. Test results showed the increase of heating capacity and decrease in the system COP. Kim et al. [23] conducted experimental and numerical studies on an air-to-water CASHP with R134a/R410A, in order to find the optimal charge amount. Similarly, Chae et al. [24] evaluated the impacts of the refrigerant charge amount of the high-temperature cycle on the performance in a steady-state heating operation, for a water-to-water CASHP. Song et al. [25-27] conducted experimental and theoretical comparison for the performance of an R134a/CO2 CASHP system and that of a combined R134a/CO2 system under specific operating conditions. The results showed that the cascade system performed better at lower ambient temperatures, while the combined system performed better under higher ambient temperature. To facilitate the proper choice of these two configurations, an empirical correlation was proposed to identify the region of best performance for each configuration based on an operating condition coefficient. Besides, many complicated systems that include CASHP have been developed and studied [28-31].

The intermediate temperature has been proven a critical parameter which can determine the optimal performance of the CASHP. Park et al. [19] established a thermodynamic model for prediction of the optimal intermediate temperature of a CASHP water heater with R134a/R410A. For R134a, increasing the condensing temperature raises the optimal intermediate temperature but decreases the maximum COP; while for R410A, increasing the evaporating temperature can raise both the optimal intermediate temperature and the maximum COP. A larger temperature difference in a CHE reduces the system COP as well as the optimal intermediate temperature. The experimental study by Kim et al. [92, 93] well validated the effectiveness of this modeling scheme. Lee et al. [94] conducted a thermodynamic analysis for a cascade refrigeration system that uses

CO2 and NH3 as refrigerants for the LTC and HTC, respectively, which was used to determine the optimal condensing temperature of the CHE under various design parameters for maximizing the COP and minimizing the exergy destruction. Wang et al. [95] investigated the effects of the LTC condensing temperature and the CHE temperature difference on the system performance for a cascade refrigeration system with a twin-screw compressor. In addition, Dopazo et al. [96] also studied the optimum CO2 condensing temperature for a CO2-NH3 cascade refrigeration system.

In this dissertation research, the efficiency of CASHP water heater is optimized by using multivariable extremum seeking control strategy as the real-time optimization solution. The intermediate temperature, along with other operational variables, are searched simultaneously to minimize the system power or maximize the system COP.

## 2.4 Review of Extremum Seeking Control and Its HVAC Applications

Extremum seeking control (ESC) is a model-free optimization method, which can search for the unknown and slowly varying input setpoint for optimizing specific performance index with only limited knowledge of the system models. By use of pairs of dither-demodulation signals and proper filtering for extracting the online gradient estimation, the optimum seeking process becomes more robust against external disturbance and time-varying process variation [97]. However, the convergence characteristic of the gradient ESC is heavily affected by the Hessian of the underlying static map for the plant. For systems with nearly quadratic map that has relatively constant Hessian, the convergence rate is nearly consistent regardless the initial condition. The standard ESC works well for such plant. However, for static maps with large variation in Hessian, the convergence rate of ESC can vary significantly with the initial value. In order to address this issue, Ghaffari *et al*. [98] proposed a Newton based ESC strategy. The online estimation of Hessian is realized by using an additional demodulation signal, and the inverse of Hessian is obtained via solving a Riccati differential equation. In this dissertation, both standard and Newton-based ESC are applied in the different model. The review of ESC is divided into two parts:

1) The principle and design guidelines for the dither ESC strategies used in this dissertation research. First, the single-input dither ESC derivation is described in detail, followed by the presentation of the Newton-based ESC. Finally, the multivariable ESC [99, 100] is reviewed.

2) The historical development of ESC is introduced along with its applications.

### 2.4.1 Review of Extremum Seeking Control

ESC deals with the online optimization problem of finding an optimizing input $u_{opt}$ for unknown and/or time-varying cost function $f(u,t)$ [97, 98]. The block diagram of a single-input ESC is shown in Figure 2.1, where $F_I(s)$ and $F_O(s)$ denote the linear time-invariant (LTI) approximation of the input and output dynamics of the system, respectively. A pair of dither-demodulation signals, $M(t)$ and $S(t)$, along with high-pass filter $F_{HP}(s)$ and low-pass filter $F_{LP}(s)$, are used to extract the gradient information. Closing the loop with integral controller can drive the input to optimality provided that the closed-loop system is asymptotically stable.

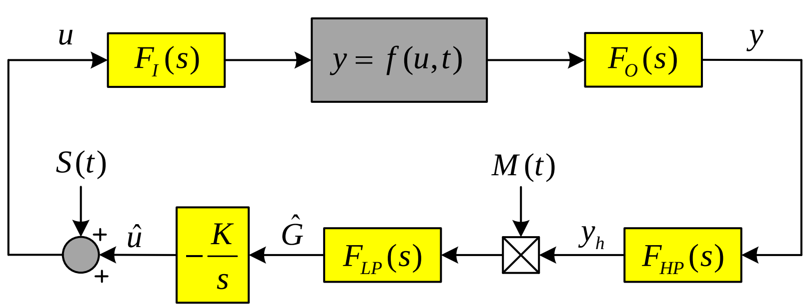


Figure 2.1. Block diagram for standard single-input dither ESC.

The working principle of ESC is illustrated for a single-input scenario. For a nonlinear static plant with single input $u$ and a unique minimum $u^*$:

$$y = f(u) \tag{2-1}$$

The gradient $\hat{G} = \partial f/\partial u$ can be estimated as follows. The input $\hat{u}$ is perturbed by adding a dither signal $S(t) = a\sin(\omega t)$, i.e. the plant input becomes

$$u = \hat{u} + a\sin(\omega t) \tag{2-2}$$

where $a$ is the dither amplitude, $\omega$ is the dither frequency. Then the corresponding plant output can be expressed as:

$$y = f[\hat{u} + a\sin(\omega t + \varphi_{in})] \tag{2-3}$$

where $\varphi_{in} = \angle F_I(j\omega)$ is the phase shift caused by the input dynamics at the dither frequency $\omega$. Eq. (2-3) can be approximated by the leading terms of Taylor expansion around a given value $\hat{u}$:

$$\begin{aligned} y &= f(\hat{u}) + \frac{df(\hat{u})}{d\hat{u}} a\sin(\omega t + \varphi_{in}) + \frac{1}{2}\frac{d^2 f(\hat{u})}{d\hat{u}^2} a^2 \sin^2(\omega t + \varphi_{in}) + \cdots \\ &\approx f(\hat{u}) + \frac{df(\hat{u})}{d\hat{u}} a\sin(\omega t + \varphi_{in}) + \frac{1}{4}\frac{d^2 f(\hat{u})}{d\hat{u}^2} a^2 - \frac{1}{4}\frac{d^2 f(\hat{u})}{d\hat{u}^2} a^2 \cos 2(\omega t + \varphi_{in}) \end{aligned} \tag{2-4}$$

A high pass filter $F_{HP}(s)$ is designed to remove the DC term in equation (2-4). So the filter output is the AC term and it can be keep and approximated as:

$$y_h \approx \frac{df(\hat{u})}{d\hat{u}} a\sin(\omega t + \varphi_{in} + \varphi_{HP}) - \frac{1}{4}\frac{d^2 f(\hat{u})}{d\hat{u}^2} a^2 \cos 2(\omega t + \varphi_{in} + \varphi_{HP}) \tag{2-5}$$

where the $\varphi_{HP}$ is the phase shift caused by the high pass filter $F_{HP}(s)$. Without loss of generality, $F_O(s)$ is simplified as unity, which is true when the sensor dynamics is negligible and/or no postprocessing is needed for the measurement. The high-pass filtered output in Eq. (2-5) is then multiplied by the demodulation signal $M(t)=\frac{2}{a}\sin(\omega t+\theta)$, with θ being the phase difference between the dither and demodulation signals, which yields

$$y_h \cdot M(t) = \left[ \frac{df(\hat{u})}{d\hat{u}} a \sin(\omega t + \varphi_{in} + \varphi_{HP}) - \frac{1}{4}\frac{d^2 f(\hat{u})}{d\hat{u}^2} a^2 \cos 2(\omega t + \varphi_{in} + \varphi_{HP}) \right] \frac{2}{a}\sin(\omega t + \theta)$$

$$= \frac{df(\hat{u})}{d\hat{u}} [\cos(\varphi_{in} + \varphi_{HP} - \theta) - \cos(2\omega t + \varphi_{in} + \varphi_{HP} + \theta)] + h.o.t \tag{2-6}$$

where $h.o.t$ stands for the high order terms. Eq. (2-6) carries the gradient in the DC term, and then the low-pass filter $F_{LP}(s)$ is used to remove the AC terms and retain the DC term. So the output of the low-pass filter includes the estimation of gradient

$$G(u) = \left. \frac{df(u)}{du} \right|_{u=\hat{u}} \tag{2-7}$$

By integrating the gradient proportional signal, the closed–loop system thus realized will make the gradient vanish and thus lead to the optimality, provided that the closed-loop system is asymptotically stable.

The gradient ESC as described above may suffer from inconsistent convergence rate under different Hessian of static map. This is especially undesirable for extremum seeking of asymmetric map. The Newton-based ESC has been developed to provide a gain compensation with online Hessian estimation. As shown in Figure 2.2, the Newton-based ESC contains two loops. The inner loop is a standard dither gradient ESC same as Figure 2.1, while the outer loop contains a demodulation based Hessian estimation with Hessian inverse obtained by use of the Riccati differential equation. The output of the high-pass filter is multiplied the second demodulation signal $N(t)$ and then filtered with the bank of low-pass filters $F_{LPH}(s)$ to extract the Hessian estimation. The output of the Ricatti equation is the real-time inverse of the dynamic estimate of Hessian.

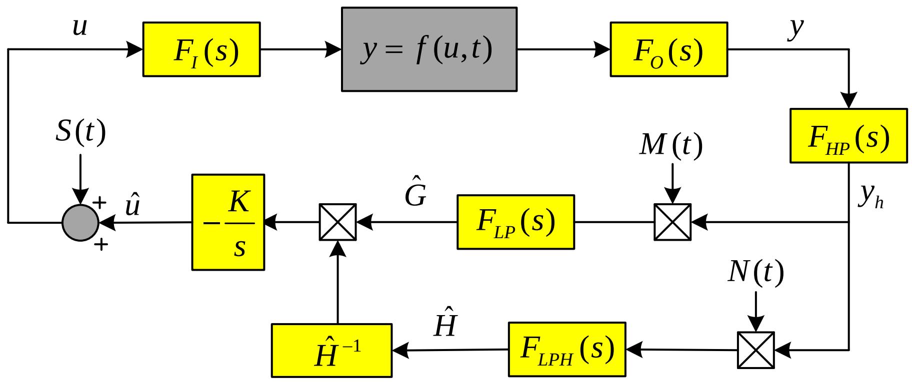


Figure 2.2. Block diagram for the Newton-based ESC [98].

Continued from Eq. (2-5), multiplying $y_h$ by $N(t) = \frac{16}{a^2}\left[\sin^2(\omega t + \varphi) - \frac{1}{2}\right]$ yields:

$$y_h \cdot N(t) = \left[\frac{df(\hat{u})}{d\hat{u}} a\sin(\omega t + \varphi) - \frac{1}{4}\frac{d^2 f(\hat{u})}{d\hat{u}^2} a^2 \cos 2(\omega t + \varphi)\right] \frac{16}{a^2}\left[\sin^2(\omega t + \varphi) - \frac{1}{2}\right]$$

$$= -\frac{4}{a}\frac{df(\hat{u})}{d\hat{u}}\left[\sin 3(\omega t + \varphi) - \sin(\omega t + \varphi)\right] + \frac{d^2 f(\hat{u})}{d\hat{u}^2} + \frac{d^2 f(\hat{u})}{d\hat{u}^2} \cos 4(\omega t + \varphi) \qquad (2\text{-}8)$$

where $\varphi = \varphi_{in} + \varphi_{HP}$. By applying $F_{LPH}(s)$ to retain the DC term, the Hessian estimate can thus be obtained:

$$H(\hat{u}) = \frac{d^2 f(\hat{u})}{d\hat{u}^2} \qquad (2\text{-}9)$$

For the single-input Newton-based ESC, the Hessian is the second-order derivative. So $\hat{H}^{-1}$ is the reciprocal of $\hat{H}$, which can be directly used to multiply the estimation of gradient $\hat{G}$ to remove the impact of the Hessian.

Then the above derivation can be extended to the multi-variable ESC. For an $n$-input nonlinear plant, i.e. $u^*(t) = \arg\min_u f(u,t)$ where $u = [u_1 \quad \cdots \quad u_n]^T$ denotes the vector of manipulated inputs, and $f(u,t): \mathbb{R}^n \times \mathbb{R}^1 \to \mathbb{R}^1$ denotes some measurable cost function (or performance index). $f(u,t)$ is typically assumed convex for the operational range being considered, in which a unique minimum can be achieved. Here the periodic dither signals and periodic demodulation signals are denoted as $S(t) = [S_1(t) \quad \cdots \quad S_n(t)]^T$ and $M(t) = [M_1(t) \quad \cdots \quad M_n(t)]^T$ respectively, where $S_i(t) = a_i \sin(\omega_i t)$ ($i$ = 1, …, $n$) and $M_i(t) = \frac{2}{a_i}\sin(\omega_i t + \theta_i)$. For the multivariable case, the band-pass (BP) filters $F_{BP,i}(s)$ rather than high-pass filters are used to extract the gradient information for the $i$-th channel in a more isolated fashion.

The multi-variable ESC process can be similarly interpreted for the $n$-input plant ($n \geq 2$), following Figure 2.1. The plant output can be expressed as:

$$y = f[\hat{u} + S(t)] = f(\hat{u}) + g(\hat{u})S(t) + \frac{1}{2}S(t)^T HS(t) + R(S(t))$$

$$= \sum_{i=1}^{n} f(u_i) + \sum_{i=1}^{n} g_i \cos(\omega_i t) + \frac{1}{2}\sum_{i=1}^{n} h_{ii} \cos(\omega_i t)\cos(\omega_i t) + \sum_{1\leq i\leq j\leq n} h_{ij} \cos(\omega_i t)\cos(\omega_i t) \qquad (2\text{-}10)$$

where $R(S(t))$ is the high-order terms of the Taylor expansion which can be ignored. In addition, the cosine function is used to express both sine and cosine terms in the results for simplifying the analysis. The phase in each trigonometric function would have no effect on analysis for relationship between dither frequencies, so the phase shift is also omitted in the analysis.

For this plant, assuming that the Hessian is symmetric matrix, i.e. $h_{ij} = h_{ji}$. So in Eq. (2-10), the DC parts are:

$$\sum_{i=1}^{n} f(u_i) + \frac{1}{4}\sum_{i=1}^{n} h_{ii} \tag{2-11}$$

The AC parts in Eq. (2-10) should be:

$$\sum_{i=1}^{n} g_i \cos(\omega_i t)\,,\ \sum_{i=1}^{n} h_{ii}\cos(2\omega_i t)\,,\ \sum_{i=1}^{n} h_{ii}\cos(2\omega_i t)\ \sum_{1\le i\le j\le n}^{n} h_{ij}[\cos(\omega_i+\omega_j)t+\cos(\omega_j-\omega_i)t] \tag{2-12}$$

Then the above output passes through the band-pass filters, the DC terms are removed and the AC terms are retained. Then the outputs of the band-pass filters are multiplied by the demodulation signal $M(t)=\begin{bmatrix} M_1(t) & \cdots & M_n(t)\end{bmatrix}^T$ to demodulate. After the demodulation, the AC parts for a multi-variable case are the following:

$$g_r\cos(2\omega_r t) \tag{2-13}$$

$$\sum_{i=1}^{n} g_i\cos(\omega_i t)\cos(\omega_r t) = \sum_{i=1}^{n} g_i[\cos(\omega_i+\omega_r)t+\cos(\omega_i-\omega_r)t],\quad for\,\forall i\ne r \tag{2-14}$$

$$\sum_{i=1}^{n} h_{ii}\cos(2\omega_i t)\cos(\omega_r t) = \sum_{i=1}^{n} h_{ii}[\cos(2\omega_i+\omega_r)t+\cos(2\omega_i-\omega_r)t] \tag{2-15}$$

$$\sum_{1\le i\le j\le n}^{n} h_{ij}[\cos(\omega_i+\omega_j)t+\cos(\omega_j-\omega_i)t]\cos(\omega_r t)$$

$$=\sum_{1\le i\le j\le n}^{n} h_{ij}[\cos(\omega_i+\omega_j+\omega_r)t+\cos(\omega_i+\omega_j-\omega_r)t+\cos(\omega_j-\omega_i+\omega_r)t+\cos(\omega_j-\omega_i-\omega_r)t] \tag{2-16}$$

The DC term that contains $g_r$ is the estimated gradient that is wanted. Then both the DC and AC terms pass through a low-pass filter, thus the AC terms get removed. Finally, the estimated gradient $\hat{G}$ is obtained. To make sure that Equations (2-14) through (2-16) have no DC terms and to reduce inter-channel interference in gradient information, the dither frequencies need to satisfy the following conditions:

1) For Eq. (2-14), $\omega_r \neq \omega_i \quad for \forall i \neq r$. The same dither frequencies cannot be chosen for avoiding the estimation of $g_r$ corrupted by $g_i$.

2) For Eq. (2-15), $\omega_r \neq 2\omega_i$. The chosen dither frequency cannot be twice of another one for avoiding the estimation of $g_r$ corrupted by $h_{ii}$.

3) For Eq. (2-16), $\omega_r \neq \omega_i + \omega_j$ for $\forall$i, j$\neq$r. A dither frequency cannot be the sum of any other two frequencies for avoiding the estimation of $g_r$ corrupted by $h_{ij}$.

The reason for choosing band-pass filters over conventional high-pass filters in ESC design in this study is to achieve better cross-channel decoupling for the gradient estimation. For each input channel, an anti-notch BP filter is designed with the center frequency chosen at the dither frequency, thus the phase response of the filter vanishes at the dither frequency.

For the multi-variable Newton-based ESC, $\hat{H}^{-1}$ in Figure 2.2 is the inverse of the Hessian matrix. Directly finding the inverse matrix can be computationally expensive. Also, the estimated Hessian matrix may be singular under some condition. To address such issues, a Riccati differential equation $\dot{\Gamma} = \omega_r \Gamma - \omega_r \Gamma H \Gamma$ is used to derive $\hat{H}^{-1}$ as shown in Figure 2.3. The equation has two equilibria: $\dot{\Gamma}_1 = 0$ is unstable and $\dot{\Gamma}_2 = H^{-1}$ is locally exponentially stable. The solution of Riccati equation asymptotically converges to the actual inverse of Hessian estimate.

The above is the detailed description for the derivation of the ESC. For the specific ESC design process, the following guidelines need to be followed [99, 101].

(1) Open-loop testing is performed to estimate the input dynamic for each input channel. Step test is typically the choice for the case of low-order input dynamics.

(2) The dither frequency is typically chosen within the bandwidth of the input dynamics.

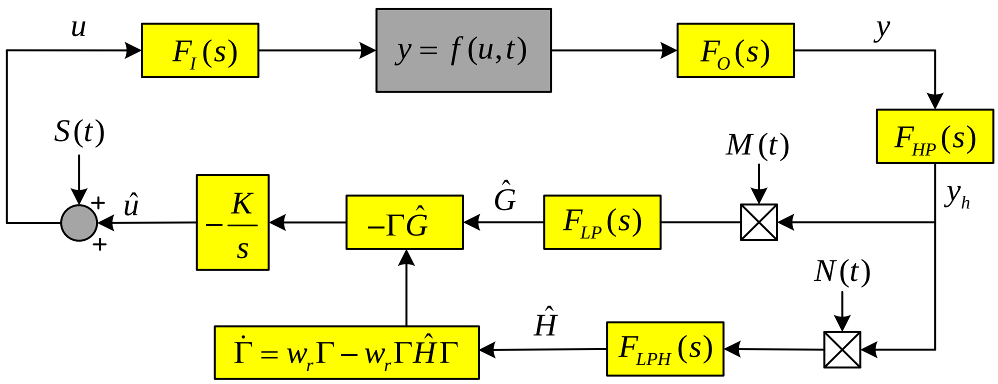


Figure 2.3. Block diagram for Newton based ESC [98].

(3) The dither amplitude $a_i$ should be as small as possible in order to reduce the amplitude of steady-state oscillation (i.e. steady-state error of search), but meanwhile large enough to guarantee sufficient signal-to-noise ratio (SNR) for the dithered output at the respective dither frequency.

(4) The band-pass or high-pass filters should be designed to retain the dither harmonics, while the low-pass filter is designed to provide sufficient roll-off at twice the dither frequencies.

(5) The phase difference between the dither and demodulation signal pairs should be appropriate such that the positive realness of the averaged system is secured.

(6) The integral gain needs to be adjusted to guarantee the stability for a possible range of input dynamics bandwidth to achieve a proper convergence rate based on the estimated Hessian of the static map, dither amplitude and dither frequency. If possible a properly selected larger gain can improve the transient performance.

### 2.4.2 Historical development of ESC and its applications

Leblanc [102] first presented the idea of ESC in 1922. In the mid of 20$^{th}$ centenary, ESC became popular and had been applied in various applications including internal combustion engines and gas furnaces, among others [103-105]. However, lack of a rigorous proof of stability had been a significant issue for the development of ESC. Aström and Wittenmark [106] pointed out that ESC is one of the most promising adaptive control methods but needs for clear design guidelines and stability proof. Krstic and Wang [97] first gave a rigorous local stability analysis and proof of a dither ESC for a general SISO nonlinear system by employing the Averaging Analysis and the Singular Perturbation Method in 2000. Later Krstic and his co-workers [107], Rotea [108], as well as Walsh [109], among others, extended such analysis to the dither ESC with multiple inputs. These work made major contribution to the revival and growth of ESC.

Afterwards, a lot of research has been conducted to enrich the ESC design and analysis, in order to make it fit better for control practices. A major drawback of conventional ESC is the time-separation issue, i.e. the effective gradient search process is carried out at a time scale much slower than the plant dynamics. Such slow convergence is indeed undesirable for most engineering applications. Several adaptive forms of ESC algorithms have been proposed to speed up the convergence for generic nonlinear dynamic plant. Scheinker and Krstić [110] presented a form of ESC that guaranteed known bounds on update rates and control efforts. The method is validated with 2D vehicle velocity control model in which the velocity is constrained. Guay and Dochain [111] formulated the ESC problem as a time-varying gradient estimation problem. They claimed that, by avoiding the need for averaging, the impact of dither signals on the ESC performance could be minimized. Gelbert et al. [112] replaced the conventional high-pass and low-pass filters in the ESC loop with the extended Kalman filters, and the simulation results showed 50% reduction of the convergence time compared to the classical ESC. Moase and Manzie [113] presented a semi-global stability analysis of ESC for Hammerstein plants, in which an observer is used to estimate the unknown gradient instead of using low-pass filter for conventional ESC scheme. Compared to conventional ESC, faster dither frequency is allowed to speed up the convergence for Hammerstein plants while the stability is still observed. Durr et al. [114] proposed the Lie bracket based approximation for ESC along with the saddle-point dynamics based stability analysis. Guay et al. [115] proposed the proportional-integral ESC scheme which incorporates adaptive parameter estimation.

For practical systems, the operation is subject to input and state constraints. Due to the inherent inclusion of integrator in the ESC loop, input saturation could disable the ESC searching process especially when the optimum input varies between an interior point to a boundary point of the operation range. There have been remarkable attempts to enable ESC to handle input saturation. Li and Seem [116] proposed a back-calculation based anti-windup ESC, in order to handle the undesirable actuator saturation. Li et al. [117] demonstrate the effectiveness of this scheme in avoiding integrator windup for an ESC application of air handling unit operation. Later, Tan et al. [118] proposed two other anti-windup ESC schemes, along with a systematic framework for the analysis of anti-windup ESC. One is based on a constrained optimization approach in which some penalty function is used to adapt the search so as not to violate the constraints. The other technique uses an anti-windup scheme, a widely used mechanism in engineering to prevent windup of integral action in a controller. It is demonstrated that both methods are essentially equivalent. In that for any penalty-function based ESC, there exists an equivalent anti-windup ESC whose phase portrait is a global approximate of the penalty-function ESC. In addition, the research on decentralized, distributed and multi-agent ESC schemes have been investigated for large-scale networked systems [119-121]. A lot of research has been reported to enhance the local ESC to achieve global optimization [122-124].

Based on the efforts in the theoretical aspects, ESC has observed its rapid applications to different areas, such as MPPT (maximum power point tracking) control of photovoltaic (PV) systems [125], wastewater treatment [126], fuel cells [127], robot navigation [128], vehicle anti-lockup braking system (ABS) system [129], laser control [130], bioreactor [131], wind turbine [132, 133], among others. For the HVAC area, ESC has emerged as an appealing solution to model-free real-time setpoint optimization strategy for achieving energy efficient operation, due to the nonlinear, distributed and time-varying nature of such system and the cost-driven constraint of this industrial sector. Li et al. [134] proposed using an ESC algorithm to optimize the performance of a prototype standing wave thermoacoustic cooler by both tuning the boundary condition and the driving frequency. The experimental results demonstrated the effectiveness of the using ESC for maintaining maximum achievable performance. Sane et al. [135] presented the dither-based ESC as an online optimization algorithm for chilled water plant control to minimize the total power consumption. Seem et al. [136] used the ESC to vary the flow of outdoor air into the building to minimize the mechanical cooling load in a building. Li et al. [137] proposed to minimize the energy consumption by seeking the optimal outdoor air damper opening for an airside economizer. Mu et al. [138] experimentally validate the effectiveness of ESC for airside economizer. Gall et al. [139] developed a dynamic model of a single-zone variable air volume system and the space condition control loops. The ESC is used to minimize the total system power and results showed a 10.8% power saving.

For chilled-water systems, Li et al. [140] applied the ESC to minimize the total power consumption via using the fan speed as control input. Several different ESC strategies are compared by Mu et al. [141] on a chiller plant model. In addition, Mu et al. [142-144] maximized the energy efficiency of chiller water plant with parallel chillers by virtue of ESC. The feedback to ESC is the total power consumption of the plant consisting of chiller compressors, cooling tower fan, and condenser water pumps, in combination with penalty terms for input-saturation. The control inputs include the cooling tower fan airflow, condenser water flows and evaporator leaving chilled-water temperature setpoint.

ESC also have been widely applied in the heat pump systems. Burns and Laughman [145] applied the ESC method for a vapor compression system, in which ESC can automatically discover sets of inputs that minimize the energy consumption while the machine is in operation. Xiao et al. [100] proposed a multi-variable ESC for a variable-speed mini air-condition system. The total power is minimized by optimize the evaporator and condenser fan speed and the experiment validated the effectiveness of the proposed method. Weiss et al. [146] considered minimizing the total power consumption for a vapor compressor system by integrating the ESC and model predictive control. Dong et al. [147] proposed using the ESC to minimize an ASHP for both heating and cooling operation and validating it by simulation model. Koeln et al. [148] showed there exists an optimal subcooling, which maximize the vapor compression system efficiency by simulation and experiment results, and the ESC is implemented to find the optimal subcooling in an adaptive and model-free manner. Hu et al. [149, 150] applied ESC strategy to optimize the discharge pressure for an air-source transcritical CO2 heat pump water heater for minimizing the total power consumption and maximizing the system COP. Guay and Burns [151] compared the traditional perturbation-based ESC and a time-varying ESC in the context of optimizing the energy efficiency of a vapor compression system. It was found that the time-varying ESC converged faster and more consistently than the other method tested.

## 2.5 Review of Modelica Based Modeling for HVAC

Modelica is a non-proprietary, domain-neutral modeling language that supports several different modeling formalisms. It can be used to solve a variety of problems that can be expressed in terms of differential-algebraic equations describing the behavior of continuous variables and discrete variables [152]. Compared to the conventional modeling schemes based on imperative languages, the modeling based on Modelica bears the following four features [153]:

1) Modelica is an object-oriented equation-based modeling language, as opposed to the imperative languages featuring assignment statements. Such paradigm enables the so-called acausal modeling of differential algebraic equation systems.
2) With Modelica designed as an object oriented programming language, the components, processes and subsystems are developed as 'classes' without the need for defining a specific direction of data flow. The reuse and evolution/expansion of components are much easier than modeling with imperative languages.
3) Modelica features the capability of so-called multi-domain modeling, i.e. the model components describing physical objects of different domains, such as electrical, mechanical, thermodynamic, fluidic and control systems, can be connected to form a larger scale system.
4) Modelica based integrated development environment, e.g. Dymola, features decoupling of equation based physical modeling and the development and evolution of numerical solvers. Such feature brings forth the following benefits: i) the modelers are not required to be involved

in implementation of numerical algorithms (as opposed to the scenario of modeling with imperative language like Fortran), and ii) it is much more convenient to expand the software infrastructure, e.g. the ramification of component/media libraries on a unified platform.

These advantages make Modelica both powerful and broadly applicable for modeling and simulation of mechanical, electrical, thermodynamic, hydraulic systems and controls. As pointed out by Li et al. in their reviews [154, 155], dynamical modeling of HVAC system is usually complicated by strong interactions among multiple physical domains as shown in Figure 2.4, including thermodynamics, heat transfer, fluid mechanics, rigid body dynamics, electromagnetics and control systems.

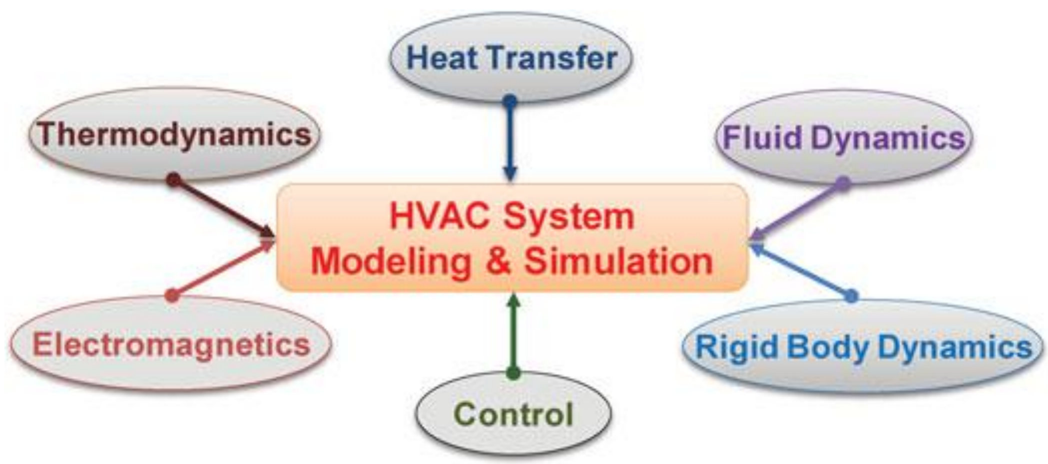


Figure 2.4. Schematic of multi-domain HVAC system modeling and simulation [154].

These features make the Modelica suitable for the HVAC system modeling. In addition, they pointed out that the Modelica-based modeling platform offers some desirable features for HVAC control simulations, such as object-oriented and acausal modeling, resulting in the ease of modeling and the reduction in development cost.

Li et al. [156] developed a Modelica-based dynamic model for a chilled-water cooling coil in order to make the cooling coil modeling more accurate and computationally efficient. The transient behaviors and steady-state predictions for the dynamic coil model is benchmarked with experimental data and the results show well agreement. Later, Li et al. [157, 158] developed a dynamic water-cooled centrifugal chiller model with Dymola and TIL in Modelica language. In this model, detailed losses at the impeller and the diffuser were considered based on compressor geometry parameters. For the special case of centrifugal chiller initialization, a three-step preprocessing scheme was proposed to obtain suitable initial guess that enabled the nonlinear solvers to start at physically reasonable values. Simulation results demonstrated the effectiveness of the proposed modeling framework and initialization method. Mortada et al. [159] developed a dynamic modeling of an integrated air-to-air heat pump using Modelica. The Modelica language allows the model to be flexible to handle different heat-exchanger configurations. Qiao et al. [160] compared the accuracy and computational intensity of dynamic model for a simple vapor compression cycle with Modelica, Simulink and SimScape™. Gall et al. [161] presented a dynamic model of a short cycling scroll compressor that includes scroll geometry, leakage and a mathematical approximation of the digital capacity mechanism has been developed with the Modelica. It is verified by the experimental data, the results showed good agreement for the model and experiment. Tian et al. [162] developed a Modelica based integrated platform that coupled the HVAC equipment, multizone building model and computational fluid dynamics (CFD) simulations for airflows. Zhou et al. [163] developed a Modelica based model of an air-to-air plate-fin heat exchangers (PFHEs), without considering the latent heat. The proposed modeling scheme features: i) the impacts of the changing air flow rates and temperatures, ii) the use of nominal parameters as inputs, without the use of any geometric data, and iii) no spatial discretization needed for the numerical solution. With significantly reduced computational intensity than the finite-element method, the proposed model showed less than 10% modeling error against the experimental data. Elisa et al. [164] investigated different existing Modelica models for pipe and boiler, and selected useful models that could be extended with equations for simulation of Legionella pneumophila bacterial growth. They pointed out that in future research, HVAC designers will be able to investigate the contamination risk for Legionella pneumophila in the design phase of a hot water system, by implementing the customized pipe and boiler model in a hot water system model. Besides the above, other efforts of Modelica based HVAC modeling included $CO_2$ refrigeration [165], vapor compression cycle [166], heat exchanger and cooling tower [167, 168], building energy and control [169-171], among others.

Motivated by the great need for various HVAC applications, many Modelica libraries for simulation of thermo-fluid and HVAC systems have been developed, such as ThermoFlow Library [172, 173], Air-conditioning Library [174], Modelica Fluid Library [175], HIT Library [176], Fluid Flow Library [177], and TIL Library [14], Modelica Building Library [178]. Among these, the TIL Library is designed for steady-state and dynamic simulation of thermo-fluid systems, jointly developed by TLK-Thermo GmbH and Technical University at Braunschweig. TIL can be easily adapted to model and simulate customized refrigeration systems, air conditioning systems, heat pump systems, supermarket and transportation refrigeration systems, among others [14]. On one hand, detailed models can be developed for individual components. On the other hand, the models, assisted by various optimization algorithms built in Modelica, are highly applicable for the design and optimization of large-scale complex systems. Furthermore, various add-on libraries are available for simulation of components and systems of different domain applications. The

Modelica Building Library [178], developed by the Lawrence Berkeley National Laboratory, is a free open-source library with dynamic simulation models for building zone and airflow, district energy and control systems, in order to facilitate simulation of building energy control systems.

This dissertation research, in addition to Dymola platform, has utilized the TIL Library [14], Modelica Building Library [178], Modelica Standard Library [179] and Multi-criteria Optimization Library [180] to for the modeling and optimization work. The TIL Library is used to develop the ASHP models, the Modelica Building Library is used to model the ambient conditions, the Modelica Standard Library is used to build the control systems, and the Multi-criteria Optimization Library is used to calibrate the global optimum as benchmark to evaluate the steady-state performance of ESC strategies. In particular, for the ASHP with FTC vapor injection optimization in Chapter 4, a flash tank model is developed by enhancing the Separator model in TIL (*TIL.VLEFluidComponents.Separators.Separator*) with the modeling framework provided by Qiao et al. [75].

# CHAPTER 3

# EFFICIENT OPERATION OF AN AIR-SOURCE HEAT PUMP WITH INTERNAL HEAT EXCHANGER CYCLE VAPOR INJECTION*

This chapter presents the ESC based real-time efficiency optimization strategy for an ASHP water heater with an IHXC vapor injection, from design, simulation to results analysis.

## 3.1 Introduction and Research Motivation

As introduced in Chapter 1, the current control strategy for the ASHP with IHXC is to fix a setting constant superheat for the injection loop under the nominal operation condition by employing thermostatic expansion valves (TXV). A sensing bulb and a pressure line are attached at the internal heat exchanger outlet to regulate the UEV opening to satisfy the superheat setpoint via manipulation of the injected mass flow rate. However, field operation of an ASHP is subject to significant variation in ambient condition and heating load demand, as well as the degradation of the equipment characteristics throughout its operational life. Therefore, such control method based on the calibrated superheat setpoint limited the potential of realizing the achievable efficiency for ASHP operation, the operational efficiency can often be significantly away from the actual optimum under different combinations of ambient, load and equipment conditions other than the nominal.

In this chapter, the ESC is proposed as a novel control strategy to optimize in real time the operational efficiency of an ASHP water heater with IHXC. Figure 3.1 shows the schematic diagram of ESC based IHXC-VI ASHP. For the injection loop, the UEV employs an electrical expansion valve (EEV) in place of the conventional TXV. The UEV is controlled by an inner-loop PI controller to regulate the intermediate pressure and consequently the injected refrigerant mass flow rate. The ESC takes the total power measurement as the sole feedback and the manipulated input is the intermediate pressure of the VI loop. The mass flow rate and the inlet temperature for the water passing through the condenser are set to be constant, while the outlet temperature is regulated by another PI controller via the compressor frequency. Thus, the heating capacity is maintained as constant. The main-loop superheat is set as constant and regulated via the LEV opening. The evaporator fan speed is set as constant. The proposed ESC stategy was validated with simulation study using a Modelica-based dynamic simulation model with several simulation scenarios.

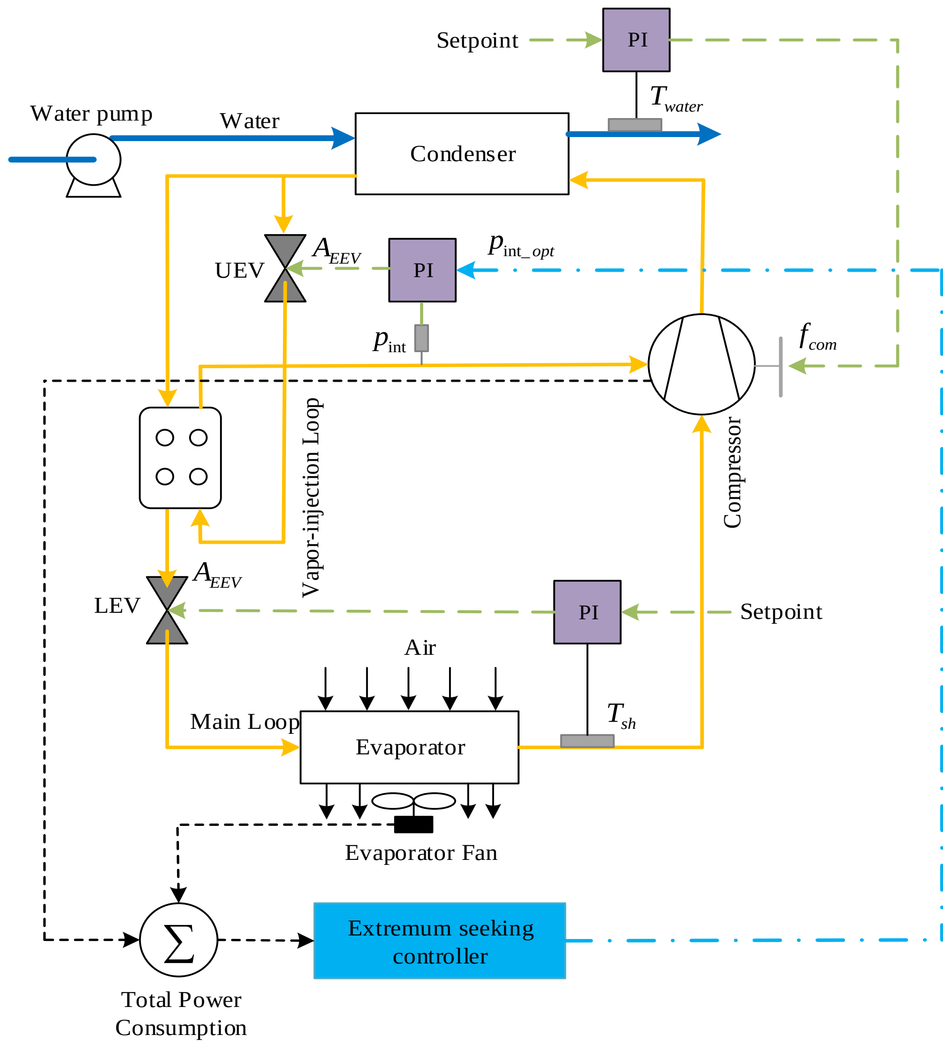


Figure 3.1. Schematic diagram for the ESC based operation for IHXC-VI ASHP.

## 3.2 Dynamic Simulation Modeling of an IHXC-VI based Heat Pump Water Heater

### 3.2.1 Dynamic modeling

In order to evaluate the proposed ESC control strategy in the IHXC-VI heat pump water heater system, a Modelica-based dynamic simulation model is developed using Dymola 2017 [13] and TIL Library 3.4.2 from TLK-Thermo [14, 15] as shown in Figure 3.2.

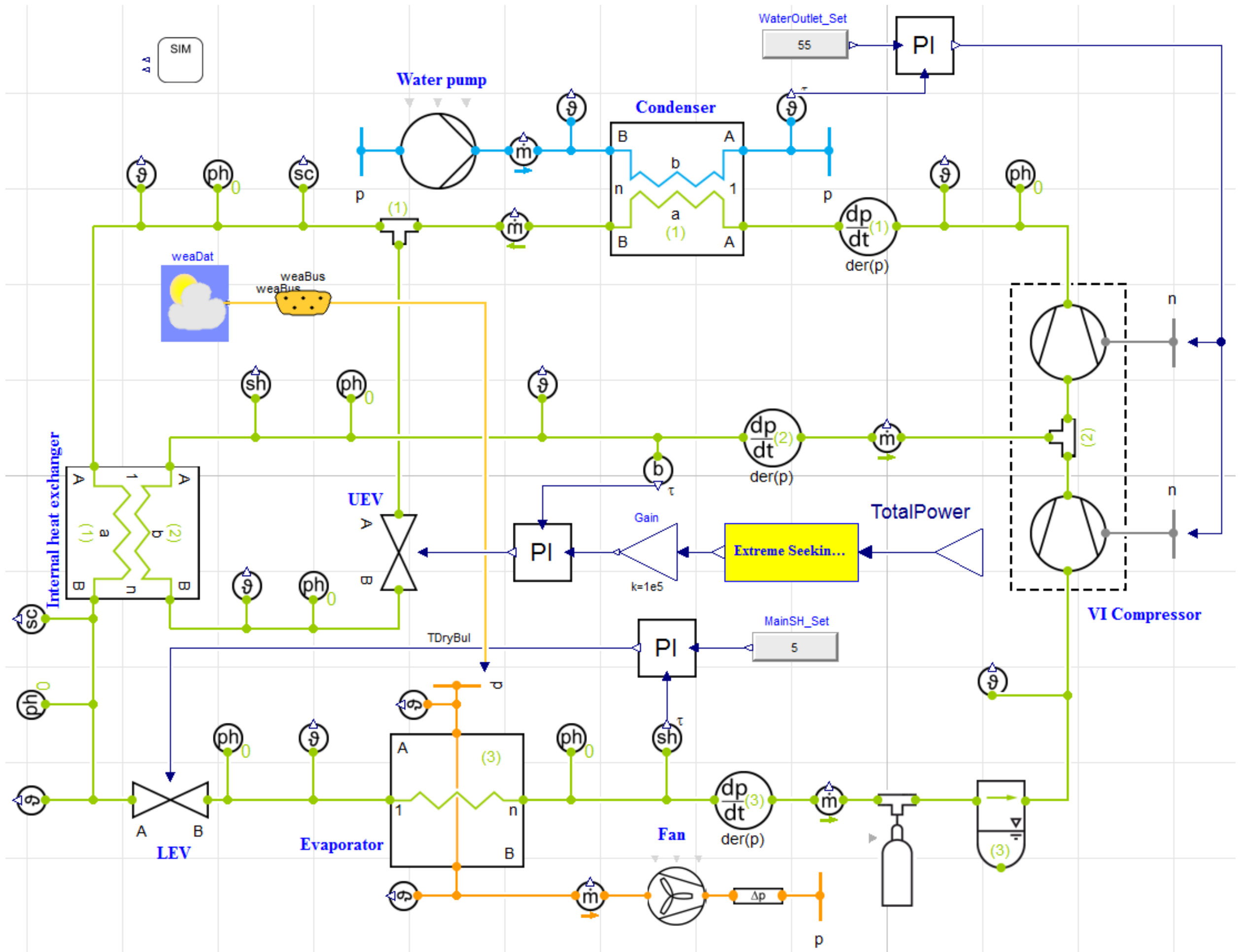


Figure 3.2. Dymola layout for the IHXC-VI ASHP water heater model with ESC.

The VI compressor is modeled by a cascade of two scroll compressor modules (*TIL.VLEFluidComponents.Compressors.ScrollCompressor*) and one junction module (*TIL. VLEFluidComponents.JunctionElements.VolumeJunction*). The junction module works as a mixing chamber. The frequencies of the two compressors are adjusted simultaneously so as to emulate the fact the VI compressor has a single shaft. A tube-and-tube heat exchanger is adopted as the condenser that rejects the heat to the water. For the water side of the condenser, the mass flow rate and the inlet temperature are set to be constant, while the outlet temperature is regulated by a proportional-integral (PI) controller via the compressor frequency. A fin-and-tube cross-flow heat exchanger module (*TIL.HeatExchangers.FinAndTube.MoistAirVLEFluid.CrossFlowHX*) is used to model the evaporator which absorbs the heat from the ambient air; the model can handle the latent heat transfer with the moist air when applicable. A plate parallel-flow heat exchanger module (*TIL.HeatExchangers.Plate.VLEFluidVLEFluid.ParallelFlowHX*) is used to model the counter-flow IHXC, which realizes the heat transfer between the main and injection loops. The expansion valve is modeled with the orifice valve module (*TIL.VLEFluidComponents.Valves.OrificeValve*), which calculates the mass flow rate with dependency on the pressure drop using the Bernoulli Equation, with the effective flow area as an input variable. The evaporator fan is modeled with a simple fan module (*TIL.GasComponents.Fans.SimpleFan*), whose operation can be defined with pressure increase or mass flow rate. The water pump is modeled with an affinity-law based pump module (*TIL.LiquidComponents.Pumps.SimplePump*). In this study, the mass flow rate for the airside of the evaporator and the waterside of the condenser are set as constant.

Table 3.1. Design specifications of major components of IHXC-VI heat pump.

| Components | Design specifications |
|---|---|
| VI Compressor | Scroll compressor; displacement: $72\times10^{-6}$ m$^3$ for lower and $30\times10^{-6}$ m$^3$ for upper; variable speed. |
| Condenser | Tube-and-tube heat exchanger; counter flow; copper; refrigerant tube: *Φ*7.92 mm, number of parallel tubes 7; water tube: stainless steel, DN50, number of parallel tubes: 1; tube length: 4.5m. |
| Evaporator | Fin-and-tube heat exchanger; staggered copper tubes; tube diameter 7mm; wall thickness: 1.5mm; number of serial tubes 3; number of parallel tubes |

| | |
|---|---|
| | 16; fin spacing 2.2mm; thickness 0.2mm; number of parallel tube side flows 6; tube length 0.8 m. |
| IHXC | Plate heat exchanger; steel; number of plates 5; plate length 0.2m; plate width 0.1m; pattern angle 35°. |
| Evaporator fan | Fan efficiency: 0.4; nominal air mass flow rate: 1.1 $kg \cdot s^{-1}$ |
| Expansion valve | Electronic expansion valve; typical effective flow area: $0.2 \times 10^{-6}$ $m^2$. |

In this study, the UEV in the injection loop is controlled by an inner-loop PI controller to regulate the intermediate pressure and consequently the injected refrigerant mass flow rate. The LEV in the main loop is used to regulate the corresponding superheat setpoint, which can be adjusted by another PI controller. The modeling details for the scroll compressors and other components are given in the Appendix A. Table 3.1 shows the design specifications for the major components.

### 3.2.2 Performance evaluation for the system operation

The VI compressor model consists of two scroll compressors of different displacement ranges. Their frequencies can be set simultaneously by one PI controller. The power consumption of compressor is variable under change of operational conditions. In this study, the evaporator fan speed is fixed, so the fan power is constant. The total power is thus:

$$P_{total} = P_{ucomp} + P_{lcomp} + P_{fan} \tag{3-1}$$

where $P$ refers to the power consumption, the subscripts 'total' refers total power consumption, 'ucomp', 'lcomp' and 'fan' refer to the upper compressor, lower compressor and evaporator fan. As the water inlet and outlet temperatures as well as the water mass flow rate are constant, the heat capacity of the condenser $\dot{Q}$ is constant, which can be calculated as:

$$\dot{Q} = \dot{m}_{water} c_p (T_{water,out} - T_{water,in}) = \dot{m}_{ref} (h_{ref,in} - h_{ref,out}) \tag{3-2}$$

where $\dot{m}$ refers to the mass flow rate, the subscripts 'water' and 'ref' refer to the condenser water and refrigerant, respectively. $T$ refers to temperature, and subscripts 'water,out' and 'water,in' refer to the water outlet and water inlet of the condenser, respectively. $h$ refers to enthalpy, subscripts 'ref,in' and 'ref,out' refer the refrigerant inlet and refrigerant outlet of the condenser, respectively. $c_p$ refers to the water specific heat capacity.

Then the COP of the IHXC water heat pump is the ratio of the heat capacity to the total power:

$$COP = \frac{\dot{Q}}{P_{total}} \tag{3-3}$$

Finally, the injection ratio $R_{inj}$ is defined as the ratio of the injected refrigerant mass flow rate $\dot{m}_{inj}$ to the condenser refrigerant mass flow rate $\dot{m}_{cond}$:

$$R_{inj} = \frac{\dot{m}_{inj}}{\dot{m}_{cond}} \tag{3-4}$$

In this model, the minimal total power corresponds to the maximum COP because of the constant heat capacity maintained throughout the simulated operation. The total power is adopted as the only ESC feedback rather than the COP, because power measurement is relatively simple and cost-effective while determination of COP requires several measurements of thermal and fluidic variables.

### 3.3 ESC Design for the IHXC ASHP Water Heater

For energy efficient operation of the IHXC-VI ASHP water heater system, the proposed ESC based control strategy takes the total power as the only feedback, and the intermediate pressure setpoint as the manipulated input. The proposed ESC controller is designed for the IHXC-VI ASHP water heater system as described in Section 3.1. For the condenser, the water inlet temperature is fixed at 50℃, and the water mass flow rate is set to be 0.5 kg $s^{-1}$, and the outlet temperature setpoint is 55℃. The ambient air temperature and relative humidity are set to be –20℃ and 50% respectively, and the mass flow rate of the evaporator fan is set to be 1.1 kg $s^{-1}$. The main loop superheat is set to be 5℃.

First, the input dynamic is estimated via the step response as shown in Figure 3.3, with the intermediate pressure setpoint changed from 9.0 to 9.25 bar, 9.25 to 9.5 bar and from 9.5 to 9.75 bar, respectively. As a conservative estimate, the input dynamic for ESC design is approximated based on the slowest response, i.e.

$$\hat{F}_I(s) = \frac{0.025^2}{s^2 + 2\times 1.212\times 0.025s + 0.025^2} \tag{3-5}$$

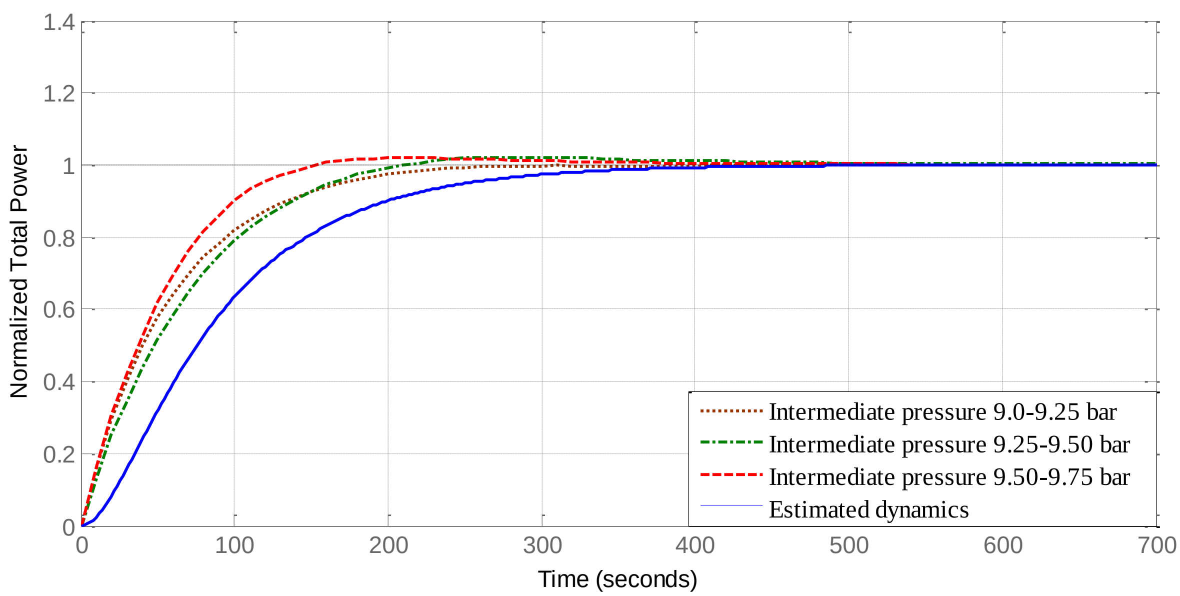


Figure 3.3. Step response for input dynamics estimation of IHXC-VI ASHP water heater.

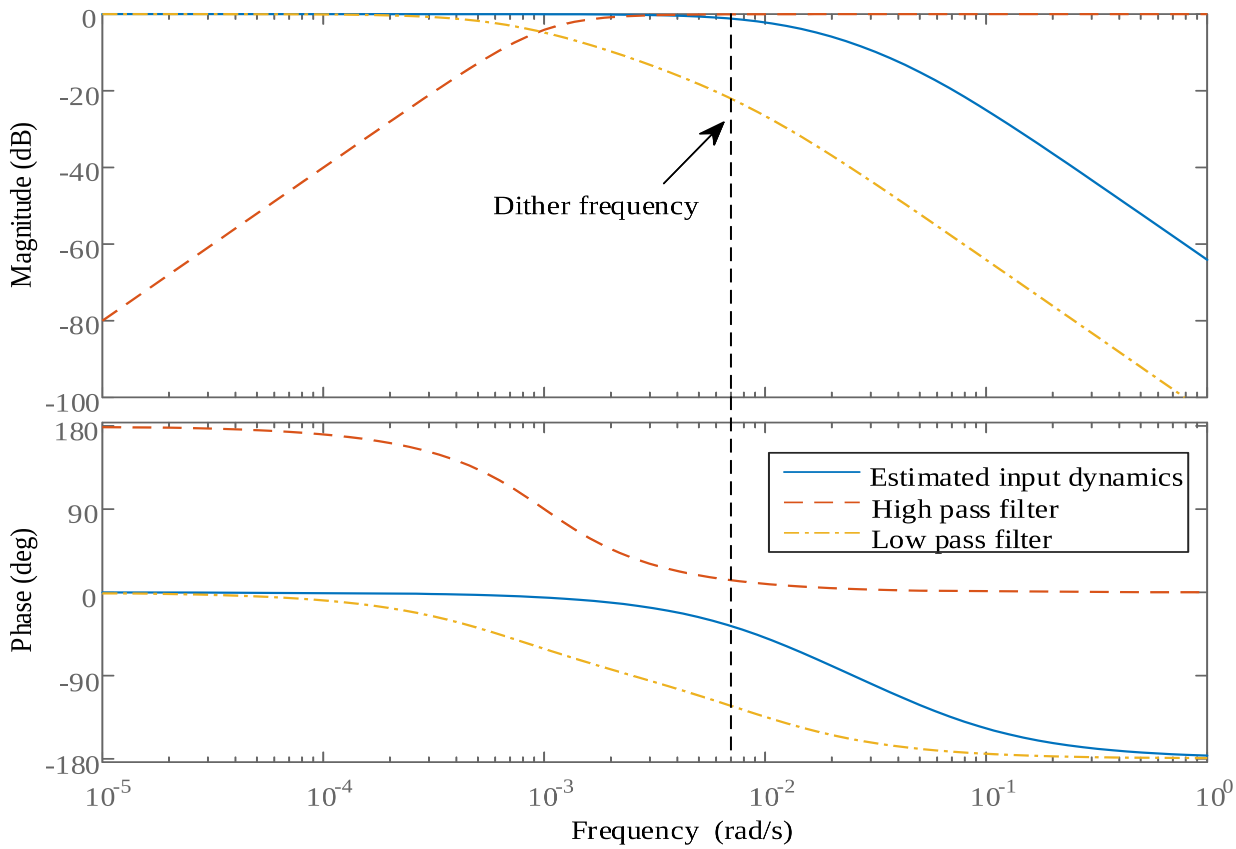


Figure 3.4. Bode plots for the estimated input dynamics, high-pass and low-pass filters.

The corresponding Bode plot is drawn in Figure 3.4. The dither frequency is chosen at 1.2 × $10^{-3}$ Hz, and the dither amplitude is selected as 6000 Pa. The high-pass and low-pass filters are designed as:

$$F_{HP}(s) = \frac{s^2}{s^2 + 2 \times 0.8 \times 0.001 s + 0.001^2} \tag{3-6}$$

$$F_{LP}(s) = \frac{0.0025^2}{s^2 + 2 \times 1.9 \times 0.0025 s + 0.0025^2} \tag{3-7}$$

The phase compensation for the chosen dither is $\alpha = -[\angle F_I(j\omega_d) + \angle F_{HP}(j\omega_d)] = -39.6^{\circ}$.

Besides the ESC implemented as an outer-loop controller for setpoint optimization, several inner-loop controllers are implemented to realize the necessary regulation of some key process variables. 1) The intermediate pressure of the injection loop is regulated by a PI controller by tuning the UEV opening. 2) A PI controller is used to regulate the water outlet temperature setpoint via the compressor speed. The water outlet temperature setpoint is 55°C. 3) A PI controller controls the main-loop superheat via tuning the LEV opening. The setpoint of the main-loop superheat is 5°C. The specific design specifications of the three PI controllers are shown in Table 3.2.

Table 3.2. Design specifications of the PI controllers

| | Proportional Gain ($k$) | Integral Time ($T_i$) | Initial Output of PI controller |
|---|---|---|---|
| Intermediate pressure PI | $1\times10^{-10}$ | 100 | $5\times10^{-8}$ |
| Superheat PI | $1\times10^{-6}$ | 100 | $2.5\times10^{-7}$ |
| Water outlet temperature PI | 1 | 5 | 50 |

### 3.4 Simulation Results

The ESC controller designed in the previous section is then implemented in the Dymola simulation model of the IHXC-VI ASHP water heater. Simulations are conducted for three scenarios: 1) fixed ambient temperature, 2) staircase profile of ambient temperature, and 3) a realistic ambient temperature profile.

To evaluate the performance of setpoint optimization for ESC, the optimum setting or trajectory for the given system configuration is obtained with the simulation based optimization procedure offered by the simulation platform. Dymola has offered several options within its

Optimization Library [180, 181]. The Optimization Library provides tools to benefit from numerical optimization algorithms without special knowledge about the internals of the algorithms. It helps set up the optimization runs conveniently by tailored Graphical User Interfaces (GUIs) for different tasks. For example, one is able to automatically optimize model parameters in order to improve the system performance assessed by some model variables. In this study, the Sequential Quadratic Programming (SQP) procedure in the Dymola Optimization Library (*Optimization.Tasks.ModelOptimization*) is adopted to find the 'true optimum' for the intermediate pressure setpoint. Sequential Quadratic Programming (SQP) is one of the most successful methods for the numerical solution of constrained nonlinear optimization problems. It can find an approximate solution of a sequence of quadratic programming (QP) subproblems in which a quadratic model of the objective function is minimized subject to the linearized constraints. SQP methods provide a relatively reliable "certificate of infeasibility" and they have the potential of being able to capitalize on a good initial starting point. Sophisticated matrix factorization updating techniques are used to exploit the fact that the linear equations change by only a single row and column at each inner iteration. These updating techniques are often customized for the particular QP method being used and have the benefit of providing a uniform treatment of ill-conditioning and singularity [182]. So the SQP method relies on a profound theoretical foundation and provides powerful algorithmic tools for the solution of large-scale problems. It can be used to solve a general nonlinear optimization problem and has usually a super-linear convergence with the aid of gradients of functions and constraints. In the simulation study of this chapter, the tolerance of SQP optimization is set as $1\times10^{-3}$.

### 3.4.1 ESC under fixed condition

ESC is first evaluated with the design condition described in Section 3.3. The static map for this fixed condition is shown in Figure 3.5, in which the minimum total power is 4,870 Watt at the intermediate pressure of 9.51 bar.

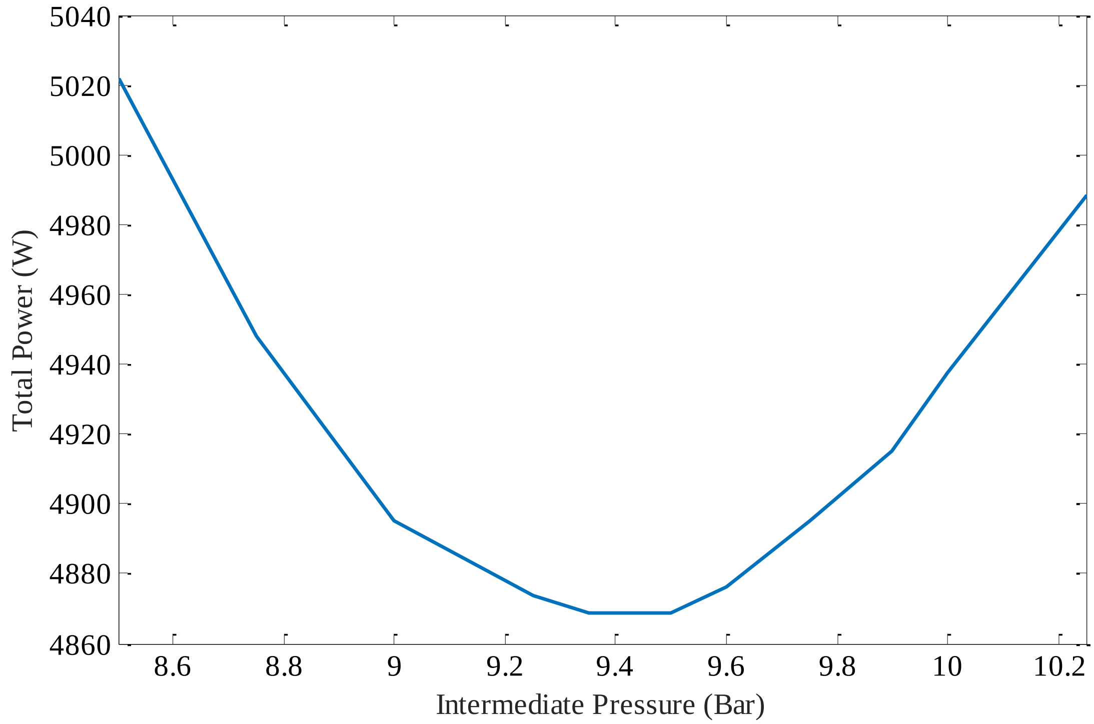


Figure 3.5. Static map of total power in terms of the intermediate pressure.

As shown in Figure 3.6, the ESC starts at $t$ = 1 hour, with the initial intermediate pressure of 8 bar. With less than 2 hours, ESC converges the intermediate pressure to 9.45 bar. Compared to the estimated optimum in the static map in Figure 3.5, the steady-state error is about 0.6%. Meanwhile, the UEV effective flow area increases from the initial value of $6.65\times10^{-2}$ mm$^2$ to $2.24\times10^{-1}$ mm$^2$, and the injection ratio increases from 12.7% to 32.5%. The trajectories of several other variables are shown in Figure 3.7. The total power converges to 4896.4 W from the initial value of 5277.6W, and the COP increases from 1.98 to 2.14. Compared to the calibrated optimum, the steady-state errors in terms of the total power and COP are about 0.9% and 0.8% respectively. The water outlet temperature is shown to be well regulated to its setpoint, and the compressor speed decreases from 64.9 Hz to 57.8 Hz throughout the extremum-seeking transient process.

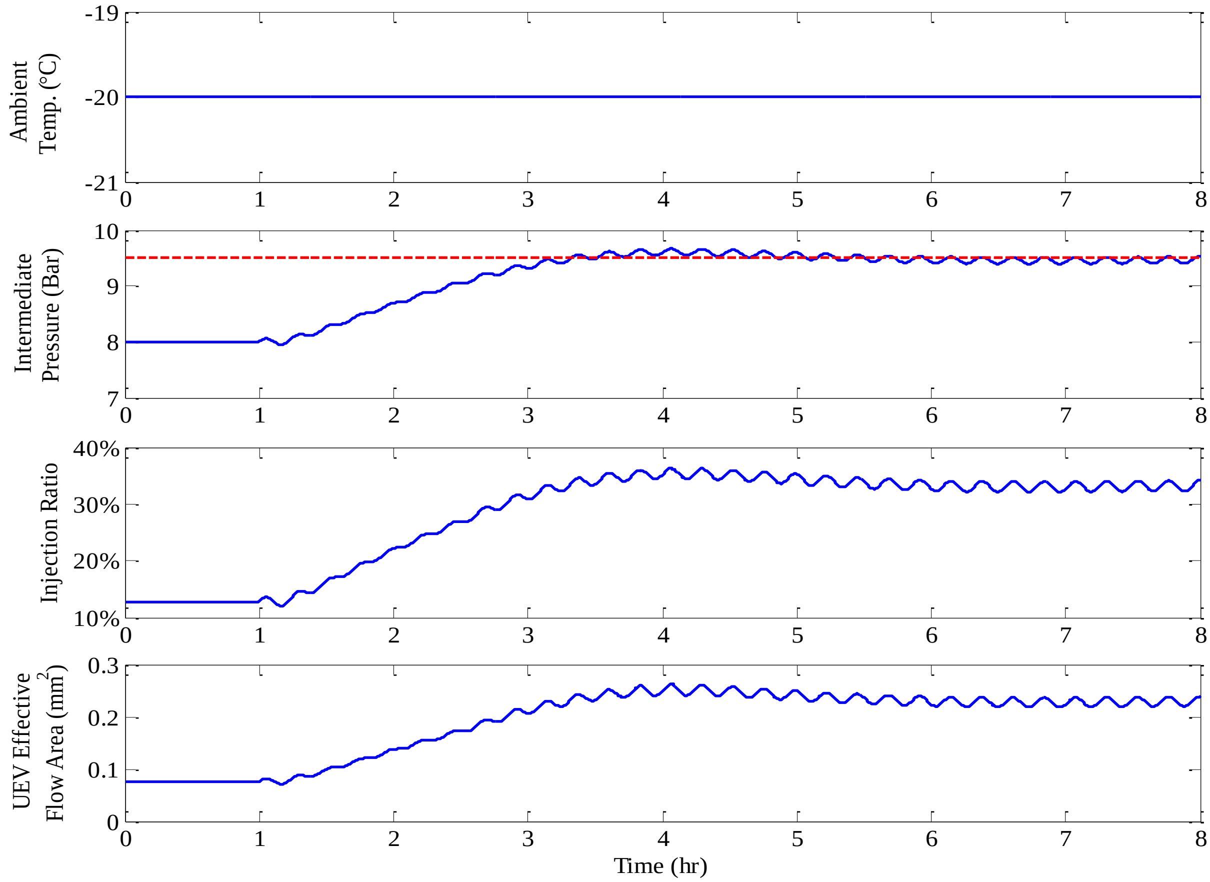


Figure 3.6. Trajectories of ambient temperature, intermediate pressure, injection ratio and UEV effective flow area for ESC simulation under fixed ambient temperature.

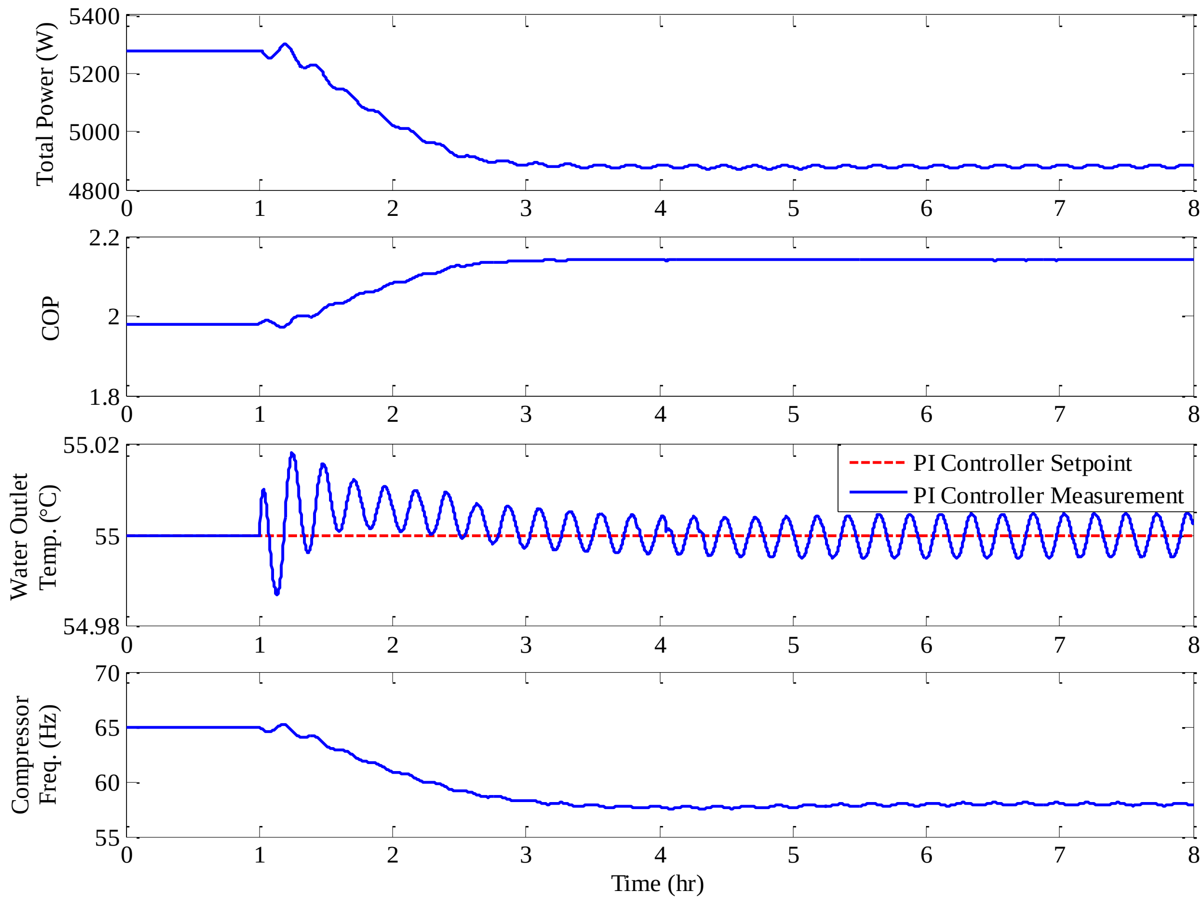


Figure 3.7. Trajectories of the total power, COP, water outlet temperature and compressor frequency for ESC simulation under fixed ambient temperature.

For evaluating the impact of the initial value, the ESC simulation is repeated by starting from three different initial values of intermediate pressure. Table 3.3 summarizes the steady-state values of input and output as well as the settling time. The results show that the converged steady-state value is very consistent with the previous results, while the settling time is affected by the initial value. As mentioned earlier, another inner-loop regulation control required for a valid operation of ESC is quality regulation of the main-loop superheat temperature. Figure 3.8 shows the trajectories of the main-loop superheat and the main-loop LEV opening, which justifies a sound regulation. Also, the ESC gradient estimate (i.e. the output of the low-pass filter) is shown, which converges to the neighborhood of zero, i.e. achieving the optimality.

Table 3.3. Summary of ESC performance under different initial values.

| Initial intermediate pressure (bar) | Steady-state intermediate pressure (bar) | Steady-state total power (W) | Settling time (s) |
|---|---|---|---|
| 9 | 9.55 | 4905.22 | 1920 |
| 10 | 9.58 | 4913.9 | 1280 |
| 11 | 9.60 | 4904.3 | 5950 |

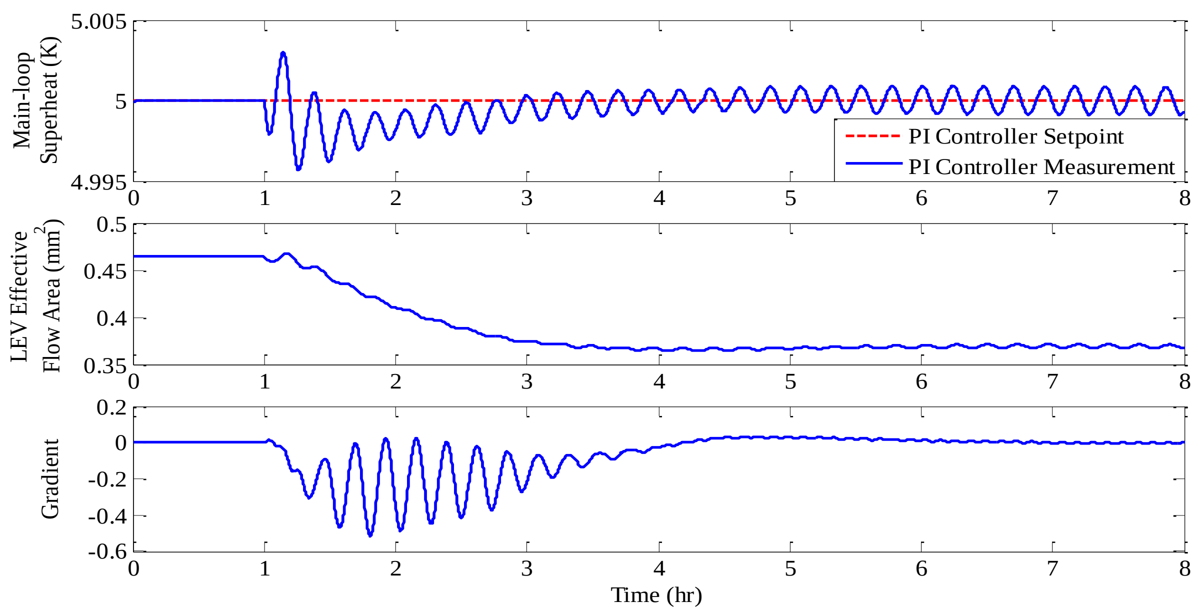


Figure 3.8. Trajectories of main-loop superheat, main-loop LEV opening, ESC Gradient for simulation under fixed ambient temperature.

### 3.4.2 ESC under staircase profile of ambient temperature

The ESC controller is then tested under a staircase profile of ambient temperature as shown in Figure 3.9, which starts from -15°C, and then goes down to –20°C, –25°C, –30°C sequentially, with

3600-second ramp for the first three steps and a 7200-second ramp at the final step back to -15℃. The interval for each temperature level is 12 hour. For the ESC operation, the trajectories of the intermediate pressure, injection ratio and effective flow area of the expansion valve are shown in Figure 3.9.

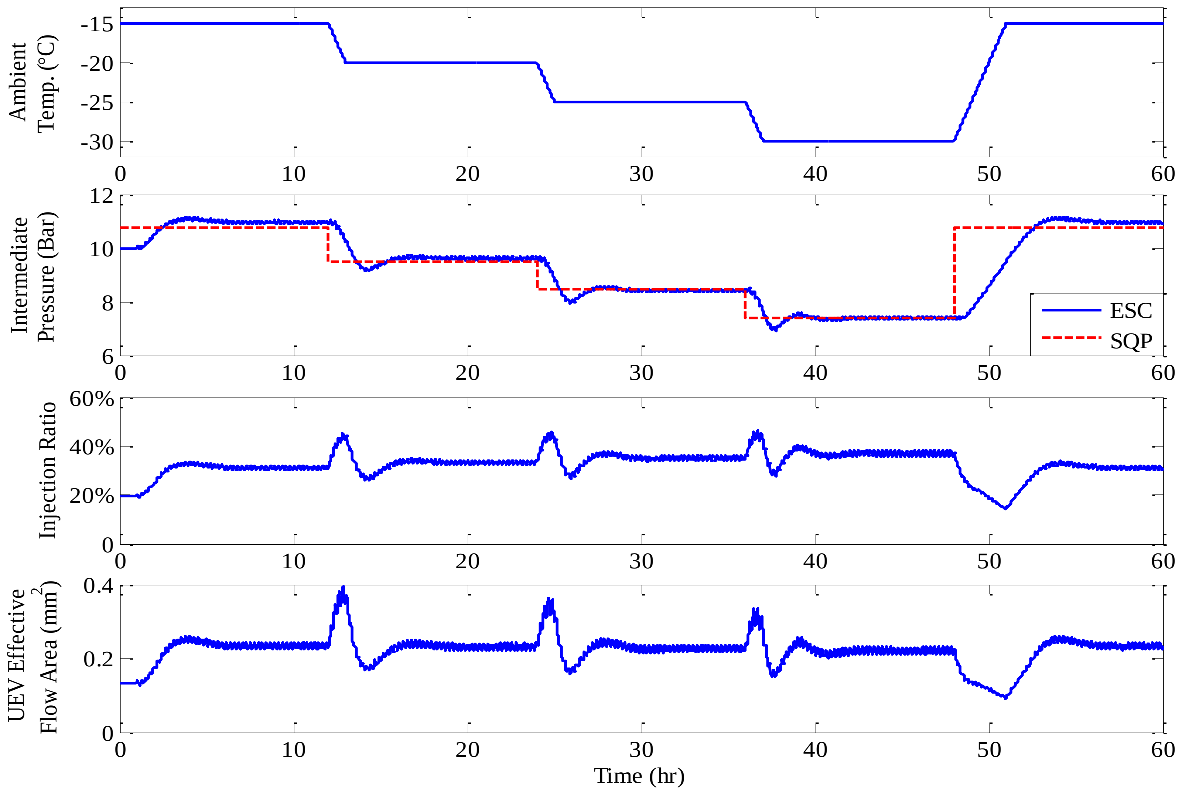


Figure 3.9. Trajectories of ambient temperature, intermediate pressure, injection ratio and UEV opening for ESC simulation under staircase change of ambient temperature.

ESC is turned on at $t$ = 1 hour, the steady-state intermediate pressure is 10.9, 9.58, 8.45, 7.4 and 10.9 bar, under the ambient temperature of -15℃, -20℃, -25℃, -30℃ and -15℃. These values are very close to the optimum intermediate pressure levels found by the SQP procedure that are plotted as red dashed lines. The maximal steady-state error is about 1.4% for the case of -15℃. The corresponding optimal injection ratio is 31%, 34%, 36% and 38% for the case of -15℃, -20℃,

-25℃ and -30℃, respectively, which is consistent with the profile of the effective flow area of the injection-loop expansion valve.

To illustrate the thermodynamic cycle of the heat pump system operation, the p-h diagrams for the ESC steady-state operation at each ambient temperature are shown in Figure 3.10. The constant-pressure heat rejection process in the condenser is shown as segment 4–5, and then the refrigerant is separated into two loops. The main-loop refrigerant flow is subcooled in segment 5-6, undergoes an isenthalpic expansion process through the main-loop expansion valve with segment 6-7, and then absorbs the heat under constant-pressure from the ambient air for segment 7-1. In parallel, the injection-loop refrigerant flow first undergoes an isenthalpic expansion process from point 5 to point 8, and then passes the internal heat exchanger with constant pressure to cool down the main-loop refrigerant. Then the refrigerant at point 1 (compressor suction port) is compressed and then mixed with the injection-loop superheat vapor to point 3. Finally the mixed refrigerant is compressed to point 4, completing the full cycle. Notice that the states corresponding to points 2 and 9 in Figure 1.5 coincide with point 3 because of the nature of the simplified modeling scheme adopted for the vapor injection compressor. It can be observed, under the staircase ambient temperature profile, the condensing pressure is nearly the same because of the same water inlet and outlet temperature. However, the optimal intermediate pressure varies significantly more under different ambient temperatures, which manifests the significance for real-time optimization of the intermediate pressure with ESC when the ambient temperature varies.

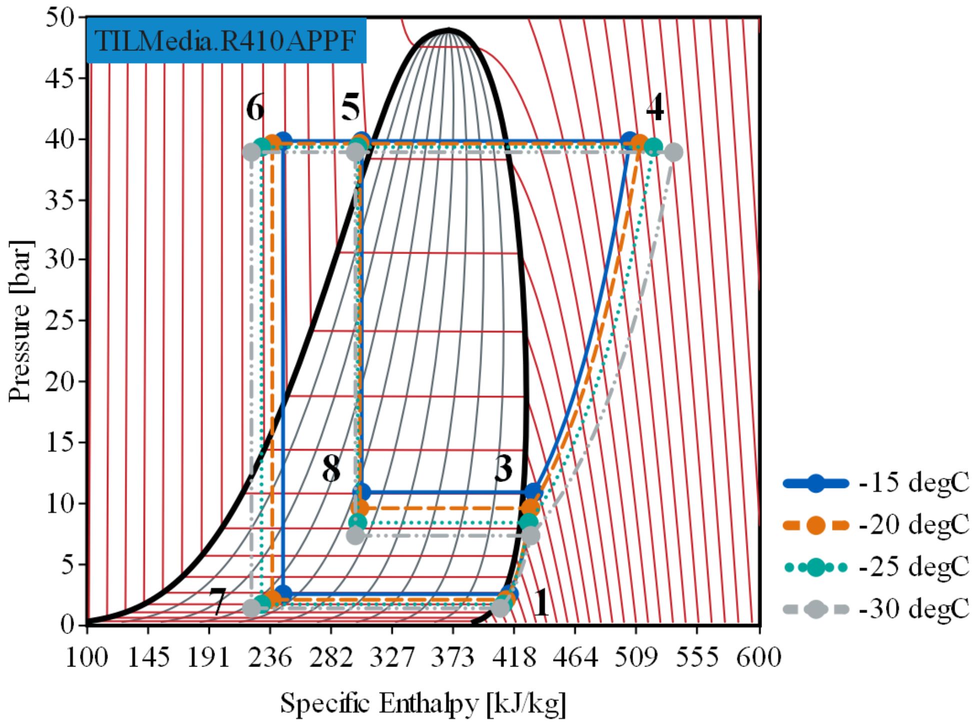


Figure 3.10. p-h diagrams of ESC stead-state operation under different ambient temperatures.

Figure 3.11 shows that, at the ESC steady state for each ambient temperature level, the total power converges to 4634.5W, 4904.2W, 5212.9W and 5530.5W, respectively, and the COP converges to 2.25, 2.13, 2.0 and 1.89, respectively. Meanwhile, the water outlet temperature remains well regulated to its setpoint with smooth variations of the compressor frequency. Similar to the case of fixed condition, the trajectories of the main-loop superheat and the LEV opening are shown in Figure 3.12, which indicates a quality inner loop control. Also shown in Figure 3.12 is the ESC gradient trajectory. For each ambient temperature, the ESC gradient converges to zero respectively.

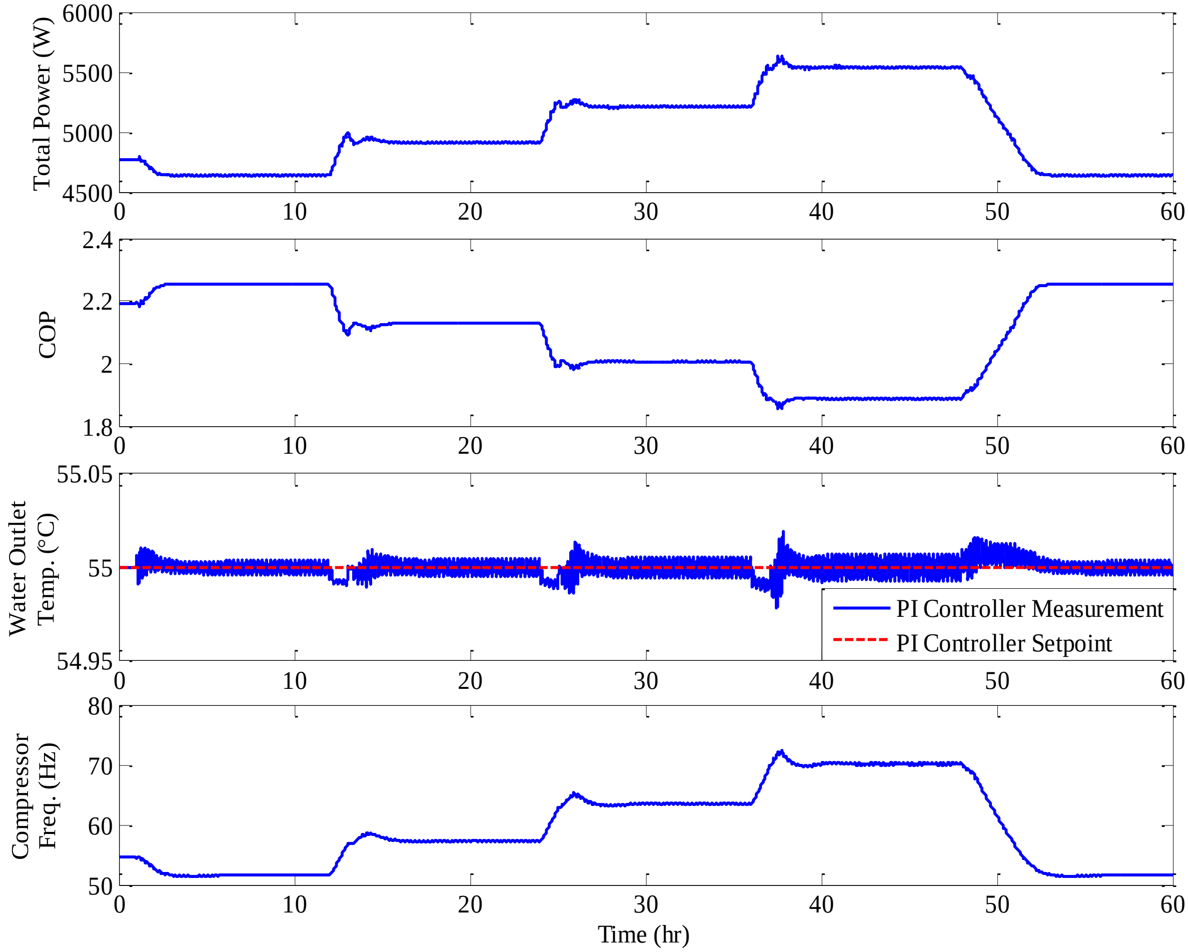


Figure 3.11. Trajectories of the total power, COP, water outlet temperature and compressor frequency for ESC simulation under staircase change of ambient temperature.

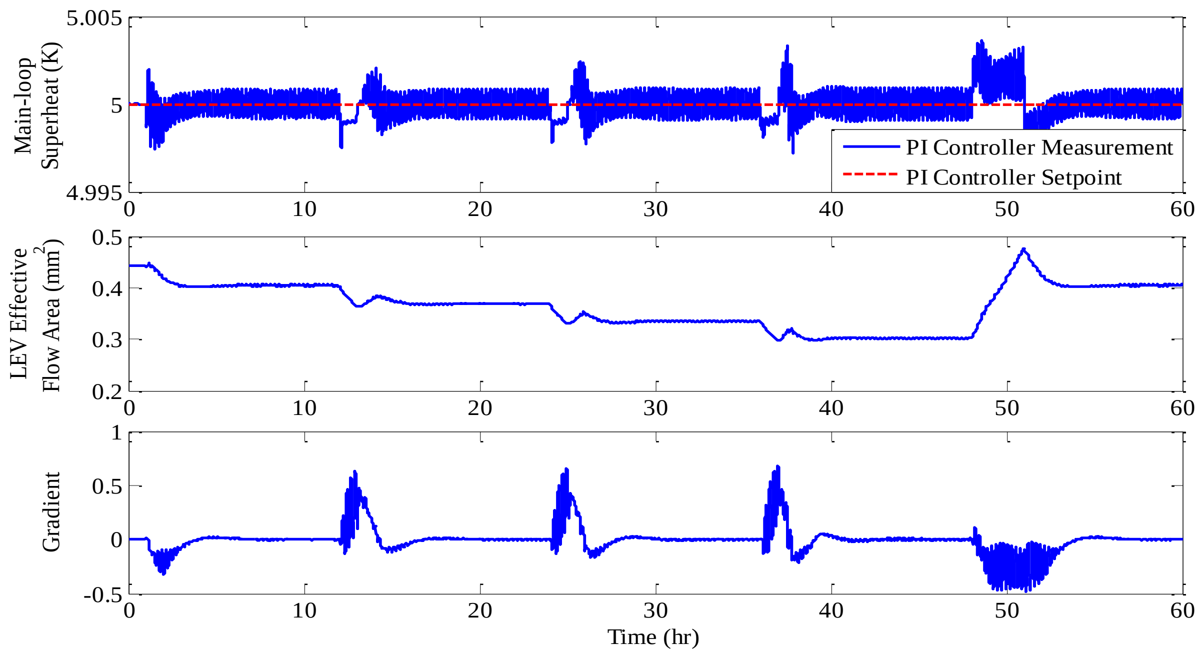


Figure 3.12. Trajectories of main-loop superheat, main-loop LEV opening and ESC gradient for ESC simulation under staircase change of ambient temperature.

### 3.4.3 ESC under realistic ambient temperature profile

Finally, the ESC control strategy is tested under a realistic ambient temperature profile. As shown in Figure 3.13, a 96-hour ambient temperature profile of Fairbanks, Alaska (January 1st through 4th) is adopted from the TMY3 data (*Buildings.BoundaryConditions.WeatherData.ReaderTMY3*), and all other settings are same as the previous cases. The initial intermediate pressure and injection ratio is 9 bar and 6%, respectively, and the ESC is turned on at t = 2 hour. The trajectories of the intermediate pressure, injection ratio and the EEV effective flow area are shown in the figure. After the ESC is turned on, the intermediate pressure and injection ratio rise up to the optimal values of 11.1 bar and 32%, respectively, when the ambient temperature is around −15°C. Afterwards, the intermediate pressure changes smoothly by following the change of the ambient temperature. Meanwhile, the injection ratio increases slowly to the maximum of 39% and then decreases to 28%, corresponding to the change of ambient temperature from around −14°C to −27.8°C, and then back up to −12.2°C.

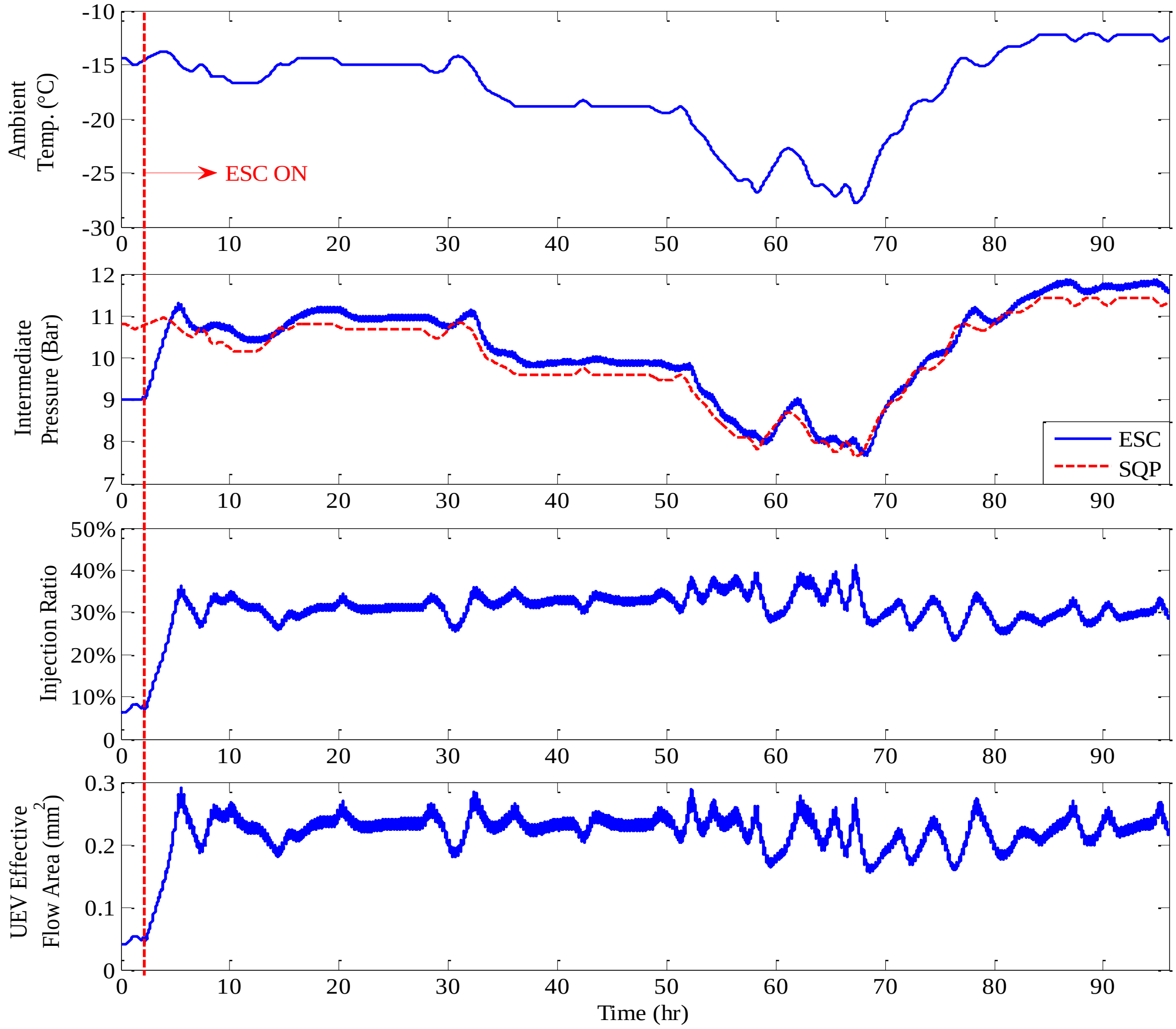


Figure 3.13. Trajectories of ambient temperature, intermediate pressure, injection ratio and UEV effective flow area for ESC simulation under a realistic ambient temperature profile.

To better evaluate the tracking capability of ESC under dynamic ambient temperature profile, the intermediate pressure trajectory by ESC is compared with that found by the SQP, as also shown in Figure 3.13. As for the aforementioned range of ambient temperature, the intermediate pressure changes from the maximum of 11.85 bar to the minimum of 7.67 bar. The blue solid line is the result found by ESC, while the red dashed line is the optimal value found by SQP. The SQP optimum values are found for each ambient temperature from -12°C to -28°C, with increment of 0.1°C. It reveals that the optimal intermediate pressure searched by ESC is very close to the result of SQP, with the maximal error of about 1.5% throughout the whole simulation, in spite of some delay.

The trajectories of total power and COP are then compared in Figure 3.14, which also supports the capability of ESC in dynamically tracking the actual optimum found by SQP in real time. As for load demand satisfaction, the water outlet temperature is well regulated to the 55℃ setpoint throughout the dynamic process with smooth trajectory of compressor frequency. Also, as shown in Figure 3.15, the main-loop superheat temperature is well regulated with a reasonably smooth profile of the LEV opening. The ESC gradient is also plotted in Figure 3.15. Under such dynamically varied ambient temperature, there is barely any true steady state, while ESC shows its efforts in steering the gradient towards zero all the time. It is noteworthy that the realistic ambient temperature is nearly constant for two intervals that are marked with two solid black lines and two dash black lines. It reveals that the gradient converges well to zero for these two intervals.

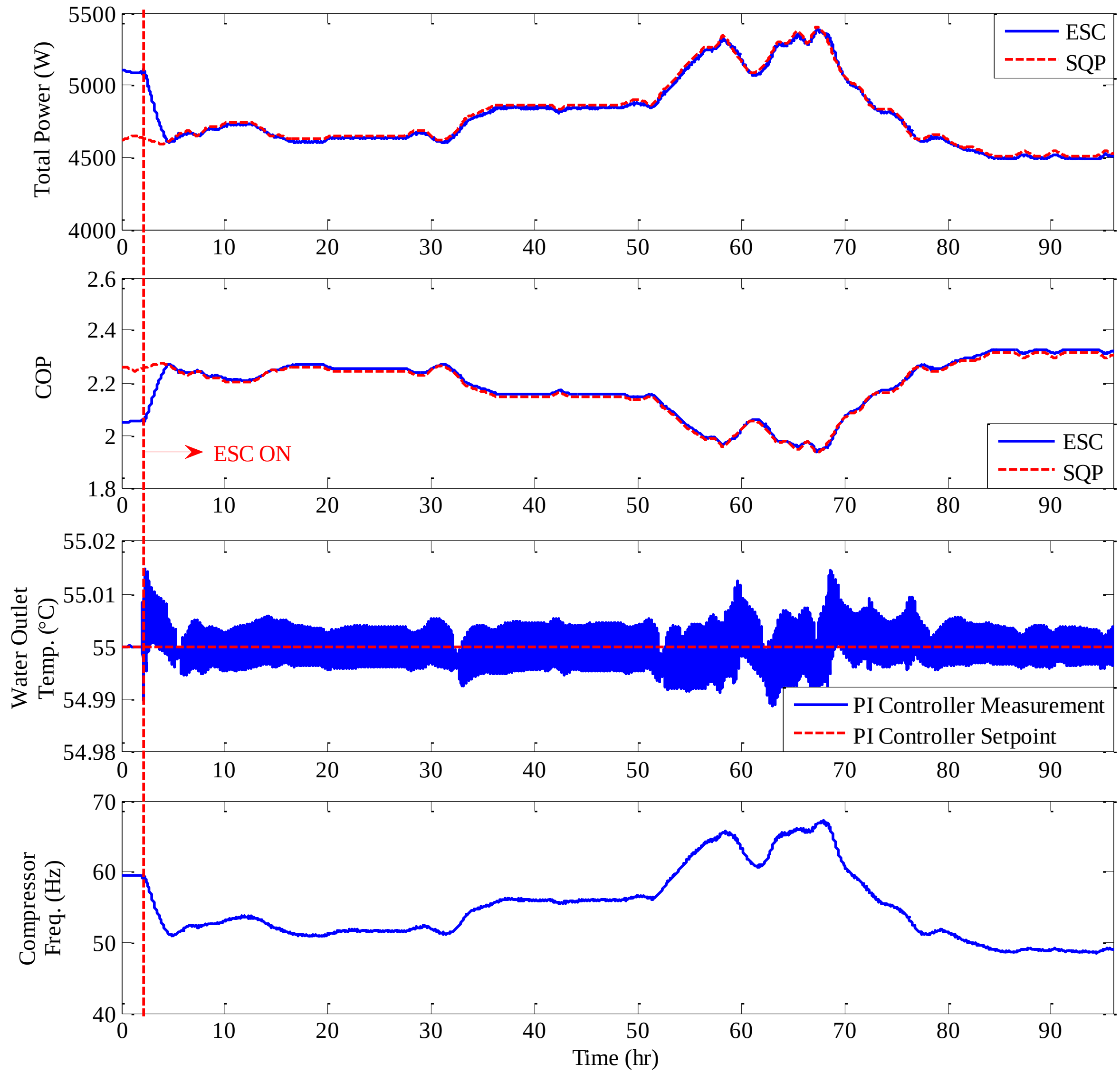


Figure 3.14. Trajectories of the total power, COP, water outlet temperature and compressor frequency trajectories for ESC simulation under a realistic ambient temperature profile.

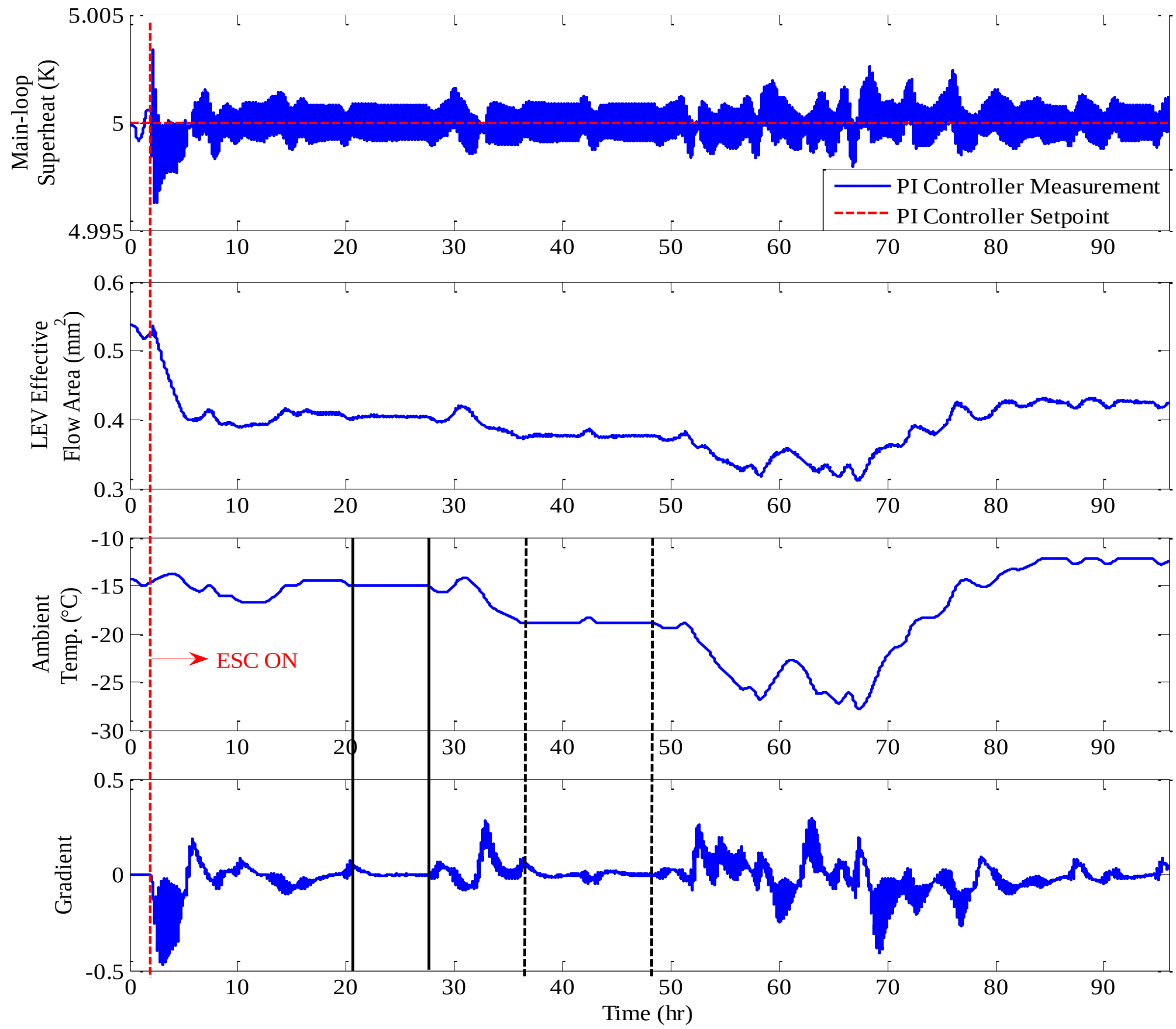


Figure 3.15. Trajectories of main-loop superheat, main-loop LEV opening and ESC gradient for ESC simulation under a realistic ambient temperature profile.

### 3.5 Summary

In this chapter, an ESC based control strategy for efficient operation of an IHXC-VI ASHP water heater system is proposed, in which the total power consumption is minimized by tuning the intermediate pressure setpoint provided that the heating load is regulated consistently. To evaluate the proposed control strategy, a Modelica-based dynamic simulation model is developed for the system of interest using Dymola and TIL Library. The simulation is conducted under three ambient conditions, i.e. fixed, staircase and realistic ambient temperature profile. The results show good performance of tracking the optimum operating point with reasonable convergence rate, even for the realistic ambient profile ranging from -12.2℃ to -27.8℃. Maintaining optimal operation for IHXC-VI heat pump systems has been a major challenge for HVAC practice due to the complexity in the inherent thermodynamic process and impact of load and ambient conditions. The proposed ESC framework promises a model-free control strategy with minimum sensing requirement.

# CHAPTER 4

# OPTIMIZATION OF AN AIR-SOURCE HEAT PUMP WITH FLASH TANK CYCLE VAPOR INJECITON*

This chapter presents the dynamic simulation modeling and a Newton based ESC strategy for optimizing a vapor injection air source heat pump water heater with flash tank.

## 4.1 Introduction and Research Motivation

Compared to an ASHP with IHXC, the flash tank cycle (FTC) has the merits of low cost and inherent higher efficiency. For FTC, the injected medium is the saturated vapor from the flash tank, which in principle bears a lower temperature than the superheated vapor being injected for the case of IHXC. This helps reduce the compressor discharge temperature and thus the power consumption. However, the FTC technique has been far behind IHXC in adoption by practical ASHP systems, in spite of its superior performance and cost-effectiveness. The major obstacle is the lack of proper control/operational strategy for its vapor injection loop. As reviewed in Chapter 1, the control strategies proposed in some recent research [89, 90] mostly focus on heating the injected vapor from the flash tank to achieve some degree of superheat. Such levitation of the temperature of the injection medium inherently leads to lower thermodynamic efficiency compared to the use of saturated vapor in the standard FTC design, in addition to the efficiency loss due to additional heating. Also, the use of a heating element increases the system complexity and cost.

A desirable control method for FTC-VI ASHP should achieve stable operation, maintain a reasonable range of liquid level, and obtain the maximum achievable thermal performance offered by the FTC in cost-effective fashion. In this chapter, a novel control strategy is proposed for an FTC-VI based two-stage ASHP, which includes two aspects: 1) the intermediate pressure level is regulated by the UEV opening, and 2) the intermediate pressure level is optimized online with respect to the total power consumption of the system using the Extremum Seeking Control (ESC). With this control strategy, three benefits can be obtained: i) the UEV is still used to regulate the thermodynamic characteristic of the injected medium, but does not manage to introduce any nontrivial superheat that would sacrifice the thermal efficiency; ii) the liquid level in the flash tank can be maintained within a safe and proper range during the operation; and iii) the optimum efficiency while satisfying the heating load in addition to safe and stable operation.

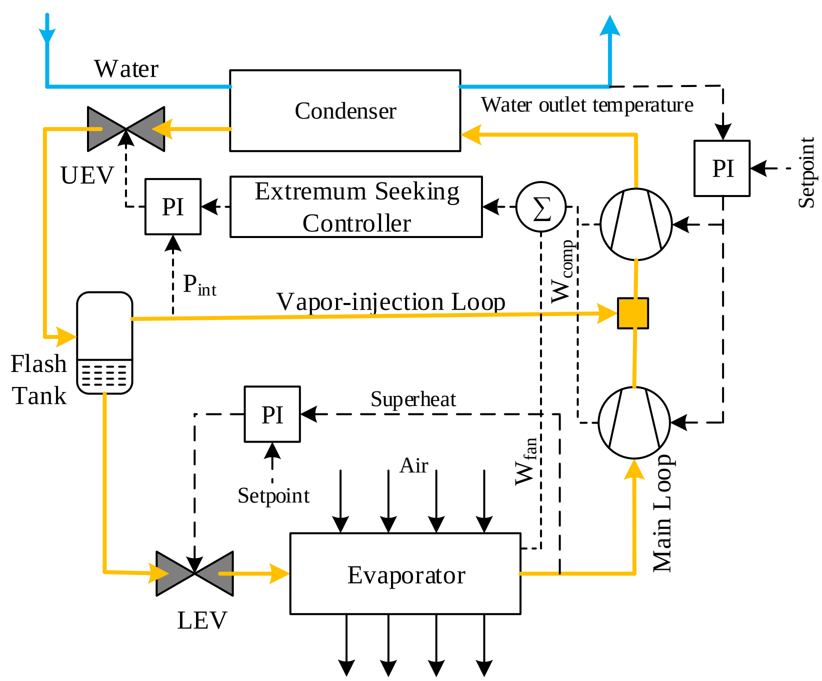


Figure 4.1. Schematic diagram for the ESC based operation for FTC-VI two-stage ASHP.

Figure 4.1 shows the ESC strategy proposed for the FTC-VI based two-stage ASHP water heater system. The intermediate pressure setpoint of the injection-loop vapor is used as the manipulated input of ESC, while the total power consumption of the system is the only feedback. The UEV opening is used to regulate the intermediate pressure to the setpoint specified by the ESC, and the water outlet temperature is regulated by the compressor capacity. The ESC loop, if asymptotically stable, minimizes the total power consumption (i.e. maximizes the energy efficiency). Such control strategy retains the merit of supplying saturated vapor in the vapor-injection loop, i.e. does not undermine the achievable efficiency of the standard FTC design. Also, it does not need any additional actuation device such as a heating element or heat exchanger. Another merit of the proposed framework is that cost-effective power measurement is readily available, while online evaluation of COP is quite costly due to the need for measuring several thermofluid variables.

## 4.2 Dynamic Simulation Modeling of FTC Based VI Two-stage ASHP System

For evaluating the proposed control strategy, a Modelica based dynamic simulation model of an FTC-VI two-stage ASHP is developed using Dymola 2017 [13] and TIL Library 3.5.0 [14, 15], with the Dymola layout shown in Figure 4.2. The intermediate pressure is regulated by the UEV opening by an inner-loop proportional-integral (PI) controller. For the ESC loop, the intermediate pressure setpoint is used as the manipulated input, and the total power is the only feedback. The capacity of the upper compressor and lower compressor is used to regulate the water outlet temperature via another PI controller simultaneously, which results in constant heating capacity under fixed water inlet temperature and fixed water flow mass rate. The LEV is used in the main loop with another PI controller to maintain a proper degree of superheat for the primary loop.

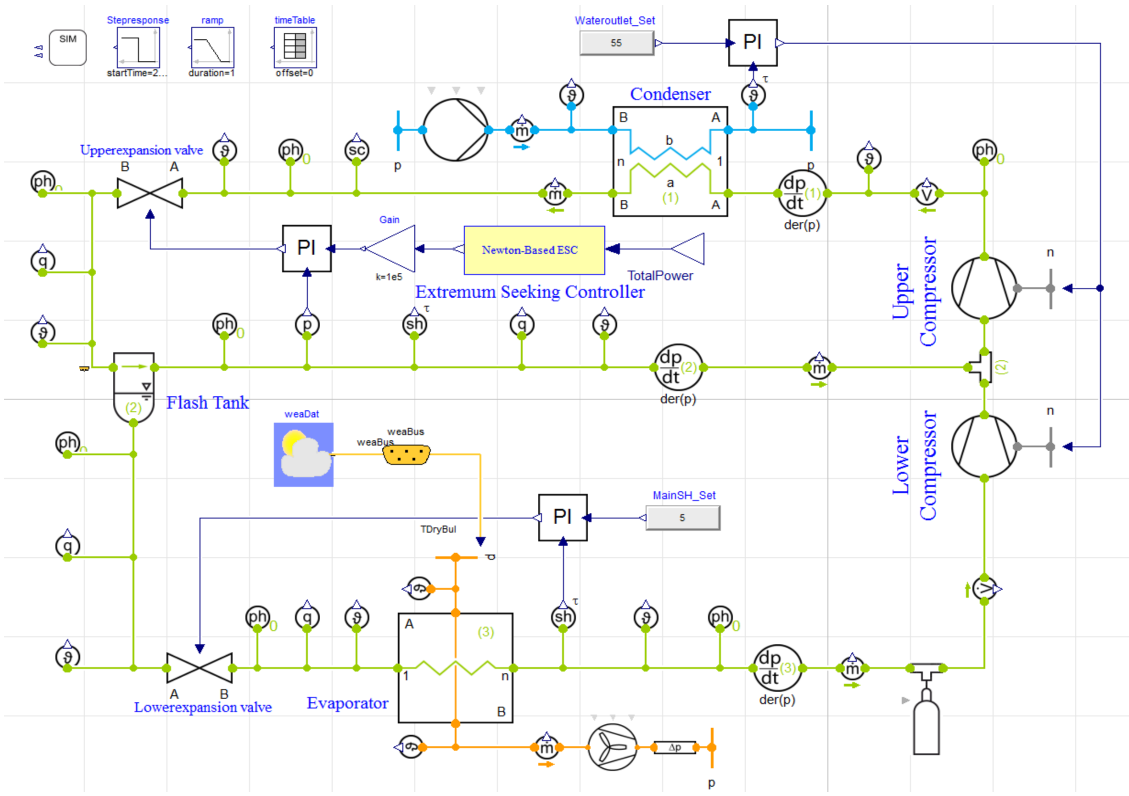


Figure 4.2. Dymola layout for the FTC-VI two-stage ASHP water heater model.

### 4.2.1 Dynamic modeling of major components

The compressors are modeled by adopting the scroll compressor module in the TIL Library (*TIL.VLEFluidComponents.Compressors.ScrollCompressor*), and the injected saturated vapor is mixed with the vapor from the lower compressor in the junction module (*TIL.VLEFluidComponents.JunctionElements.VolumeJunction*). A displacement ratio of 42% is reinforced for the two compressors, based on what is given by reference [72]. In addition, the frequencies of the two compressors are adjusted simultaneously by the PI controller.

The mathematical description for the scroll compressor model is presented in Appendix A. The flash tank is an equipment for separating the two-phase refrigerant mixture into two single-phase flows that exit from different ports. In this study, the separator model in TIL

(*TIL.VLEFluidComponents.Separators.Separator*) is enhanced by adopting the modeling framework by Qiao et al. [75]. As shown in Figure 4.3, the flash tank is modeled as an adiabatic volume with ideal mixing process, with the pressure drop neglected.

The transient energy and mass balances are formulated as

$$\frac{d\bar{h}}{dt} = \frac{1}{\rho_{FT} V_{FT}} \left[ \dot{m}_{in}(h_{in} - \bar{h}) - \dot{m}_{lo}(h_{lo} - \bar{h}) - \dot{m}_{vo}(h_{vo} - \bar{h}) + V_{FT} \frac{dp_{FT}}{dt} \right] \tag{4-1}$$

$$V_{FT} \cdot \frac{d\rho_{FT}}{dt} = \dot{m}_{in} - \dot{m}_{lo} - \dot{m}_{vo} \tag{4-2}$$

where $\bar{h}$ refers to the mass-based mean enthalpy. $h$ and $\dot{m}$ refer to the enthalpy and mass flow rate, respectively, subscripts 'in', 'lo' and 'vo' refer to the flash tank inlet, liquid outlet and vapor outlet, respectively. $\rho$, $V$ and $p$ refers to the density, volume and pressure, respectively. Subscript 'FT' refers to the flash tank. $t$ refers to the time.

The enthalpies of the discharge vapor and liquid streams are dependent on the state of the refrigerant in the flash tank. Based on Qiao et al. [75], the leaving enthalpies of two outlet streams are determined as

$$h_{lo} = \begin{cases} h_f & H_{liq} > H_{lo} + d_{liq} \\ h_g - \left( \dfrac{H_{liq} - H_{lo}}{d_{liq}} \right) \left( h_g - h_f \right) & H_{lo} + d_{liq} \geq H_{liq} \geq H_{lo} \\ h_g & H_{liq} < H_{lo} \end{cases} \tag{4-3}$$

$$h_{vo} = \begin{cases} h_f & H_{liq} > H_{vo} + d_{vap} \\ h_g - \left( \dfrac{H_{liq} - H_{vo}}{d_{vap}} \right) \left( h_g - h_f \right) & H_{vo} + d_{vap} \geq H_{liq} \geq H_{vo} \\ h_g & H_{liq} < H_{vo} \end{cases} \tag{4-4}$$

where $H$ and $d$ refer to the height and diameter of the tank, as shown in Figure 4.3. Subscripts '$g$', '$f$', '$liq$' and '$vap$' refer to saturated vapor, saturated liquid, liquid and vapor, respectively. The normalized liquid level of the flash tank $\delta_{liq}$ can be found by

$$\delta_{liq} = \frac{(h_g - \bar{h})\rho}{\rho_f (h_g - h_f)} \tag{4-5}$$

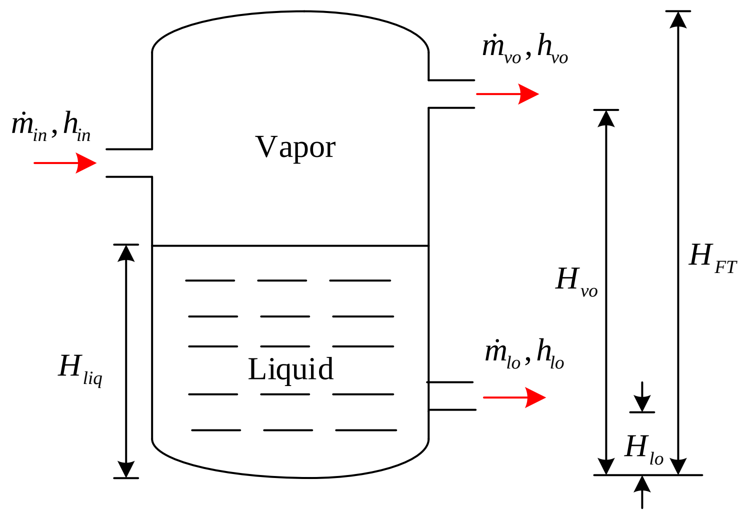


Figure 4.3. Schematic diagram for the flash tank for FTC-VI heat pump [75].

The water-heating condenser is modeled with the tube-and-tube heat exchanger module (*TIL.HeatExchangers.TubeAndTube.VLEFluidLiquid.ParallelFlowHX*). The fin-and-tube cross heat exchanger module (*TIL.HeatExchangers.FinAndTube.MoistAirVLEFluid.CrossFlowHX*) is used to model the evaporator, which can handle the latent heat transfer due to the moist air when applicable. The orifice valve module (*TIL.VLEFluidComponents.Valves.OrificeValve*) is used to model the expansion valve, which calculates the mass flow rate with dependency on the pressure drop using the Bernoulli Equation, with the effective flow area used as the input variable. The evaporator fan is modeled with a simple fan module (*TIL.GasComponents.Fans.SimpleFan*), whose operation can defined with pressure differential or mass flow rate. The water pump is modeled with the (*TIL.LiquidComponents.Pumps.SimplePump*) module, which is an affinity-law based pump model. In this study, the mass flow rate for the air side of the evaporator and the water side of the condenser are both set as constant. Table 4.1 shows the specific specifications designed for the FTC ASHP system.

Table 4.1. Design specifications of major components of FTC-VI two-stage heat pump.

| Components | Design specifications |
| --- | --- |
| Compressors | Scroll compressor; displacement: $72\times10^{-6}$ m$^3$ for lower and $30\times10^{-6}$ m$^3$ for upper; variable speed. |
| Condenser | Tube-and-tube heat exchanger; counter flow; copper; refrigerant tube: $\Phi$7.92 mm, number of parallel tubes 7; water tube: stainless steel, DN50, number of parallel tubes 1; tube length: 4.5 m. |
| Evaporator | Fin-and-tube heat exchanger; staggered copper tubes; tube diameter 7mm; wall thickness: 1.5 mm; number of serial tubes 3; number of parallel tubes 16; fin spacing 2.2 mm; thickness 0.2 mm; number of parallel tube side flows 6; tube length 0.8 m. |
| FTC | Height 0.32 m; Volume 0.0015 m$^3$. |
| Evaporator fan | Fan efficiency: 0.4; nominal air mass flow rate: 1.4 kg s$^{-1}$ |
| Expansion valve | Electronic expansion valve; typical effective flow area: 0.2×10-6 m$^2$; number: 2. |

### 4.2.2 Performance evaluation

The total power consumption is comprised of the power of the two compressors and that of the evaporator fan. The power consumption of compressor is variable under change of operational conditions. In this study, the evaporator fan speed is fixed, so the fan power is constant. The total power is thus:

$$P_{total} = P_{ucomp} + P_{lcomp} + P_{fan} \tag{4-6}$$

where P refers to the power consumption, the subscripts '*total*' refers total power consumption, '*ucomp*', '*lcomp*' and '*fan*' refer to the upper compressor, lower compressor and evaporator fan.

As the water inlet and outlet temperatures as well as the water mass flow rate are constant, the heat capacity of the condenser $\dot{Q}$ is constant, which can be calculated as:

$$\dot{Q} = \dot{m}_{water} c_p (T_{water,out} - T_{water,in}) = \dot{m}_{ref} (h_{ref,in} - h_{ref,out}) \tag{4-7}$$

where $\dot{m}$ refer to the mass flow rate, the subscripts '*water*' and '*ref*' refer to the condenser water and refrigerant, respectively. $T$ refers to temperature, and subscripts 'water,out' and 'water,in' refer to the water outlet and water inlet of the condenser, respectively. $h$ refers to the enthalpy, subscripts '*ref,in*' and '*ref,out*' refer the refrigerant inlet and refrigerant outlet of the condenser, respectively. $c_p$ refers to the water specific heat capacity.

The COP of the FTC-VI two-stage ASHP water heater is defined as the ratio of the heat capacity to the total power:

$$COP = \frac{\dot{Q}}{P_{total}} \tag{4-8}$$

Finally, the injection ratio $R_{inj}$ is defined as the ratio of the injected refrigerant mass flow rate $\dot{m}_{inj}$ to the condenser refrigerant mass flow rate $\dot{m}_{cond}$:

$$R_{inj} = \frac{\dot{m}_{inj}}{\dot{m}_{cond}} \tag{4-9}$$

In this model, the minimal total power corresponds to the maximum COP because of the constant heating capacity maintained throughout the simulated operation. The total power is adopted as the only ESC feedback rather than the COP, because power measurement is relatively simple and cost-effective while determination of COP requires several measurements of thermal and fluidic variables.

### 4.3 ESC Design for FTC based Vapor Injection Two-stage Air Source Heat Pump

The convergence characteristic of the gradient ESC is heavily affected by the Hessian of the underlying static map for the plant. For systems with nearly quadratic map that has relatively constant Hessian, the convergence rate is nearly consistent regardless the initial condition. However, for static maps with large variation in Hessian, the convergence rate of ESC can vary significantly with the initial value. In this study, the static map of the total power in terms of intermediate pressure is asymmetric as shown in Figure 4.4. To achieve more consistent convergence regardless the initial value being at either side of the optimum, the Newton-based ESC as reviewed in Chapter 2 is used.

#### 4.3.1 Gradient and Newton-based ESC design for FTC-VI two-stage ASHP water heater

The Gradient ESC controller for the FTC-VI two-stage ASHP water heater system is designed for a specific operating condition. The hot water inlet temperature is fixed at 50℃, and the water mass flow rate is set to be 0.5 kg/s. The outlet water temperature is regulated to 55℃ by compressor speed via a PI controller, i.e. the total heat transfer rate across the condensing heat exchanger is approximately constant. The ambient air temperature and relative humidity are set to be −20℃ and 50% respectively, and the mass flow rate of evaporator fan is set to be 1.4 kg/s. The superheat setpoint for the primary loop is 5℃. Figure 4.4 shows the static maps of the total power in terms of the intermediate pressure and the liquid level, respectively. The minimum total power of 4789.8

Watt is achieved at the intermediate pressure of 10.1 bar, where the corresponding liquid level is 38%. Notice that the liquid level increases monotonically with the intermediate pressure.

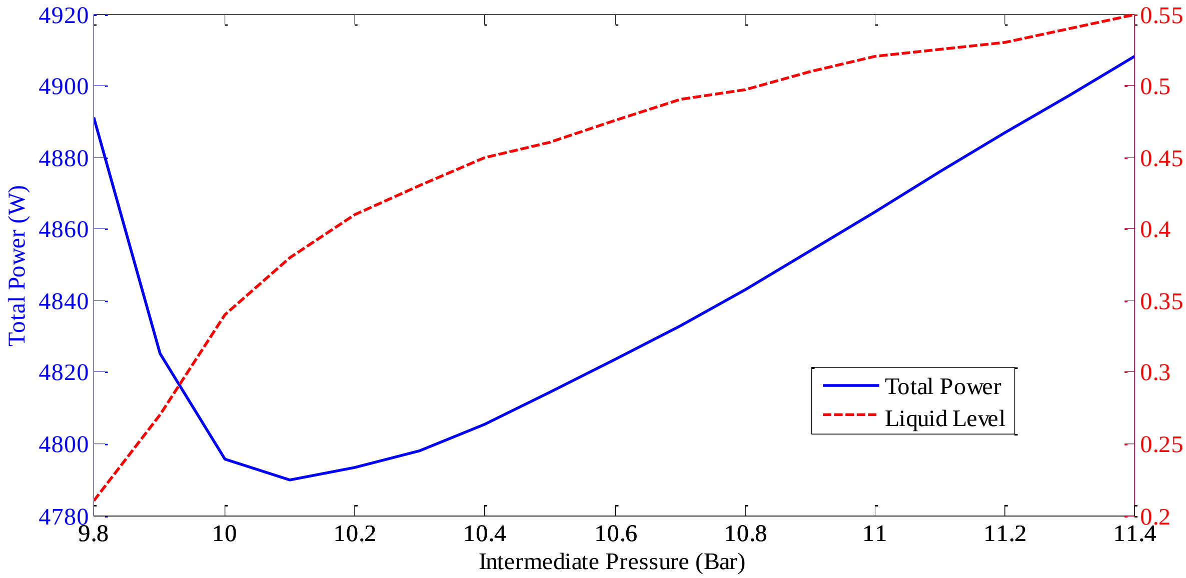


Figure 4.4. Static maps of total power in terms of intermediate pressure and liquid level for the FTC-VI two-stage ASHP water heater.

For ESC design, several open-loop step tests are simulated, with the normalized responses shown in Figure 4.5. The input dynamic is estimated as

$$\hat{F}_I(s) = \frac{0.011^2}{s^2 + 2\times 0.75\times 0.011s + 0.011^2} \tag{4-10}$$

The Bode plot of the input dynamics is shown in Figure 4.6. The dither frequency is chosen as 0.0012 Hz, and the dither amplitude is selected as 4000Pa.

The high-pass and low-pass filters are chosen as:

$$F_{HP}(s) = \frac{s^2}{s^2 + 2\times 0.8\times 0.001s + 0.001^2} \tag{4-11}$$

$$F_{Lp}(s) = \frac{0.0025^2}{s^2 + 2\times 1.9\times 0.0025s + 0.0025^2} \tag{4-12}$$

The phase compensation for the chosen dither should be

$$\alpha = -\left[\angle F_I(j\omega_d) + \angle F_{HP}(j\omega_d)\right] = 51.4° \tag{4-13}$$

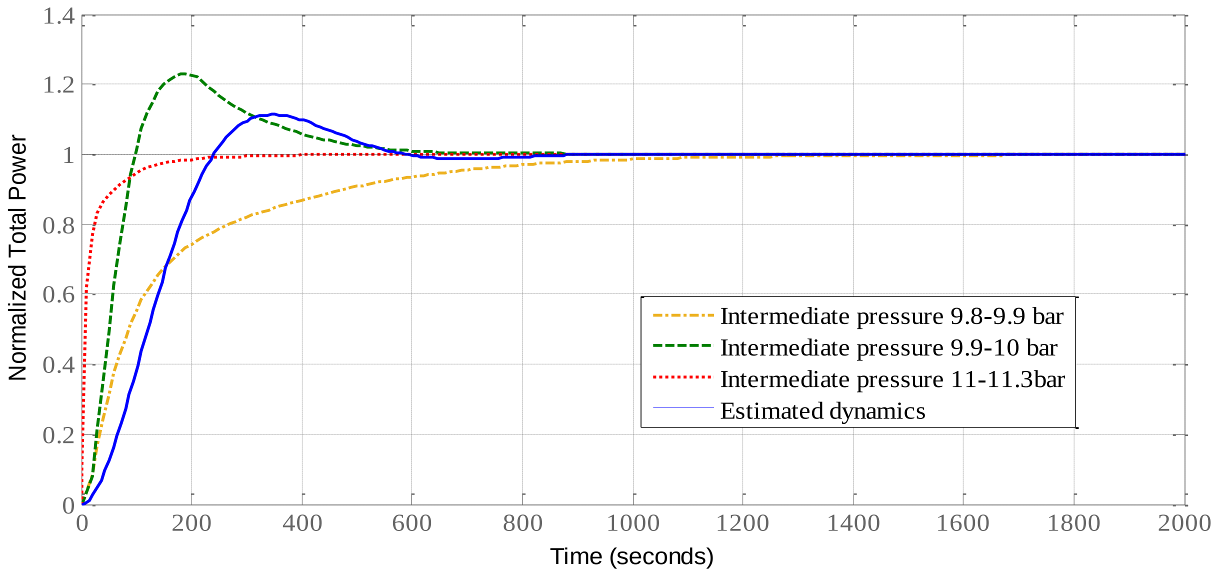


Figure 4.5. Normalized step responses for input dynamics estimation of FTC-VI two-stage ASHP water heater.

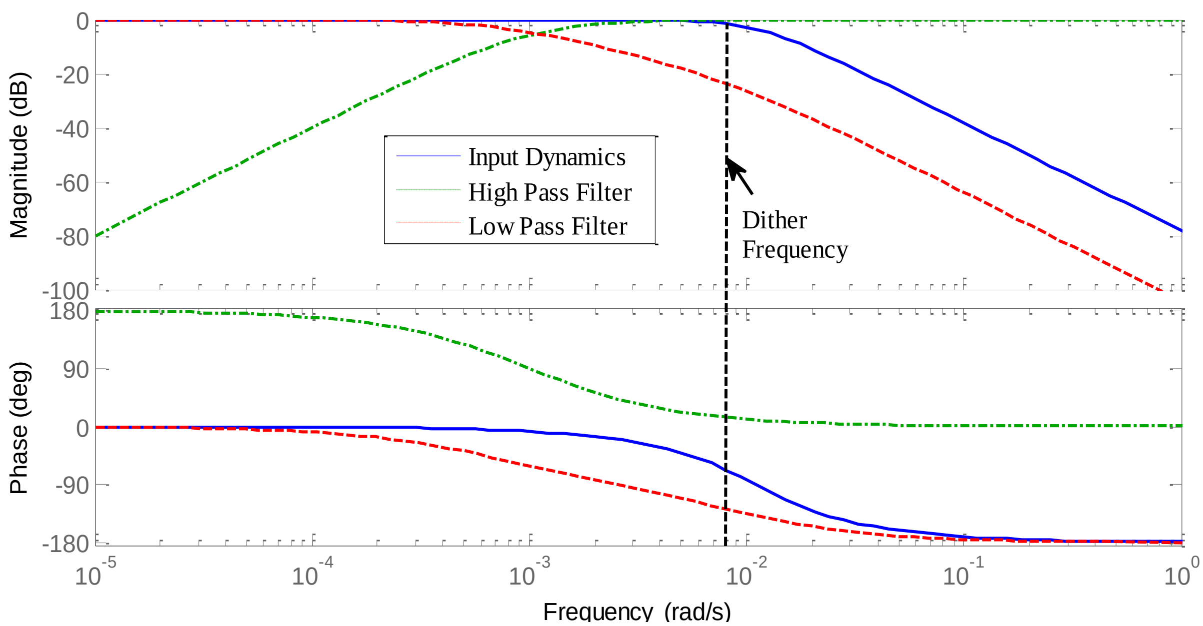


Figure 4.6. Bode plots for the estimated input dynamic, high-pass and low-pass filters.

As described in Chapter 2 for the Newton based ESC, the outer loop in Figure 2.2 needs to be designed and added. In this study, the demodulation signal for Hessian estimate is designed as:

$$N(t)=\frac{16}{4000^2}\left[\sin^2(0.0075t)-\frac{1}{2}\right] \tag{4-14}$$

The low-pass filter for the Hessian estimation is chosen as:

$$F_{LPH}(s)=\frac{0.0018^2}{s^2+2\times 0.87\times 0.0018s+0.0018^2} \tag{4-15}$$

Besides the ESC controller, several inner-loop controllers are implemented for regulating the key process variables. i) The intermediate pressure for the injection loop is regulated by the injection loop expansion valve opening with a PI controller. ii) The water outlet temperature setpoint is regulated by the compressor speed with another PI controller. The setpoint for the water outlet temperature is 55°C. iii) The main-loop superheat is regulated by the corresponding EEV opening with a PI controller, with the setpoint of 5°C. The specific design specifications of the three PI controllers are shown in Table 4.2.

Table 4.2. Design specifications of the PI controllers

| | Proportional Gain ($k$) | Integral Time ($T_i$) | Initial Output of PI Controller |
|---|---|---|---|
| Intermediate pressure PI | $1\text{x}10^{-12}$ | 1 | $7\text{x}10^{-7}$ |
| Superheat PI | $1\text{x}10^{-5}$ | 100 | $2.5\text{x}10^{-7}$ |
| Water outlet temperature PI | 1 | 5 | 50 |

### 4.3.2 Motivating case study for Newton ESC

Based on the static map and the estimated input dynamics above, the gradient ESC designed in the previous subsection is first implemented and applied to the FTC-VI two-stage ASHP water heater model under the same operating condition. With two initial values of intermediate pressure values. The ESC trajectories of the intermediate pressure are shown in Figure 4.7. The simulation starts at $t$ = 2 hours with the initial intermediate pressure of 11 bar and 9.4 bar, respectively, which correspond to the two sides of the optimum of 10.2 bar in the static map in Figure 4.4. For either case, the ESC can converge to the same intermediate pressure of 10.2 bar. Compared to the estimated optimum of 10.1 bar in the calibrated static map, the steady-state error is about 0.99%. However, the convergence time for the case starting from 9.4 bar is 2 hours as opposed to 4 hours for the case starting from 11 bar, in spite of the fact that their distances to the optimum are similar. This can be explained from the curvature in the static map, where the curve is steeper to the left of the calibrated optimum of 10.1 bar, and flatter to the right. Such consistency in convergence time is due to the different Hessian for this asymmetric map.

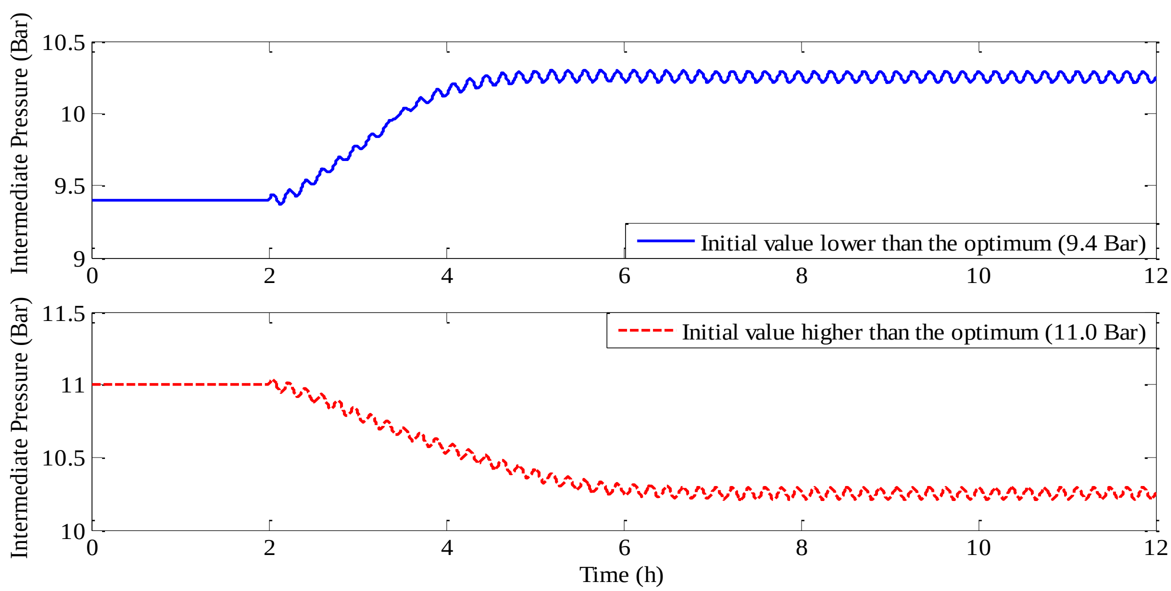


Figure 4.7. Trajectories of intermediate pressure of gradient ESC from different initial conditions.

Based on such observation, the Newton based ESC is considered a better solution to achieving more consistent transient performance. In the remaining simulations, the Newton based ESC is designed and implemented. As to be shown in Section 4.4, the Newton based ESC can achieve relatively consistent transient performance across different operating conditions.

## 4.4 Simulation Results

The Newton based ESC designed in the previous section is evaluated for three scenarios: 1) fixed ambient temperature, 2) a staircase profile of ambient temperature, and 3) a realistic profile of ambient temperature.

To quantify the transient performance for ESC simulation, the settling time is evaluated for the output (i.e. the total power in this study) rather than the manipulated input. For relative 'flat' static map of total power in terms of the manipulated variables, the 'improvement' of energy efficiency can be marginal even within a nontrivial neighborhood of the optimum of input.

### 4.4.1. ESC under fixed condition

The Newton based ESC is first evaluated for the two scenarios in Figure 4.4. The simulation results for the initial intermediate pressure of 9.8 bar are shown in Figure 4.8 and Figure 4.9. ESC starts at $t$ = 1 hour, with the initial liquid level and the UEV opening being 21% and $5.35 \times 10^{-1}$ $mm^2$, respectively. After about 3000 seconds, ESC converges the intermediate pressure to 10.2 bar, which corresponds to the flash-tank liquid level of 43.2% and UEV opening of $6.77 \times 10^{-1}$ $mm^2$.

The total power drops from 4875.08 W to 4793.34 W after about 1600 seconds, and the COP increases from 2.14 to 2.18. In addition, the injection ratio increase from 34.3% to 38.4%. The condenser water outlet temperature is well kept at the setpoint of 55°C. Compared to the estimated optimum in the calibrated static map, the steady-state errors of ESC results are about 0.99% and 1.1% for the intermediate pressure and liquid level, respectively. Figure 4.10 shows the trajectories of the main-loop superheat and the main-loop LEV opening, which justifies a sound regulation. Also, the ESC gradient estimate (i.e. the output of the low-pass filter) is shown, which converges to the neighborhood of zero, i.e. achieving the optimality.

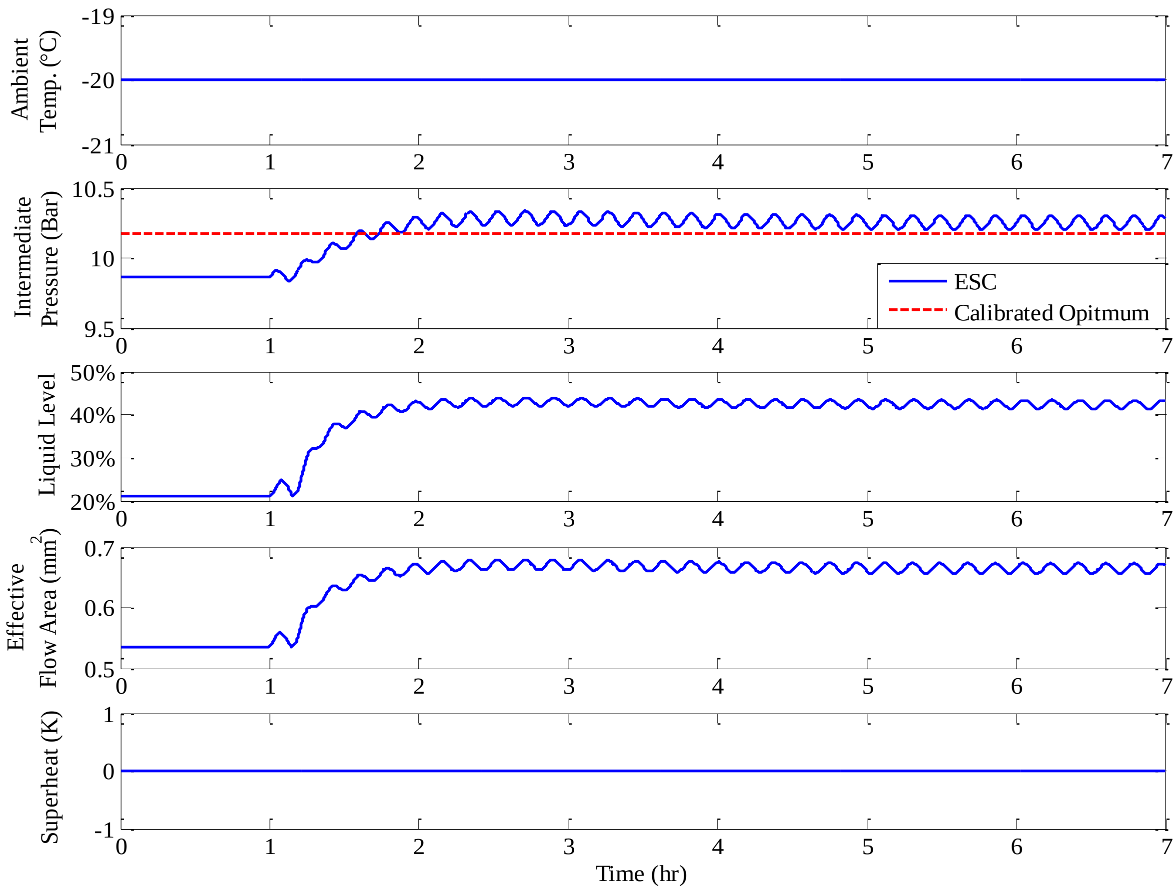


Figure 4.8. Trajectories of intermediate pressure, liquid level, UEV opening and superheat for ESC simulation under fixed ambient temperature with initial intermediate pressure of 9.8 bar.

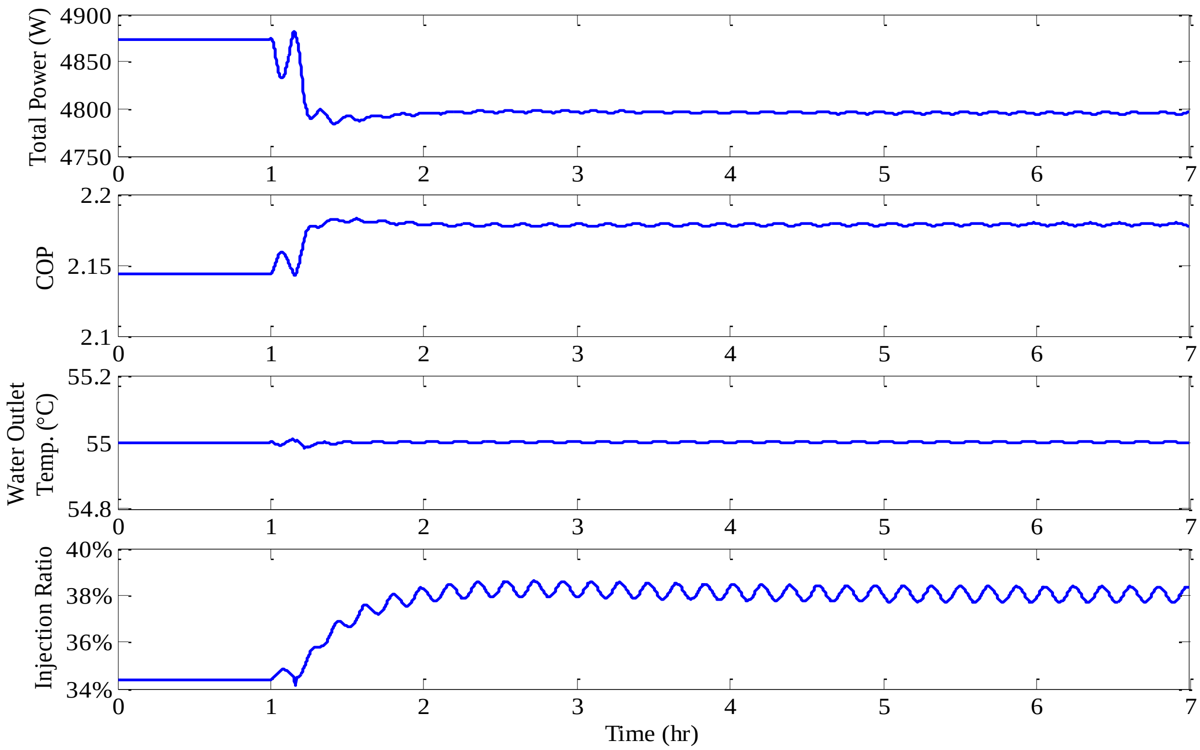


Figure 4.9. Trajectories of total power, COP, water outlet temperature and injection ratio for ESC simulation under fixed ambient temperature with initial intermediate pressure of 9.8 bar.

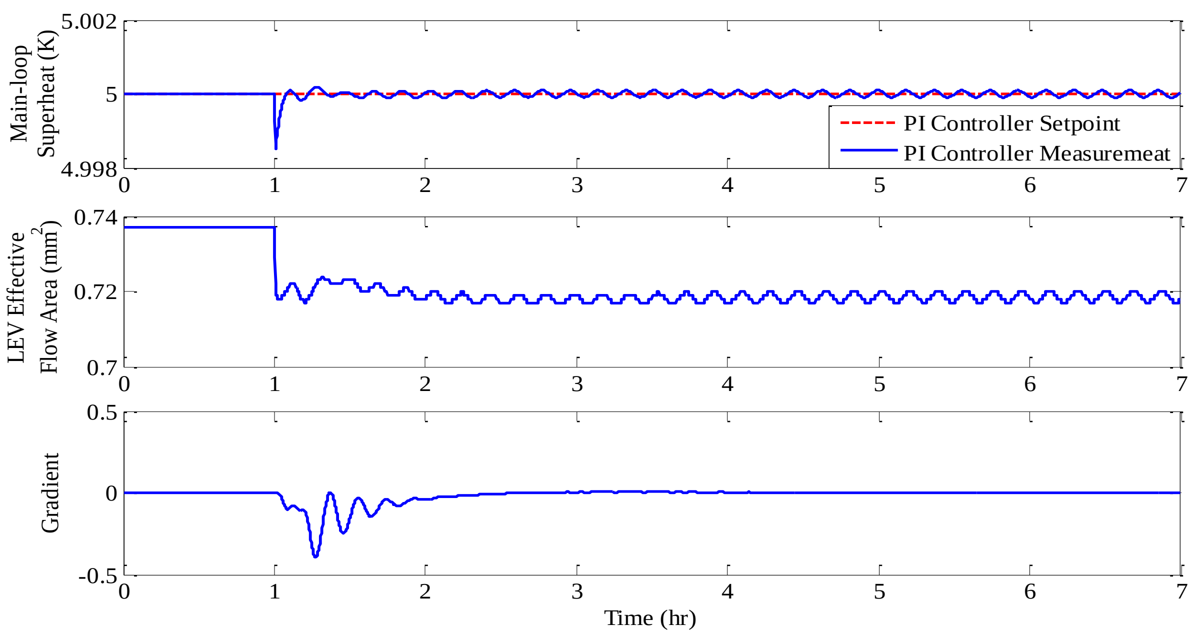


Figure 4.10. Trajectories of main-loop superheat, LEV opening, and estimated gradient for ESC simulation under fixed ambient temperature with initial intermediate pressure of 9.8 bar.

Then the simulation is run with the initial intermediate pressure of 11 bar, resulting in the liquid level and UEV opening of 52% and $7.76 \times 10^{-1}$ mm$^2$, respectively. As shown in Figure 4.11, after about 3000 seconds, the total power and COP settle at their respective optimal values. The reason for the settling time being longer than that of the previous case is that the initial value is farther from the optimal value.

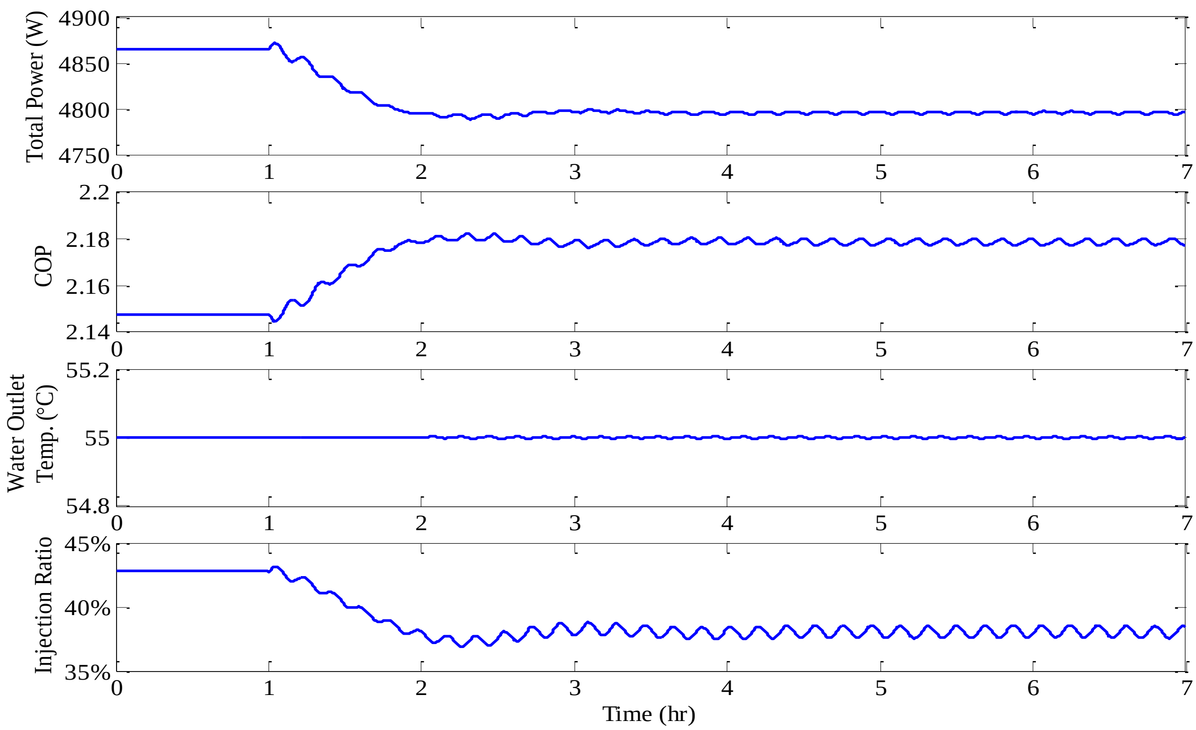


Figure 4.11. Trajectories of total power, COP, water outlet temperature and injection ratio for ESC simulation under fixed ambient temperature with the initial intermediate pressure of 11 bar.

Figure 4.12 shows that the intermediate pressure settles at 10.25 bar, with the corresponding liquid level and UEV opening being 42.5% and $6.67 \times 10^{-1}$ mm$^2$, respectively, which are almost the same as the values found in the above case. The total power drops from 4864.9 to 4794.3 Watt, and the COP increases from 2.14 to 2.18. The condenser water outlet temperature remains nearly constant throughout the simulated period. The injection ratio decreases from 42.8% to 37.5%.

Compared to the estimated optimum in the calibrated static map, the steady-state error is about 1.1% and 1.3% for the intermediate pressure and liquid level, respectively. Figure 4.13 shows the trajectories of the main-loop superheat and the main-loop LEV opening, as well as the estimated gradient. The results show that the main-loop superheat is also well controlled and the gradient converges to the neighborhood of zero.

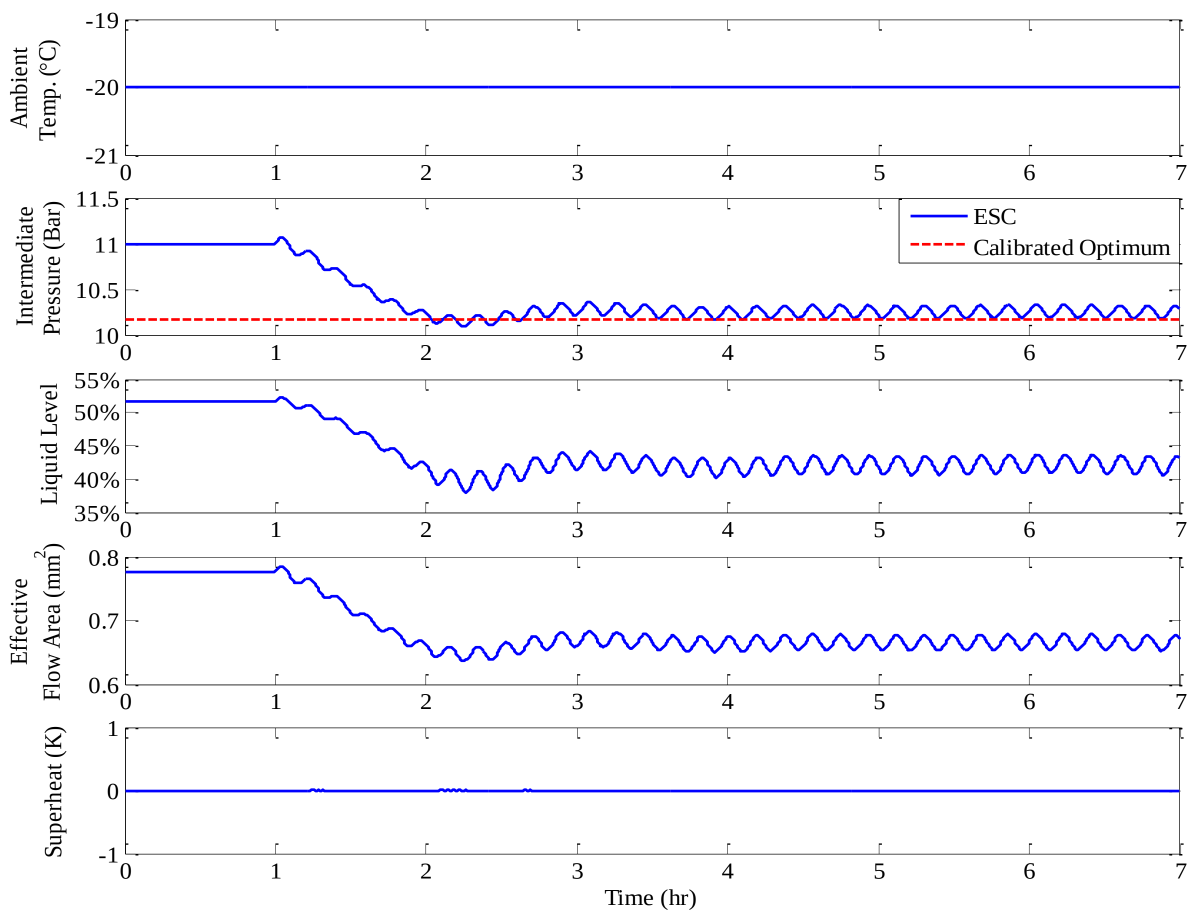


Figure 4.12. Trajectories of intermediate pressure, liquid level, UEV opening and superheat for ESC simulation under fixed ambient temperature with the initial intermediate pressure of 11 bar.

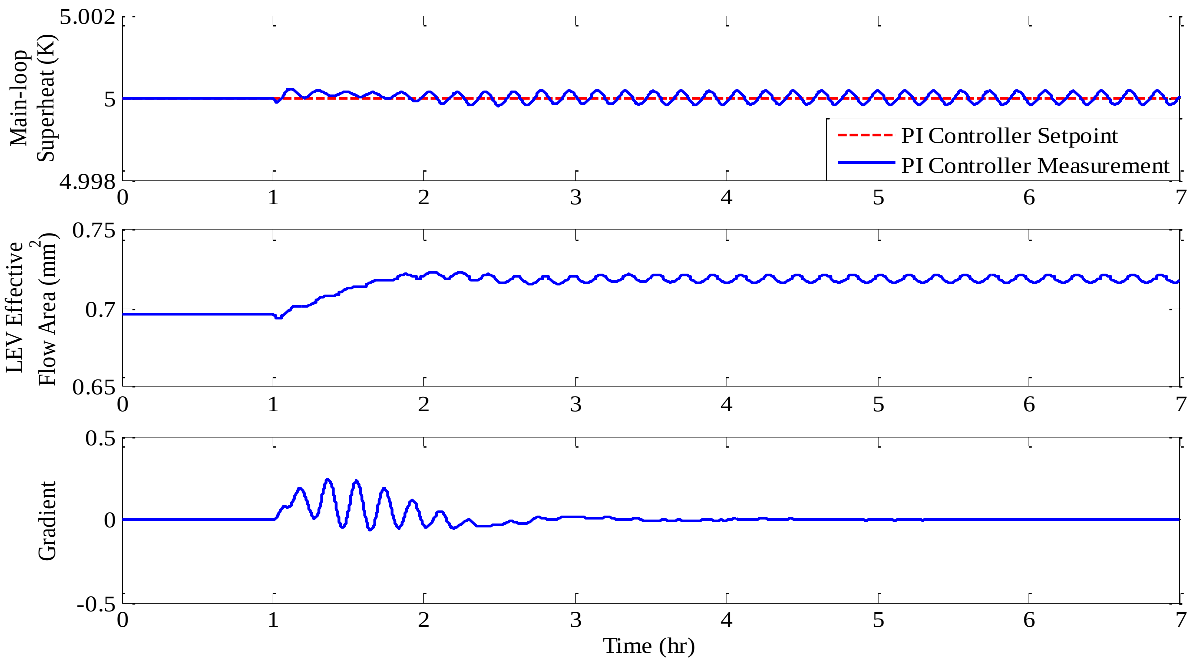


Figure 4.13. Trajectories of main-loop superheat, LEV opening, ESC Gradient for ESC simulation under fixed ambient temperature with the initial intermediate pressure of 11 bar.

Figure 4.14 shows the Hessian estimation for the fixed ambient condition. The upper plot shows the trajectories of the estimated Hessian without closing the loop of ESC, at the fixed intermediate pressure of 9.8 bar and 11 bar. The initial value of Hessian is set as 1, when Hessian estimation is turned on at 1 hour, it quickly finds the accurate Hessian value local near the intermediate pressure of system operation. The blue solid line is the result for 9.8 bar, and the red dash line is the result for 11 bar. It can be seen the Hessian at 9.8 bar is much larger than that at 11 bar, which is very consistent with the curvature shown in the static map of Figure 4.4, where the left side (9.8 bar) of the optimum is much steeper than that of the right side (11 bar). The lower plot shows the results of Hessian estimation with the ESC turned on. The initial Hessian value is also set as 1, the ESC and Hessian estimation are both turned on at 1 hour. The blue solid line stands for the ESC starting from 9.8 bar, and the red dash line stands for the ESC starting from 11 bar. For the transient trajectories of Hessian estimate, the Hessian estimate at the initial stage is significantly larger for the searching process started at 9.8 bar. In addition, it reveals that the Hessian estimate eventually converges to the same value for ESC starting from both sides of the optimum. This illustrates how the Newton-based ESC can achieve consistent convergence for an asymmetric map through Hessian estimate.

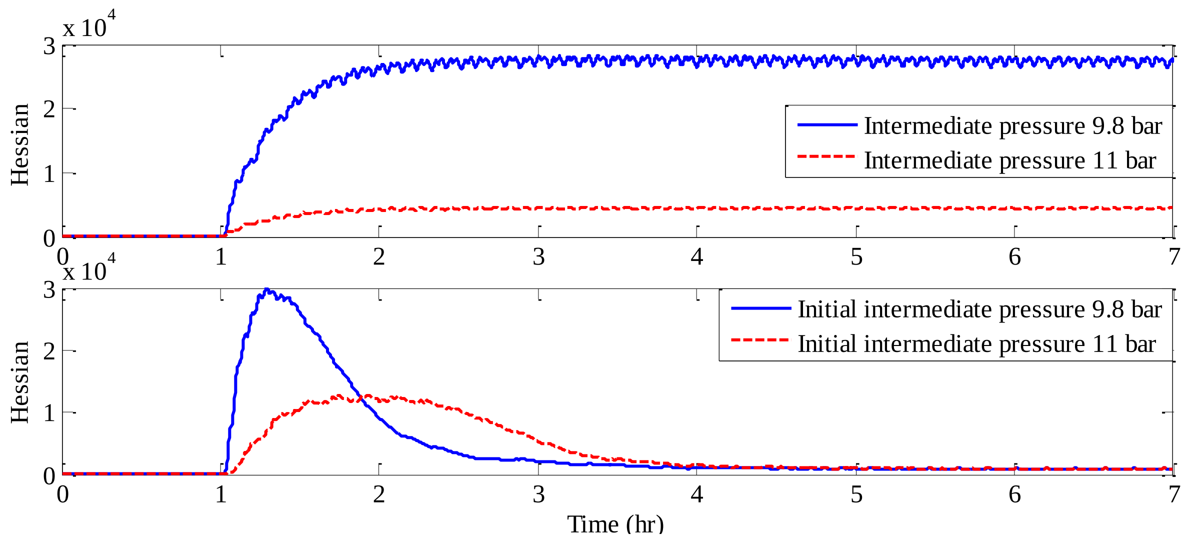


Figure 4.14. Trajectories of Hessian estimation for system operation under fixed ambient temperature before vs after closing ESC loop: initial intermediate pressure of 9.8 bar and 11bar.

The simulation results show that ESC can converge the operation very close to the calibrated optimum regardless the initial intermediate pressure with similar convergence characteristic. For both cases, the liquid levels in the flash tank are nearly the same (43.2% and 42.5%). References [89, 90] indicate that the liquid refrigerant in the flash tank should maintain a level of 30% to 60% of the tank height to ensure the reliable system operation. Therefore, the liquid levels searched by ESC are reasonable and safe. In addition, the intermediate pressure setpoint can be effectively optimized via EEV adjustment by minimizing the total power consumption without violating the load demand. It is noteworthy that the superheat has been kept zero throughout the simulation period in both cases, which indicates that the control method that we have proposed can maintain the liquid level and optimize the efficiency of FTC heat pump system without the need for adjusting the superheat.

### 4.4.2. ESC under variable ambient condition

The ESC is then tested under a staircase profile of ambient temperature. As shown in Figure 4.15, the ambient temperature starts from −21°C, first going up to −20°C, −19°C with 1°C increment, and then returning to −22°C and −25°C with a 3°C increment. Each step is realized with a 100-sec ramp. The initial intermediate pressure is set as 10.5 bar, and the ESC starts at $t$ = 1 hour. The ESC is shown to converge to the steady-state values of 9.97, 10.24, 10.52, 9.66 and 8.94 bar sequentially under the different ambient temperature. To evaluate the steady-state performance of ESC, the true optimum for each operating condition is found with the Sequential Quadratic Programming (SQP) procedure in the Dymola Optimization Library [180, 181]. The SQP approach can solve a general nonlinear constrained optimization problem with super-linear convergence. The tolerance of SQP optimization is set as $1 \times 10^{-3}$ through all the simulations. The optimum intermediate pressure found by SQP is shown in Figure 4.15 as dashed lines. The results show that the optimum values found by ESC are quite close to those found by SQP. The maximal error between the ESC and SQP is 1.1% at −25°C, where the optimal value found by ESC is 8.94 bar as opposed to the 8.84 bar by SQP. Meanwhile, the liquid level is stabilized around at 41.8% with only small variations through the whole simulation. In consequence, the superheat is always kept at 0°C, ensure that the saturated refrigerant vapor is always injected into the compressor.

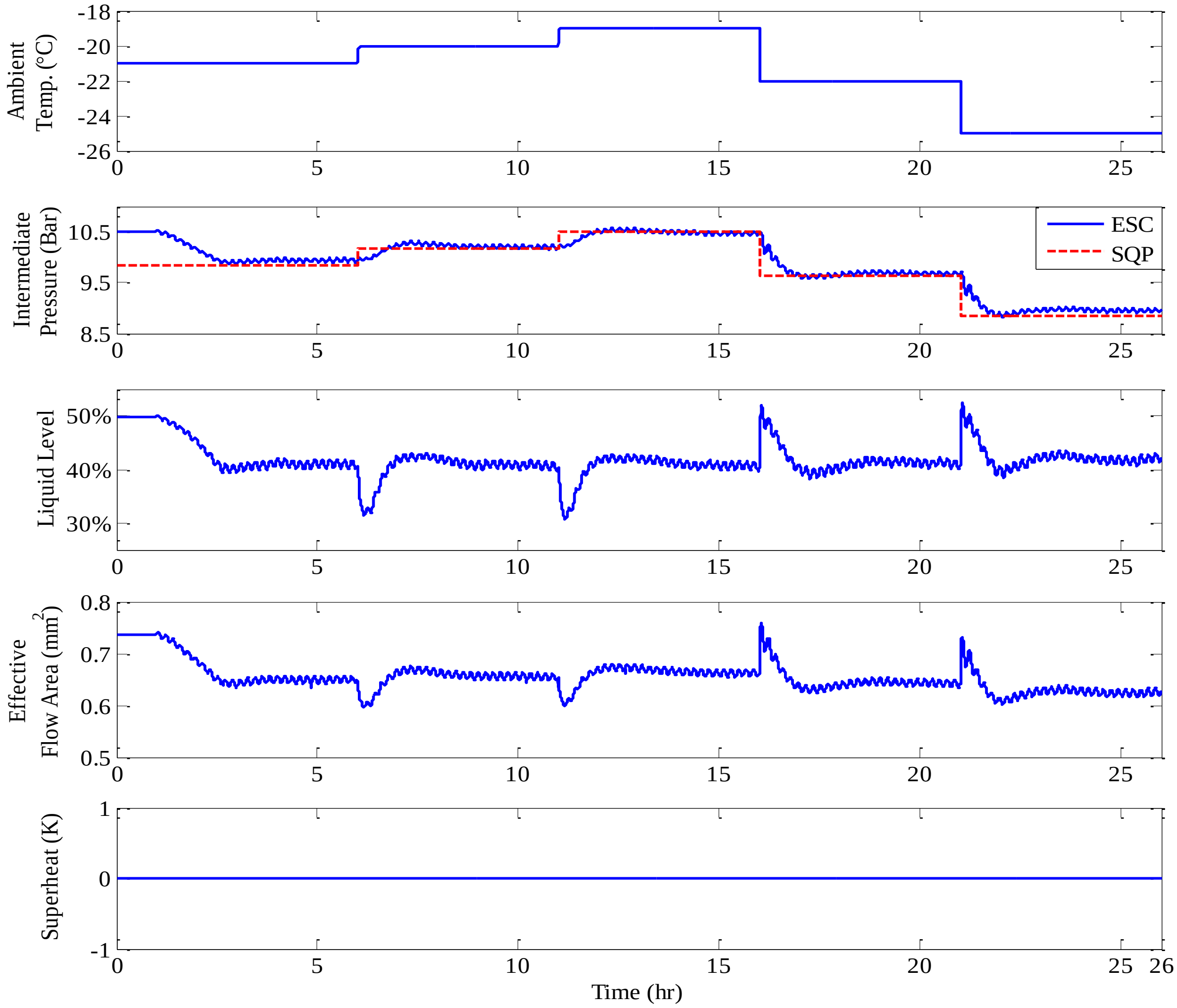


Figure 4.15. Trajectories of intermediate pressure, liquid level, UEV opening and superheat for ESC simulation under stair-case ambient temperature changes.

Figure 4.16 shows the trajectories of total power, COP, water outlet temperature, and the injection ratio. The vapor injection ratio is 38.5%, 37.9%, 37.3%, 38.8% and 39.8% for the five scenarios. The total power converged to the respective optimum values at 4851.9, 4793.3, 4739.3, 4908.3 and 5091.9 Watt, respectively, and the COP converges to the respective optimum of 2.15, 2.18, 2.20, 2.13 and 2.05. Meanwhile, the condenser water outlet temperature is well regulated throughout the whole simulation period. The results show that the ESC can converge to the true optimum under different ambient temperature and different steps of change in the ambient temperature.

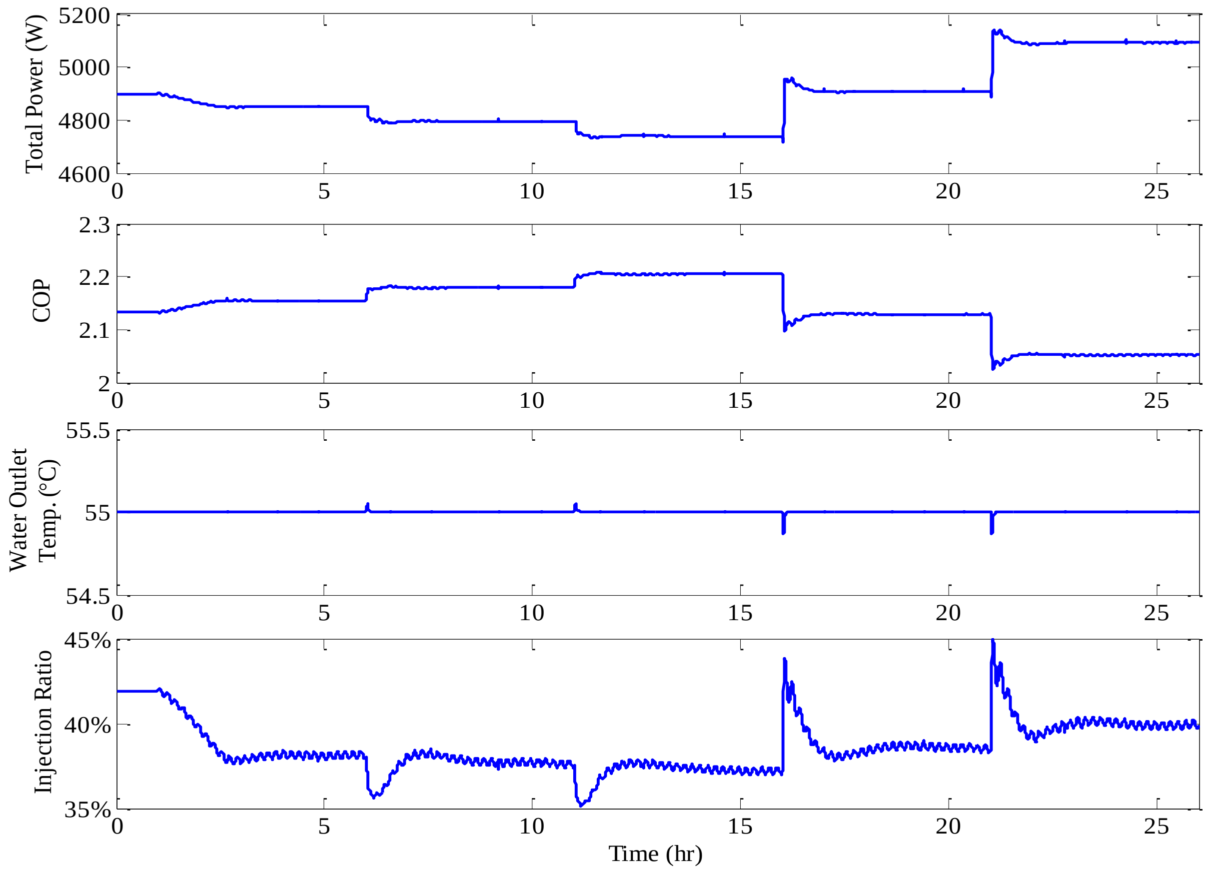


Figure 4.16. Trajectories of total power, COP, water outlet temperature and injection ratio for ESC simulation under a stair-case ambient temperature profile.

It is noteworthy that some process variables, such as the liquid level, effective flow area and injection ratio, demonstrate significant fluctuation during the transients when the ambient temperature changes. The primary reason for such observation is due to a current limitation for the solvers of dynamic simulation in Dymola when discontinuities are present, which is very likely true for other simulation platforms as well. A typical discontinuity is step change, while the ramp change presents a piecewise linear function with discontinuous derivatives at the junction points.

Such discontinuities may induce large numerical transients which are different from the actual behavior of the physical systems. Although replacement of a step change by a ramp change can lead to better results, there remains such numerical transient more or less depending how steep the ramp change is. In addition, the manipulated input of ESC is the intermediate pressure, while the ultimate physical actuation is realized by the UEV opening. As consequence, the response of injection ratio and injection ratio change more drastically as same as the expansion valve effective flow area. Similar to the case of fixed ambient temperature, the trajectories of the main-loop superheat and the LEV opening are plotted in Figure 4.17, which indicates a quality inner-loop control. Also shown in Figure 4.17 is the ESC gradient trajectory. For each ambient temperature, the ESC gradient converges to zero respectively.

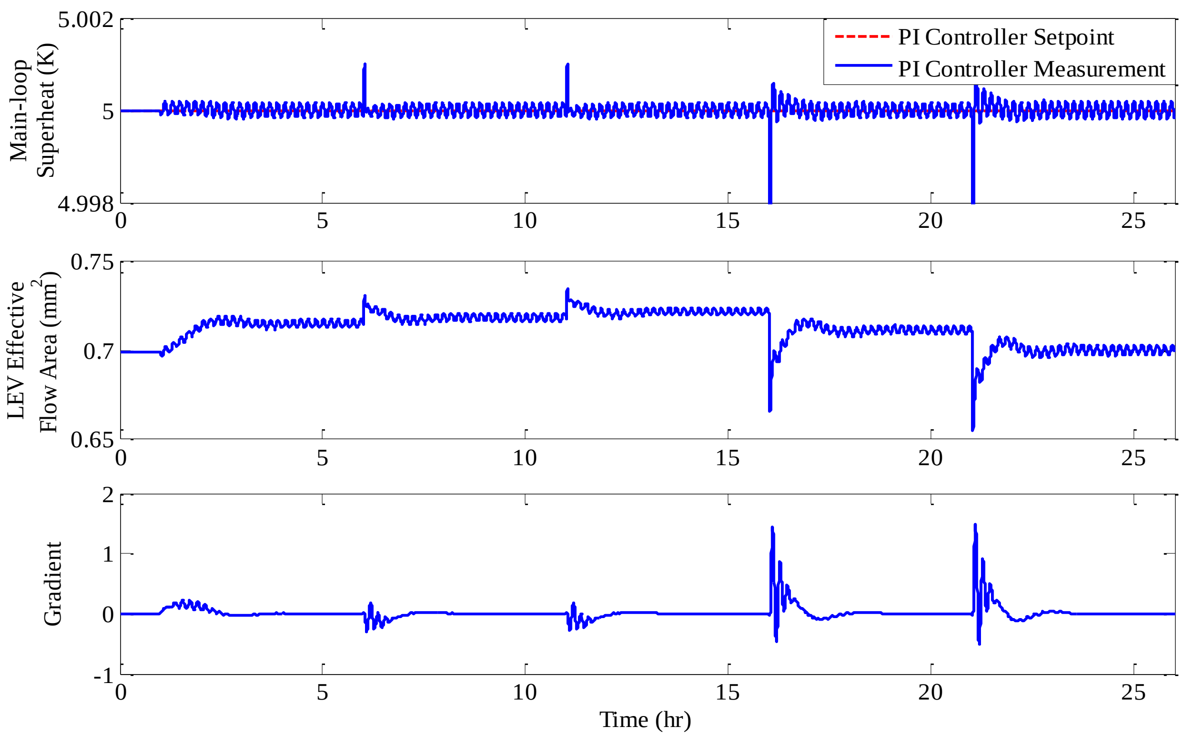


Figure 4.17. Trajectories of main-loop superheat, LEV opening, ESC Gradient for ESC simulation under stair-case ambient temperature changes.

### 4.4.3. ESC under a realistic ambient temperature profile

The ESC strategy is then evaluated with a 96-hour (January 1st through 4th) realistic ambient temperature profile of Fairbanks, Alaska from the TMY3 data. Figure 4.18 shows simulation trajectories for the intermediate pressure, liquid level, UEV opening and the superheat.

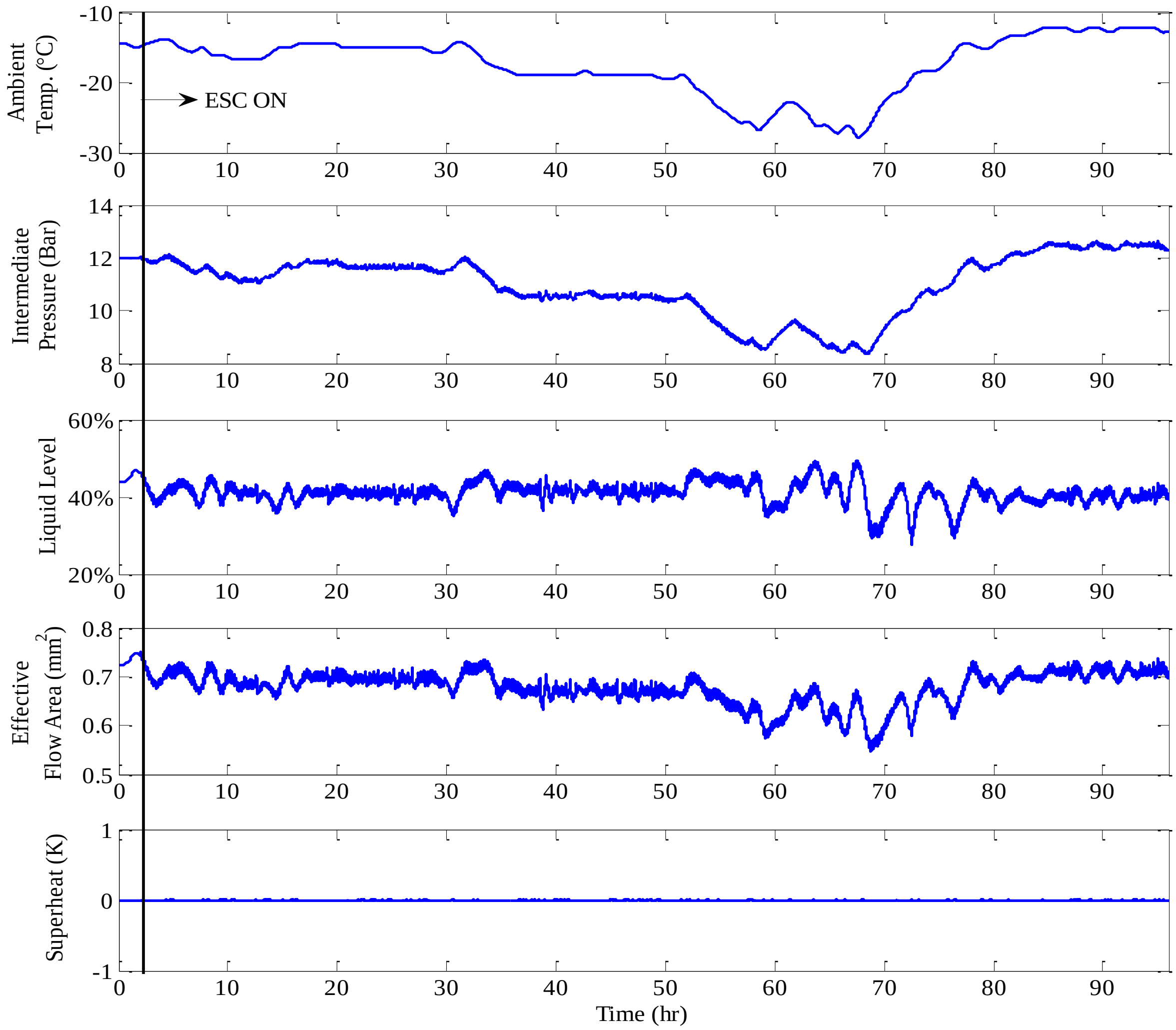


Figure 4.18. Trajectories of intermediate pressure, liquid level, UEV opening and superheat for ESC simulation under realistic ambient temperature profile.

In particular, the intermediate pressure profile found by ESC is compared with that those found by SQP in Figure 4.19. The SQP optimum values are found for each ambient temperature from -

12°C to -28°C, with increment of 0.1°C. The ESC is turned on at $t$ = 2 hour with the initial intermediate pressure at 12 bar. After about 3670 seconds, ESC drives the intermediate pressure to about 11.77 bar, which coincides with the value found by SQP. The two trajectories are very close to each other, with the maximal gap of 0.14 bar (about 1.7%) at –27°C. The delay between the ESC and SQP is estimated by the cross-correlation function as 410 seconds, this time delay is acceptable for an ASHP operating in a realistic ambient condition.

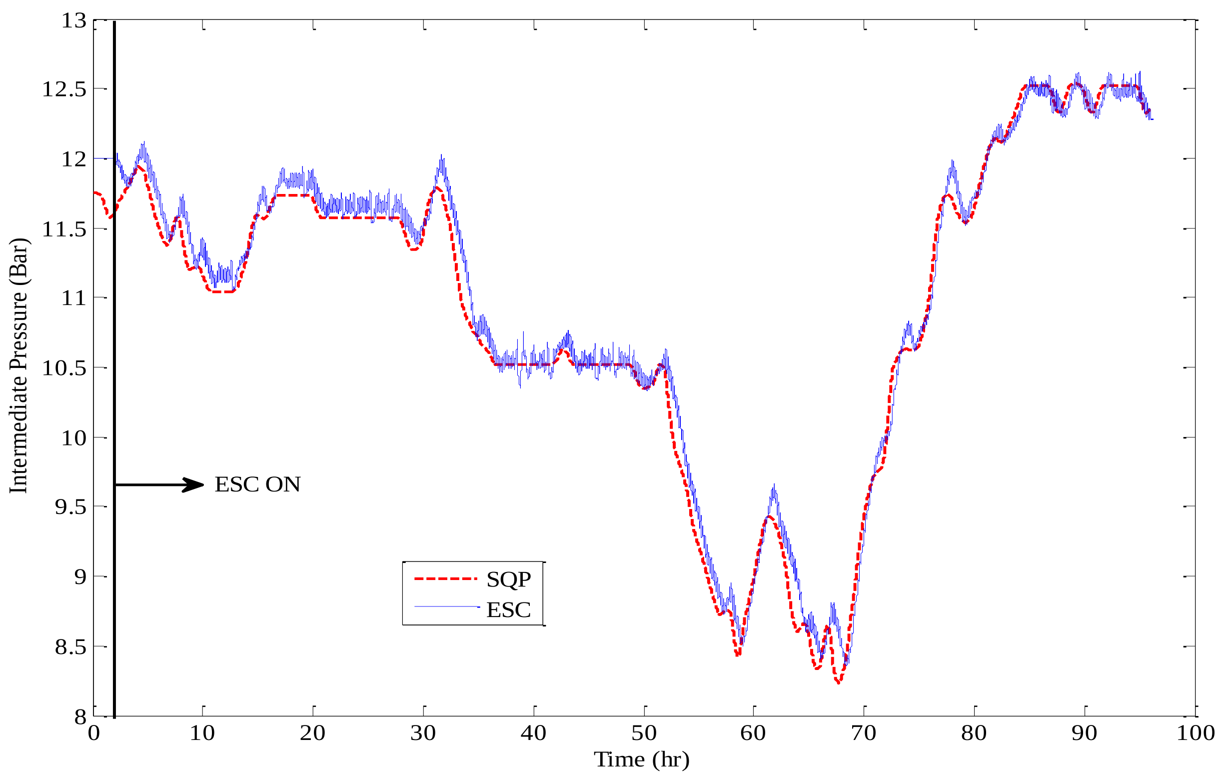


Figure 4.19. Comparison of intermediate pressure trajectories obtained by ESC and SQP.

Based on the intermediate pressure trajectory found by ESC in real time, the liquid level in the flash tank has been kept at a reasonable level. As consequence, the superheat is almost zero throughout the whole simulation, ensuring that the saturated vapor can be injected into the vapor injection compressor in a safe way, thus there would be no concern for the liquid refrigerant to flush into the compressor or extremely low liquid level that would deteriorate the system performance. The profiles of total power, COP, water outlet temperature and injection ratio are shown in Figure 4.20. The injection ratio presents a maximum value when the ambient temperature is at the lowest positon for the whole simulation. The condenser water outlet temperature is regulated well at 55°C throughout the whole simulation period.

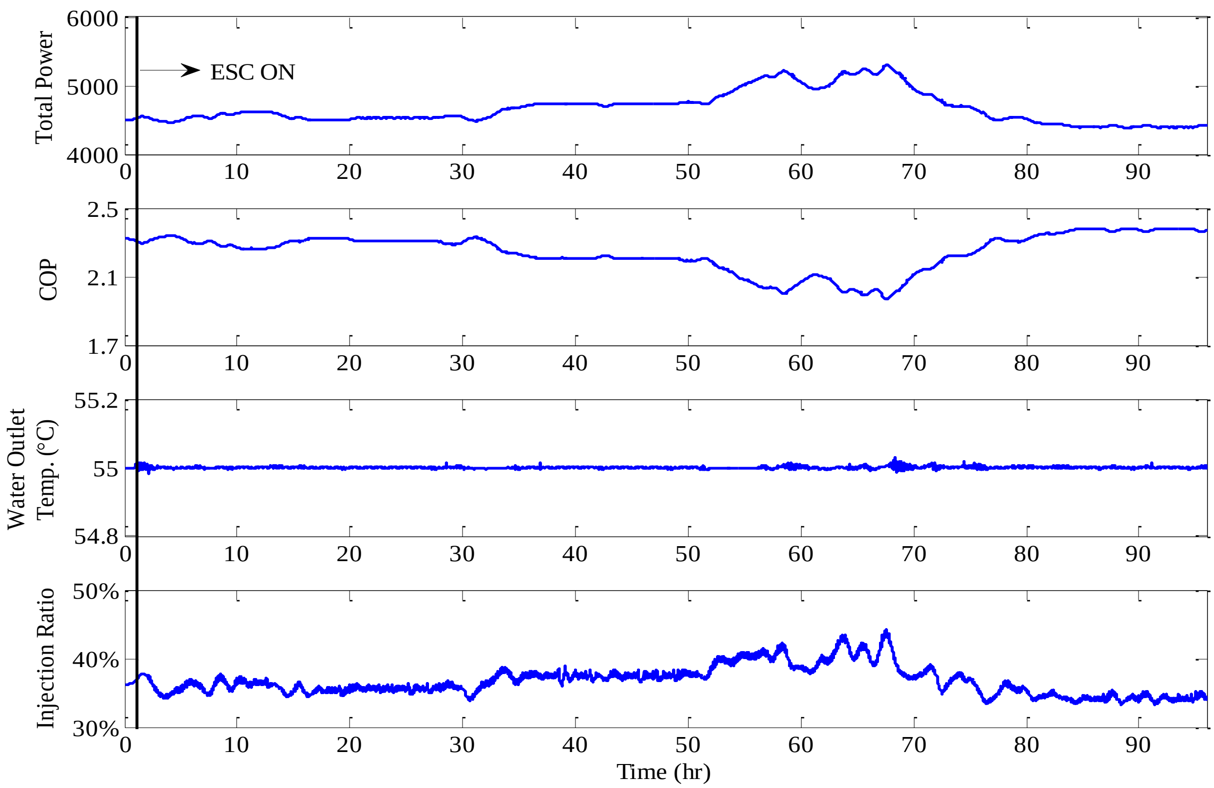


Figure 4.20. Trajectories of total power, COP, water outlet temperature and injection ratio for ESC simulation under realistic ambient temperature profile.

Figure 4.21 shows the main-loop superheat, the main-loop EEV opening and the gradient estimation through the whole simulation period. It can be seen the superheat is well maintained in the whole simulation. In addition, the gradient is shown to converge to zero when the ambient temperature is nearly constant. The total-power trajectories of ESC and SQP are compared in

Figure 4.22, where the ESC results follow the SQP optimum quite well. The maximum difference between ESC and SQP is just 41.2W under the temperature of –27.8°C, where the total power for ESC is 5312.5 Watt as opposed to 5271.3 Watt by SQP.

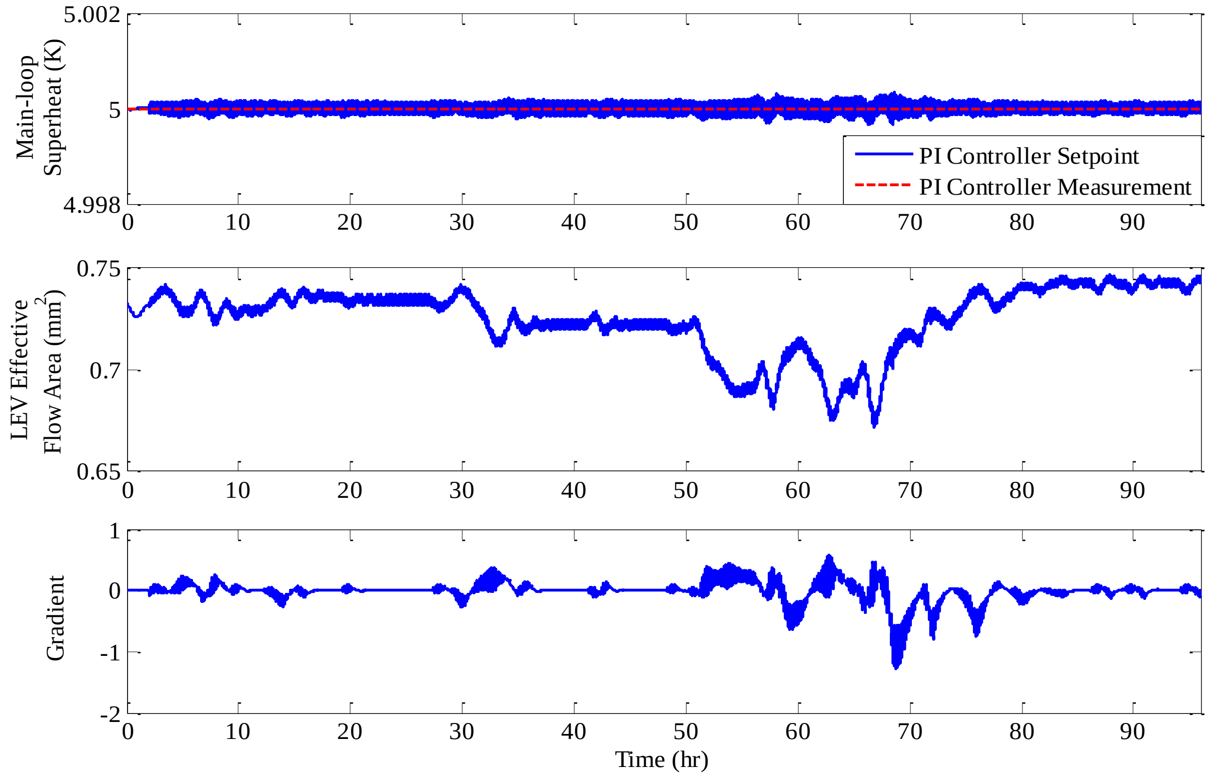


Figure 4.21. Trajectories of intermediate pressure, liquid level, UEV opening and superheat for ESC simulation under realistic ambient temperature profile.

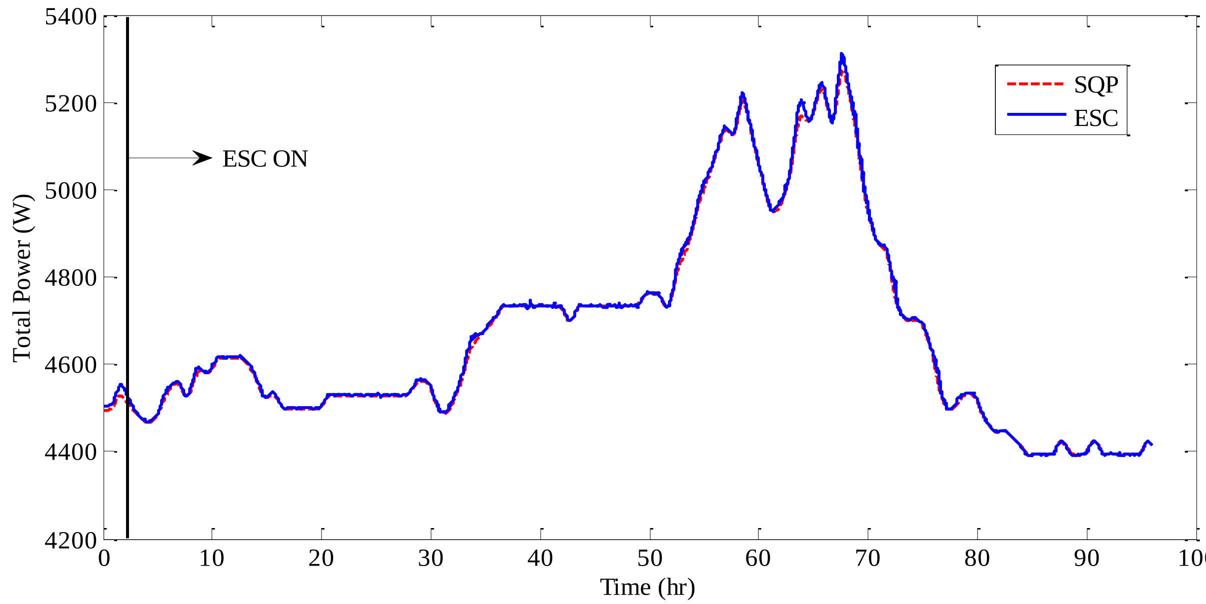


Figure 4.22. Comparison of total power trajectories obtained by ESC and SQP.

These results show that the proposed ESC strategy promises a successful solution to provide a cost-effective model-free optimal control method for the FTC-VI cycle which has long been considered difficult for heat pump development. By virtue of the ESC strategy that optimizes the intermediate pressure setpoint, two significant benefits can be obtained. First, to the authors' best knowledge, a novel and systematic control strategy is proposed for the first time on how to control the UEV for the injection loop without elevating the superheat, such that a proper and safe liquid level can be obtained inside the flash tank. Second, the optimum system performance can be obtained so that the full potential for the FTC-VI two-stage ASHP system can be realized.

### 4.5 Summary

In this chapter, a novel control strategy for the flash-tank cycle vapor injection based two-stage air-source heat pump system is proposed. Controlling the intermediate pressure setpoint by the upper expansion valve eliminates the need for adjusting the superheat for the injection loop. In other words, the injected medium remains saturated vapor, which retains the inherent merit of the flash-tank cycle concept. Then, by imposing an extremum seeking control loop for tuning the intermediate pressure setpoint based on the feedback of total power, the total power consumption of the system can be minimized in real time in a model-free fashion. Optimization of the system efficiency is realized by the actuation of the upper expansion valve, however, without elevating the degree of superheat. Under fixed, staircase and realistic ambient temperature profiles, simulation results have validated the effectiveness of the proposed method. In addition to converging the operating points to the calibrated optimum, the superheat of the injection line the vapor injection line superheat is shown to be maintained at zero, while the liquid level of the flash tank is kept in a reasonable range for safe operation. These results indicate that the proposed control strategy can greatly facilitate the operation of flash-tank-cycle vapor injection based heat pump systems, and thus promote the ramification of such technology.

# CHAPTER 5

# DYNAMIC SIMULATION MODELING AND REAL-TIME OPTIMIZATION OF A CASCADE ASHP WATER HEATER VIA MULTIVARIABLE ESC

This chapter presents the dynamic simulation modeling and the real-time efficiency optimization strategy for a cascade ASHP water heater based on the multivariable extremum seeking control.

## 5.1 Introduction and Research Motivation

As introduced in Chapter 1, determination of the optimal intermediate temperature for a specific CASHP can be performed for only a limited number of operation conditions. For a practical CASHP system operated in realistic ambient and load conditions throughout its life cycle, the effectiveness of such optimization strategies can be rather limited. Cost-effective and practically feasible real-time control strategies for CASHP systems are of keen need.

In this chapter, the multivariable ESC strategy is applied to optimize the energy efficiency of CASHP operation as a model-free real-time optimization method, with two scenarios considered: i) power minimization feedback for fixed heating capacity operation, and ii) COP maximization feedback for variable heating capacity operation. For the first scenario considered in this study, the feedback for ESC design is the total power of the CASHP system, while the manipulated inputs are the intermediate temperature, HTC and LTC superheat. For the second scenario of variable heating capacity, the feedback is the system COP, with the manipulated inputs of HTC, LTC compressor frequency and the evaporator fan air mass flow rate. Pursuit of such operation is desirable for CASHP systems equipped with water tanks, as the optimum operation settings for power minimization and COP maximization may differ. The merits of ESC with total power feedback control are straightforward reduction of power consumption, and ease of implementation with only the power measurement involved. Such strategy does not guarantee to operate the system with the highest achievable efficiency, while ESC with the COP feedback can. Indeed, the COP feedback requires more measurements. West [150] proposes to use the COP feedback for optimizing an air condition system considering that the COP provides an absolute, realistic and continuous assessment of operational efficiency; meanwhile, he indicated that field measurement of COP is rather difficult. Tahersima et al. [151] propose an economic model predictive controller for a heat pump to maximize the system COP. As the COP feedback involves multiplications and division of several thermo-fluid variables, the inherent noise in measurements (e.g. flow rate) gets further amplified in the resultant COP signal. The use of COP feedback can affect the stability and performance of the closed-loop control system, and proper filtering is typically needed. For ESC, such filtering implies non-trivial output dynamics, which implies somewhat impact on the associated design and implementation.

## 5.2 Dynamic Modeling of the Cascade Heat Pump Water Heater

A Modelica based dynamic simulation model is developed for a CASHP water heater, using Dymola 2019 [13] and TIL Library 3.5.1 [14, 15]. Two scroll compressors are used in both the LTC and HTC. A fin-and-tube heat exchanger is used as the evaporator, two plate heat exchangers are used as the CHE and the condenser. EEVs are used in both the LTC and HTC. R404A and R245fa are used as the working fluid in the LTC and HTC, respectively, with 17 kg and 19 kg charges, respectively. Table 5.1 gives the specifications for the major design parameters of the main components.

Table 5.1. Design specifications of major components of the CASHP model.

| Components | Design specifications |
|---|---|
| Compressors | Scroll compressor; displacement: 29.1 $m^3 \cdot h^{-1}$ for LTC and 33.2 $m^3 \cdot h^{-1}$ for HTC; variable speed. |
| Condenser | Brazed plate heat exchanger; single plate heat transfer area 0.095 m2; number of plates: 132. |
| CHE | Brazed plate heat exchanger; single plate heat transfer area 0.095 $m^2$; number of plates: 56. |
| Evaporator | Fin-and-tube heat exchanger; staggered copper tubes; tube diameter 9.52mm; wall thickness: 0.35 mm; number of serial tubes 3; number of parallel tubes 36; fin spacing 2.2 mm; thickness 0.2 mm; number of parallel tube side flows 18; tube length 1.8 m. Number of evaporator: 2. |
| Evaporator fan | Nominal air volume flow rate: 30000 $m^3 \cdot h^{-1}$. |
| Water pump | Nominal water mass flow rate: 2.8 kg·s-1. |
| Expansion valve | Maximal effective flow area: $1.2\times10^{-6}$ $m^2$; number: 2. |

The total power consumption is comprised of those for the two compressors and the evaporator fan and the water pump, i.e.

$$P_{total} = P_{comp,HTC} + P_{comp,LTC} + P_{fan} + P_{pump} \tag{5-1}$$

where $P$ refers to the power consumption, subscripts '*total*', '*comp,HTC*', '*comp,LTC*' refer the total power consumption, the compressor of HTC and compressor in LTC, respectively. Subscripts '*fan*' and '*pump*' refer to the evaporator fan and condenser water pump, respectively.

According to Figure 1.7, the heating capacity is the heat flux rejected to the water via the condenser, i.e.

$$\dot{Q} = \dot{m}_{ref}(h_6 - h_7) = \dot{m}_{water} c_p (T_{wo} - T_{wi}) \tag{5-2}$$

where $\dot{m}$ refers to the mass flow rate, subscripts '*water*' and '*ref*' refer to the condenser water and refrigerant, respectively. $T$ refers to temperature, and subscripts '*wo*' and '*wi*' refer to the water outlet and water inlet of the condenser, respectively. $h$ refers to the enthalpy, subscripts '6' and '7' refer the refrigerant inlet and refrigerant outlet of the condenser, respectively. $c_p$ refers to the water specific heat capacity. Then the COP of the CASHP is calculated by

$$COP = \frac{\dot{Q}}{P_{total}} \tag{5-3}$$

The schematic diagram of the CASHP system is shown in Figure 5.1 for power minimization under fixing heating capacity. Figure 5.2 shows that for COP maximization under variable heating capacity. For the power minimization case, the speed of the HTC condenser water pump is fixed, and the water outlet temperature setpoint is regulated by the HTC compressor speed. The ESC based CASHP control designed for such operation has its manipulated inputs of the intermediate temperature, the HTC and LTC superheat setpoints, while the total power is the only feedback. The LTC compressor speed is used to regulate the setpoint of intermediate temperature. The superheat setpoints of the HTC and LTC are regulated by the respective expansion valve openings. As a simplified treatment, the LTC evaporator fan speed is fixed.

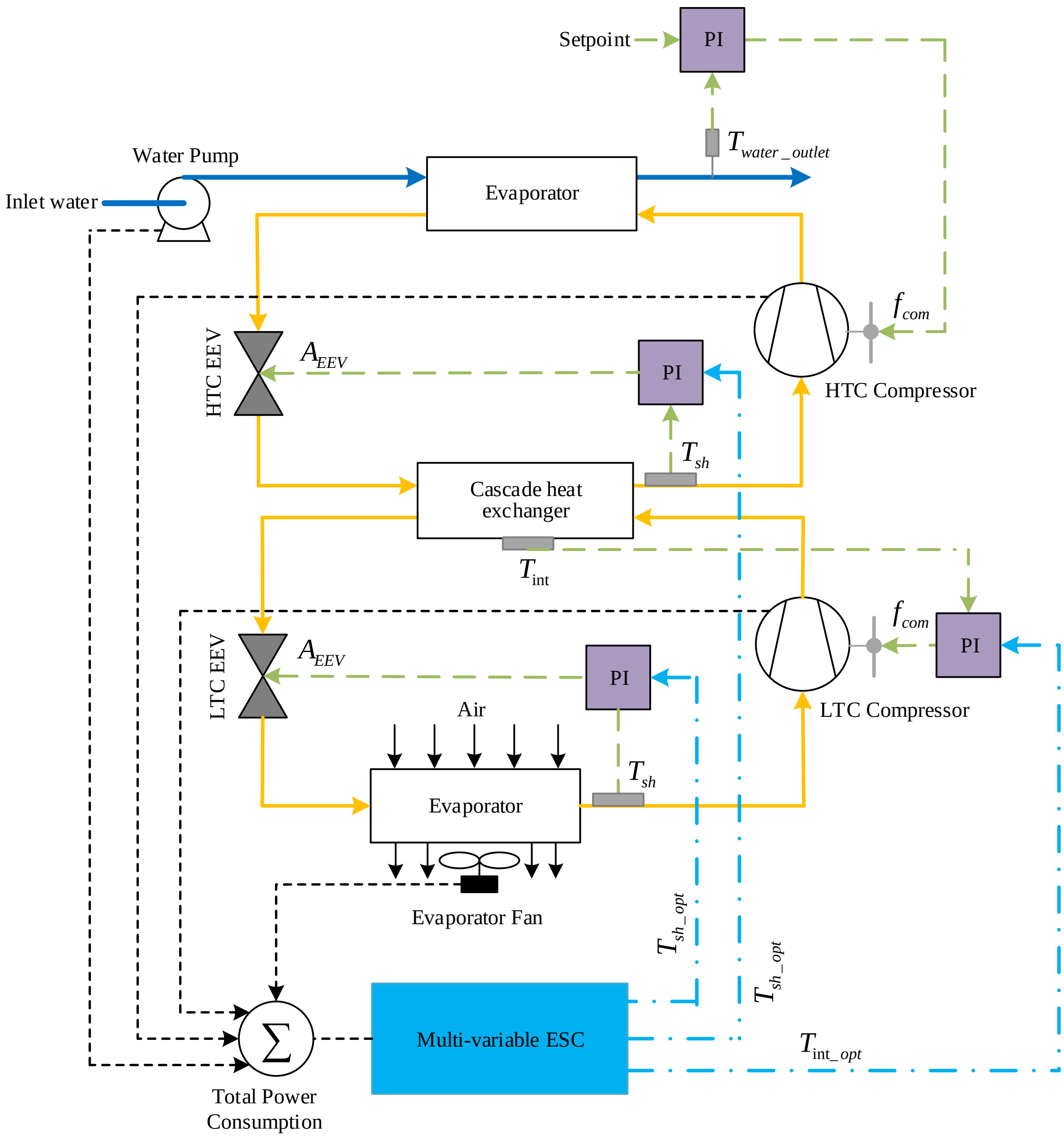


Figure 5.1. Schematic diagram for ESC based power minimization optimization under fixed heating capacity.

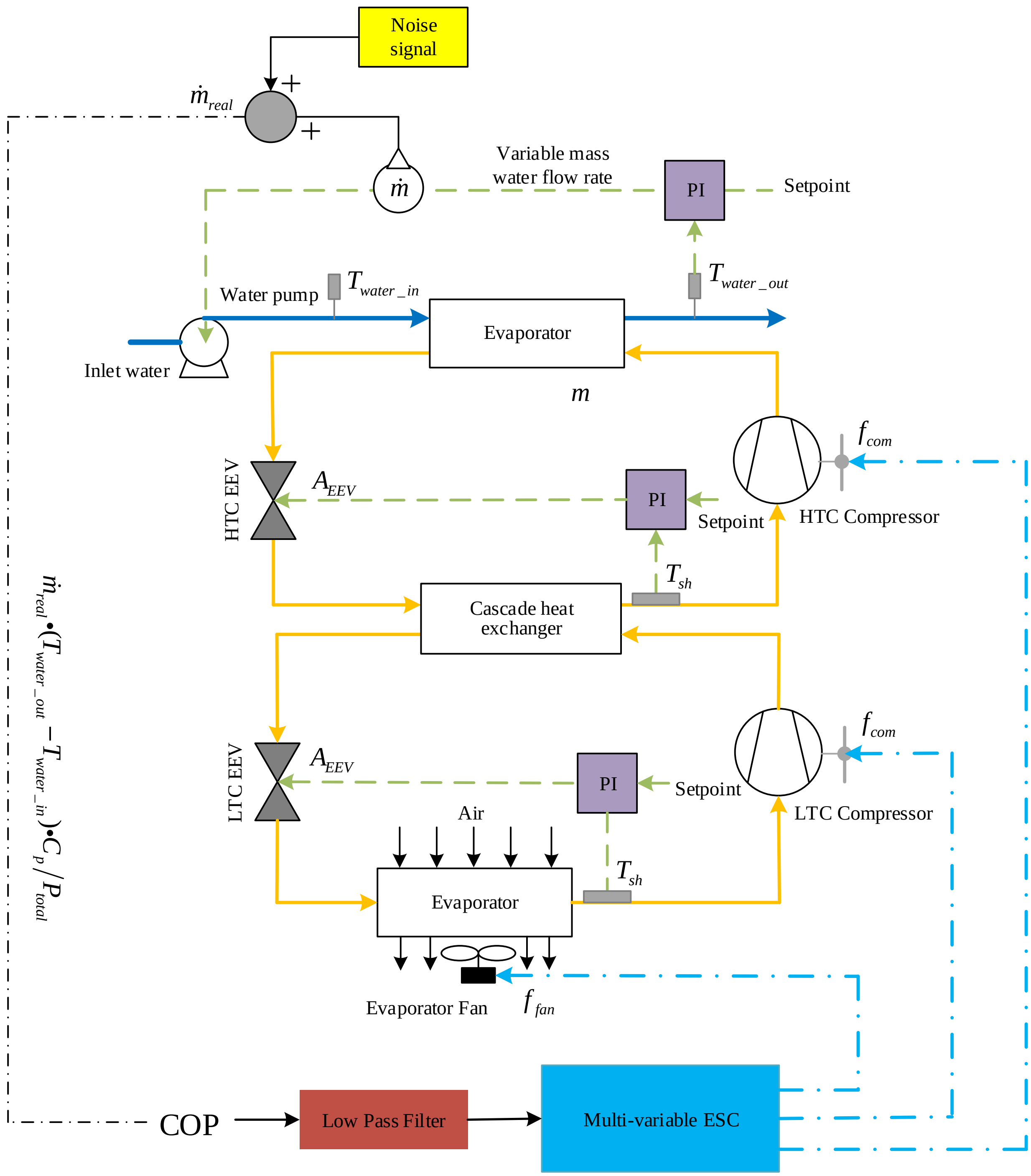


Figure 5.2. Schematic diagram for ESC based COP maximization optimization under variable heating capacity.

For the COP maximization case, the HTC condenser water pump speed is used to regulate the water outlet temperature to its setpoint. Thus, the heating capacity can be varied with ESC enabled tuning of HTC compressor speed. To better evaluate the challenge of escalating measurement noise in COP feedback, the measurement of condensing water mass flow rate is contaminated with an additive noise. The resultant COP signal as ESC feedback is thus filtered by a low-pass filter. The manipulated inputs include the HTC compressor speed, the LTC compressor speed and the evaporator fan mass flow rate.

In this model, the scroll compressor is modeled with the scroll compressor module (*TIL.VLEFluidComponents.Compressors.ScrollCompressor)* in the TIL library. It can calculate the instantaneous power consumption, and has been calibrated with measurement data of a specific compressor. Mathematical description of the scroll compressor model is presented in the Appendix A. In the TIL library, the heat exchanger models are based on the finite volume method, and the Newton's law of cooling $\dot{Q} = UA\Delta T(t)$ is applied for calculating the heat flow rate for every cell of control volume. The evaporator in LTC is modeled as a fin-and-tube cross-flow heat exchanger, with (*TIL.HeatExchangers.FinAndTube.MoistAirVLEFluid.CrossFlowHX)* module. Air-side and refrigerant-side heat transfer coefficients $h_{c,air}$ and $h_{c,ref}$ can be calculated by [183]:

$$h_{c,air} = \frac{Nu\lambda}{d_e}, \; Nu = 0.31\Pr^{0.333}\mathrm{Re}^{0.625}\left(\frac{d_e}{D_{tube}}\right)^{0.333} \tag{5-4}$$

$$h_{c,ref} = \left(\frac{1.8}{N^{0.8}}\right)\left(\frac{\lambda_{ref}}{D_{hyd}}0.023\mathrm{Re}^{0.8}\Pr^{0.4}\right) \tag{5-5a}$$

$$N = 0.38Fr^{-0.3}\left(\frac{1-x}{x}\right)^{0.8}\left(\frac{\rho_v}{\rho_l}\right)^{0.5} \tag{5-5b}$$

where Nu denotes the Nusselt number, $\lambda$ refers to the thermal conductivity, $d_e$ refers to the equivalent diameter. Pr denotes the Prandtl number, 'Re' denotes Reynolds number, and $D_{tube}$ refers to the serial tube distance. $D_{hyd}$ refers to the hydraulic diameter, Fr refers to the Froude number, $x$ refers to streaming stream mass fraction, and $\rho$ refers to density. Subscripts '*ref*', '*v*' and '*l*' refers to the refrigerant, vapor phase and liquid phase, respectively.

The CHE is modeled with the plate heat exchanger module (*TIL.HeatExchangers.Plate. VLEFluidVLEFluid.ParallelFlowHX)*. It works as a condenser for the LTC and an evaporator for the HTC. The specific heat transfer coefficient for the evaporating side is same as Eq. (5-5). The heat transfer coefficient for the condensing side is calculated as [184].

$$h_{c,ref} = 0.023\,\mathrm{Re}^{0.5}\,\mathrm{Pr}^{0.4}\left[(1-x)^{0.8} + \frac{3.8x^{0.76}(1-x)0.04}{(p/p_{crit})^{0.38}}\right] \tag{5-6}$$

where $p$ refers to the pressure, and subscript '*crit*' refers to the critical value.

The HTC condenser is also modeled by the same plate heat exchanger module. The correlation for the refrigerant side is same as Eq. (5-6), while that for the water side follows

$$h_{c,water} = \frac{Nu\lambda}{d_e} \tag{5-7a}$$

$$Nu = 0.122\,\mathrm{Pr}\frac{1}{3}\left(\frac{\eta_{water}}{\eta_{wall}}\right)^{\frac{1}{6}}(\varsigma\,\mathrm{Re}^2\sin(2\varphi))^{0.374} \tag{5-7b}$$

where $h_{c,water}$ refers to the condenser water-side heat transfer coefficient, $\eta_{water}$ refers to the viscosity of water, and $\eta_{wall}$ refers to the viscosity based on wall temperature. $\varsigma$ is the geometry factor and $\varphi$ is the mean angle.

The expansion valve is modeled with module *TIL.VLEFluidComponents.Valves.OrificeValve*, which is an orifice valve module modeled as a static isenthalpic process. The evaporator fan is modeled with the *TIL.GasComponents.Fans.SimpleFan* module, with operation characterized by either flow rate or pressure change. By use of the module of *TIL.LiquidComponents.Pumps.SimplePump*, the water pump is modeled with an affinity-law map. The separator module *TIL.VLEFluidComponents.Separators.Separator* is used to model the liquid receiver at the condenser outlet. The filling station module *TIL.VLEFluid Components.FillingStations.FillingStation* is used to specify refrigerant charge amount.

## 5.3 ESC Design and Simulation for Power Minimization under Fixed Heating Capacity

### 5.3.1. ESC design for power minimization under fixed heat capacity

For the operational scenario of fixed heating capacity, a multivariable ESC is designed to minimize the total power. It is noteworthy that, with fixed heating capacity, the minimal total power implies the maximal COP. For this ESC design, the intermediate temperature, the HTC superheat and the LTC superheat setpoints are used as the manipulated inputs. The inner-loop controllers as depicted in Figure 5.1 imply that the corresponding control authorities are the LTC compressor speed, the HTC and LTC expansion vale openings. The HTC compressor speed is used to maintain the water outlet temperature setpoint (i.e. the heating capacity).

To design the multivariable ESC, the input dynamics are estimated with step tests under the following operation condition. The water inlet temperature is fixed at 80°C, and the outlet temperature is regulated to 85°C with the HTC compressor speed via a PI controller. The water mass flow rate is fixed at 2.8 kg/s. The dry-bulb and wet-bulb temperatures of the ambient air are set to be −7°C and −7.4°C, respectively. The volumetric flow rate for the evaporator fan is fixed at 30,000 m$^3$/h. To estimate the dynamics from the intermediate temperature setpoint to the total power, the HTC and LTC superheat setpoints are both fixed at 5 K. The intermediate temperature follows step changes of +2°C from 30°C, 32°C, 34°C, 36°C and 38°C, respectively. Figure 5.3 plots the normalized step responses, and the input dynamics for the intermediate temperature channel is estimated as

$$\hat{F}_{I,INT}(s) = \frac{\omega_{n,INT}^2}{s^2 + \xi_{INT}\omega_{n,INT}s + \omega_{n,INT}^2} = \frac{0.015^2}{s^2 + 1.58 \times 0.015s + 0.015^2} \tag{5-8}$$

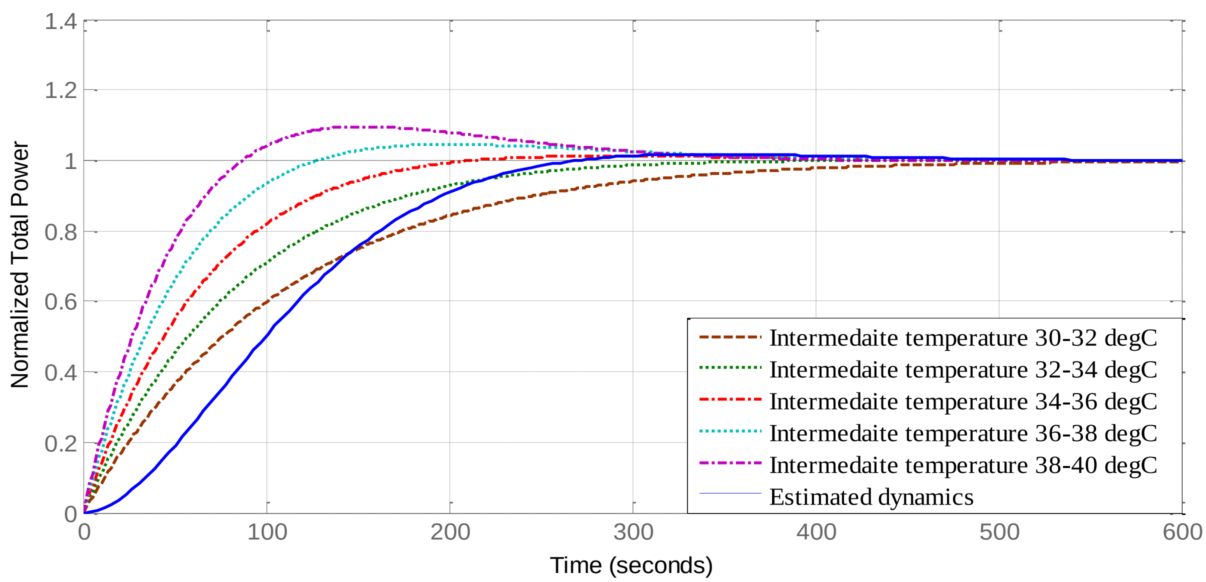


Figure 5.3. Normalized step responses from the intermediate temperature to the total power.

Based on the ESC design guidelines as reviewed in Section 2.4 a dither signal of 0.0042 rad/s and 0.5°C amplitude is then selected for the LTC compressor channel. The BP and LP filters are chosen as

$$F_{BP,INT}(s) = \frac{\xi_{BP}\omega_{BP}s}{s^2 + \xi_{BP}\omega_{BP}s + \omega_{BP}^2} = \frac{1.4 \times 0.0042s}{s^2 + 1.4 \times 0.0042s + 0.0042^2} \tag{5-9}$$

$$F_{LP,INT}(s)=\frac{\omega_{LP,INT}^{2}}{s^{2}+\xi_{LP,INT}\omega_{LP,INT}s+\omega_{LP,INT}^{2}}=\frac{0.0006^{2}}{s^{2}+1.8\times 0.0006s+0.0006^{2}} \tag{5-10}$$

Figure 5.4 shows the Bode plots for the estimated input dynamic, BP and LP filters, with the dither frequency labeled. The phase compensation for demodulation signal is chosen as –0.46 radian.

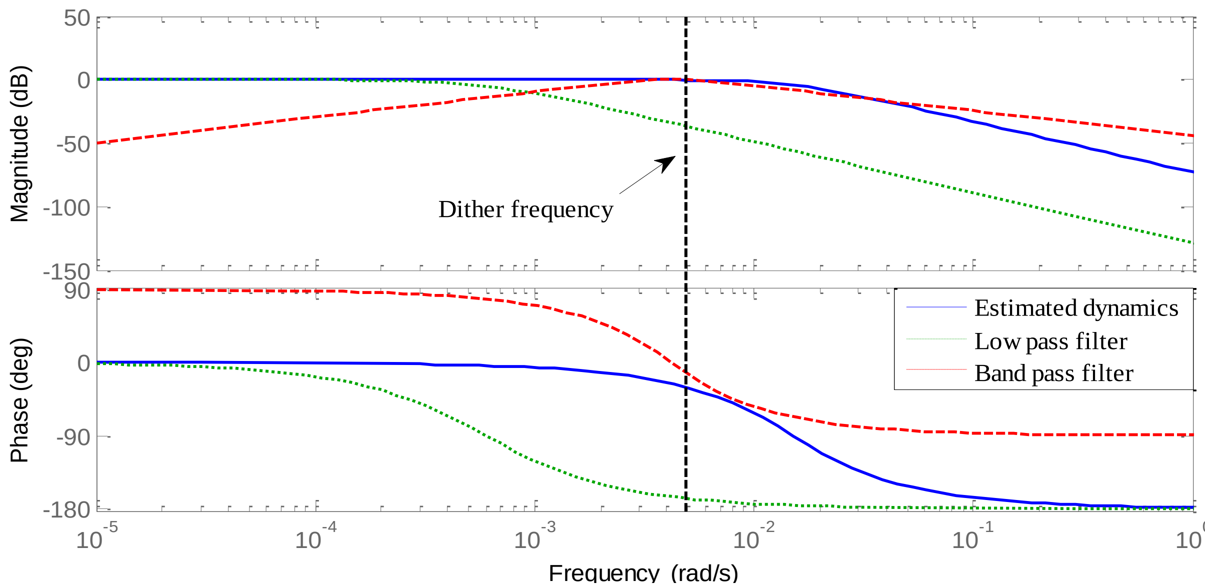


Figure 5.4. Bode plots of input dynamics, BP and LP filters for the intermediate temperature channel.

Then, this procedure is repeated for estimating the input dynamics for the HTC and LTC superheat setpoints. For the HTC superheat channel, the intermediate temperature and the LTC superheat are fixed at 35°C and 5°C, respectively. Step changes of +2°C is applied to the HTC superheat, starting from 3°C, 5°C and 7°C respectively. Then for the LTC superheat channel, the intermediate temperature and the HTC superheat are fixed at 35°C and 5 K, respectively. Similarly, step changes of +2°C is also applied to the LTC superheat, starting from 3°C, 5°C and 7°C respectively. The ESC parameters for all three channels are summarized in Table 5.2.

Table 5.2. ESC design parameters for the three loop.

| Parameter | Input Channel | | |
|---|---|---|---|
| | Intermediate Temp. | HTC Superheat | LTC Superheat |
| Dither Frequency (rad/s) | 0.0042 | 0.0064 | 0.0072 |
| Dither Amplitude (°C) | 0.5 | 0.5 | 0.5 |
| Demodulation Amplitude (°C) | 2/0.5 | 2/0.5 | 2/0.5 |
| Gain | 4 | 2 | 3.5 |
| $\omega_{BP}$ (rad/s) | 0.0042 | 0.0064 | 0.0072 |
| $\omega_{LP}$ (rad/s) | 0.0006 | 0.001 | 0.002 |
| $\varphi$ (rad) | -0.46 | -0.59 | -0.65 |
| $\xi_{BP}$ | 1.4 | 2 | 2 |
| $\xi_{LP}$ | 1.8 | 1.8 | 1.8 |

In the simulation, several inner-loop controllers are implemented for regulating some key process variables. For the case of power minimization under the fixed heating capacity, four inner-loop controllers are implemented. i) The intermediate temperature setpoint is regulated by the LTC compressor frequency via a PI controller. ii) The LTC superheat setpoint is regulated by the LTC expansion valve opening with another PI controller. iii) The HTC superheat setpoint is regulated by the HTC expansion valve with a PI controller. iv) The water outlet temperature is regulated by the HTC compressor speed, in order to meet the heating capacity. The water outlet temperature setpoint is set as 85°C. The specific design specifications of the four PI controllers are shown in Table 5.3.

Table 5.3. Design specifications of the PI controllers

| | Proportional gain ($k$) | Time constant ($T_i$) | Initial output of controller |
|---|---|---|---|
| Intermediate temperature PI | 1 | 7 | 50 |
| LTC Superheat PI | $1\times10^{-5}$ | 100 | $2.5\times10^{-7}$ |
| HTC Superheat PI | $1\times10^{-5}$ | 100 | $2.5\times10^{-7}$ |
| Water outlet temperature PI | 1 | 7 | 50 |

#### 5.3.2. Simulation study for power minimization under fixed heating capacity

The designed ESC is then simulated with the CASHP model in Dymola under both fixed and realistic ambient temperature profiles for fixed heating capacity operation. The convergence characteristic is evaluated with the settling time for the performance index, i.e. the total power in this case, and/or the COP. The steady-state performance is evaluated with the optimum found with the offline simulation based global optimization procedure using the Sequential Quadratic Programming algorithm, same as the study of VI ASHP with IHXC and FTC in Chapters 3 and 4. For the CASHP, the tolerance of SQP optimization is set as small as $1\times10^{-6}$ through the study.

##### 5.3.2.1. Simulation under fixed ambient temperature

The ESC strategy is first evaluated under the fixed condition that is same as that for the ESC design in Section 5.3.1. Figure 5.5 shows the trajectories of ESC inputs and out. The initial value for the intermediate temperature, HTC and LTC superheat setpoints are 45°C, 4°C and 13°C, respectively. Then the corresponding total power and COP under the initial value are 31.26 kW and 1.84 respectively. The HTC and LTC compressor speeds are 37.8 Hz and 60.3 Hz, respectively. The HTC and LTC EEV openings are 9.77 mm$^2$ and 5.45 mm$^2$, respectively.

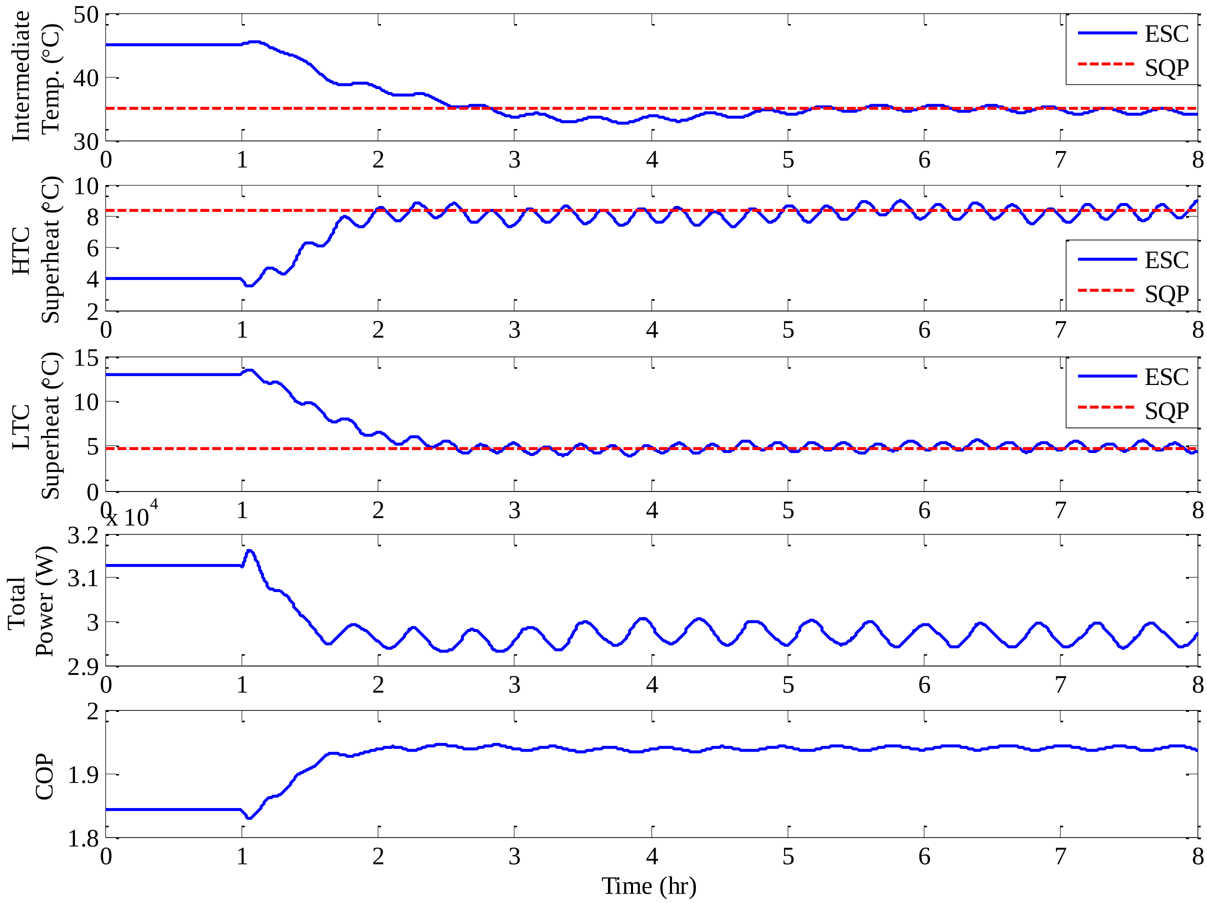


Figure 5.5. Trajectories of intermediate temperature, HTC and LTC superheats, total power and COP for ESC under fixed ambient temperature with initial intermediate temperature of 45°C.

With the ESC turned on at 1 hour as shown in Figure 5.5, the total power decreases from 31.26 kW to 29.5 kW with a settling time of about 2260 seconds. The COP increases from 1.84 to 1.95, i.e. a 6.0% increase in system performance from the initial value. Meanwhile, it reveals that the optimal intermediate temperature found by ESC is 34.9°C compared to the optimum of 35.0°C found by the SQP (shown as the red dashed line), i.e. the steady-state error is only 0.3%. The optimal superheats for the HTC and LTC found by ESC are 8.3°C and 4.75°C, respectively. Compared to the respective optimum values of 8.34°C and 4.72°C found by SQP, the steady-state errors are only 0.48% and 0.64%, respectively. The settling time for the three inputs appears longer than the output: 6500 seconds for the intermediate temperature, 3600 seconds for the HTC superheat and 5700 seconds for the LTC superheats. This is due to the fact that the sensitivity of the total power in terms of the associated manipulated variables is smaller, i.e. the ‘improvement’ of energy efficiency can be marginal as the static map becomes ‘flatter’ during the ‘last move’ towards the optimum.

Figure 5.6 shows the trajectories relevant to the inner-loop regulations, i.e. the LTC compressor speed for regulating the intermediate temperature, the HTC compressor speed for regulating the water outlet temperature, and the HTC and LTC EEV openings for regulating the respective superheat setpoints. The steady-state compressor speed for the LTC reaches 38.9 Hz, meanwhile for maintaining the setpoint of water outlet temperature, the HTC compressor speed is increased to 50 Hz. The HTC and LTC EEV openings are settled at 8.98 $mm^2$ and 5.83 $mm^2$, respectively. Finally, the water outlet temperature is shown to be maintained very well at 85°C through the whole simulation. Figure 5.7 shows the gradient trajectories of the intermediate, HTC and LTC superheat channels, all converging to the neighborhood of zero, respectively. This validates that the ESC successfully converges the operation to the optimum.

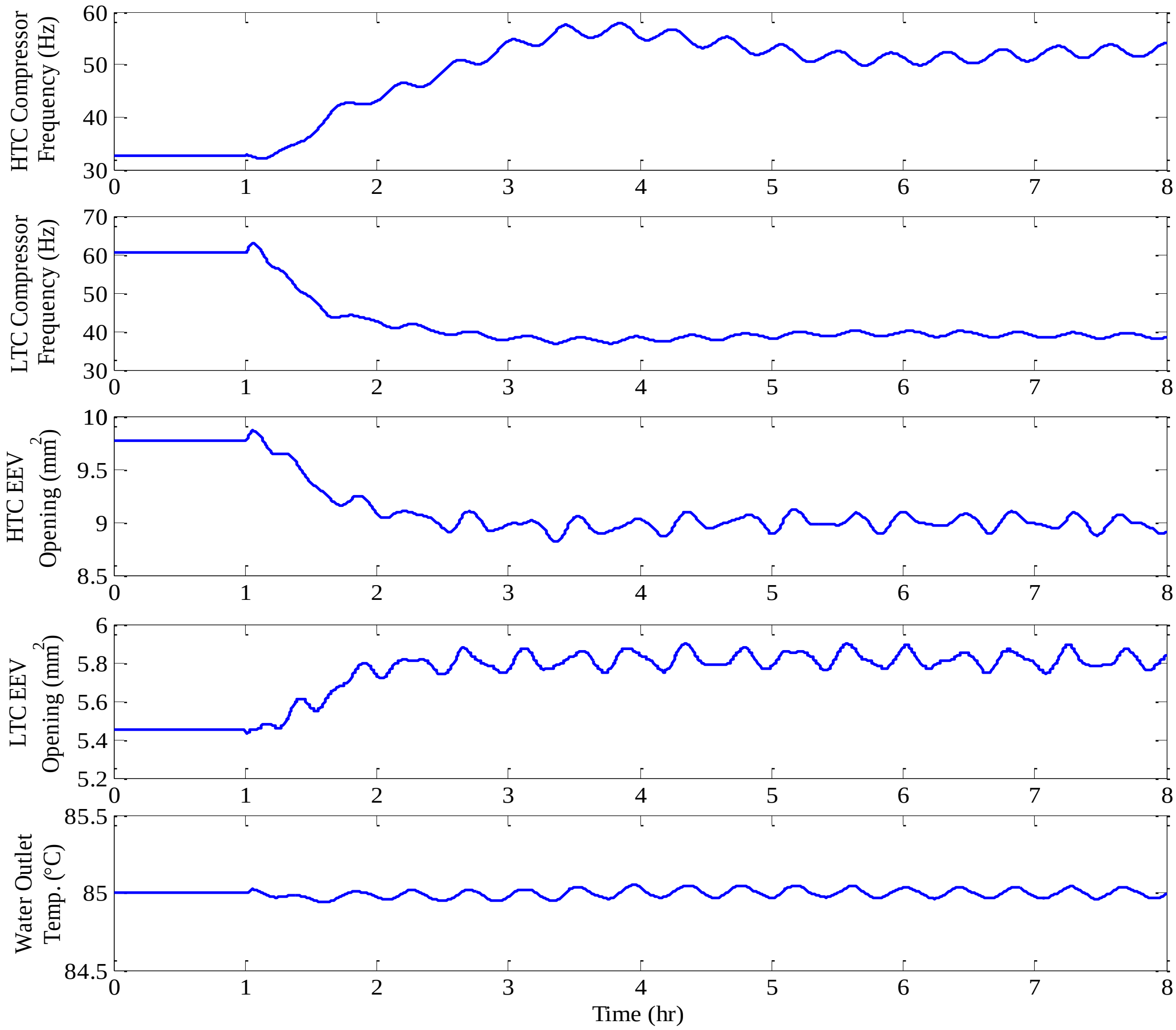


Figure 5.6. Trajectories of compressor speeds, EEV openings, water outlet temperature for ESC simulation under fixed ambient temperature with initial intermediate temperature of 45°C.

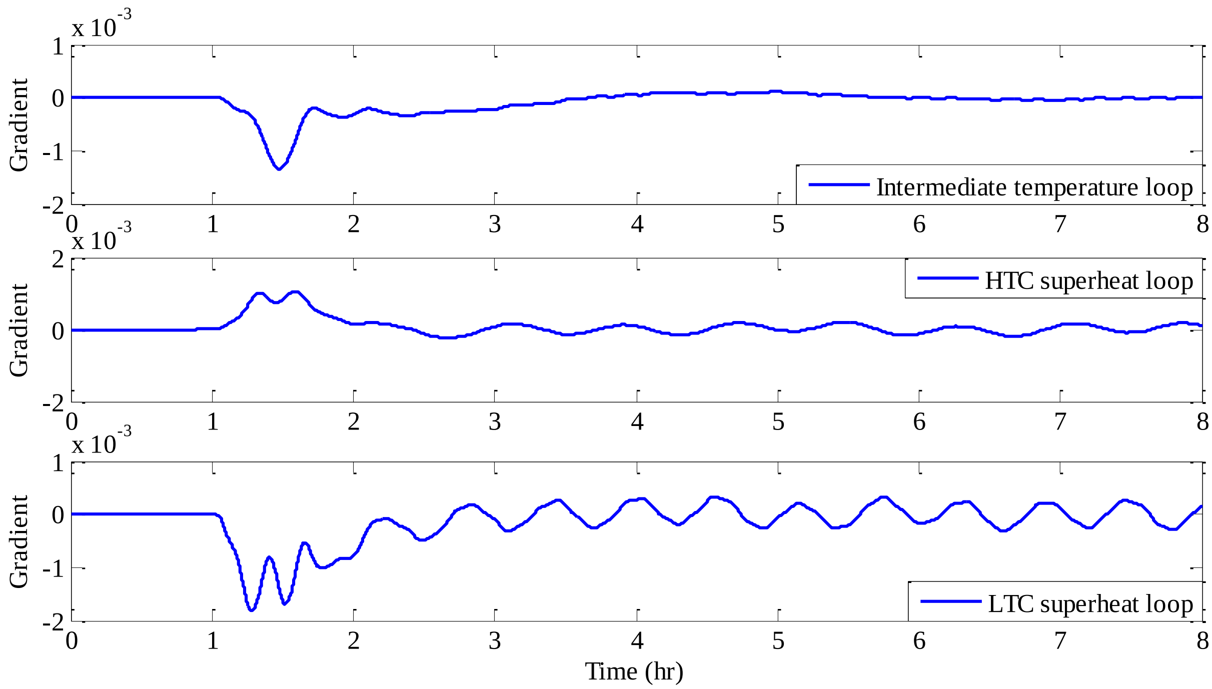


Figure 5.7. Gradient trajectories for ESC simulation of CASHP under fixed ambient temperature with initial intermediate temperature of 45°C.

To further justify the consistency of the ESC strategy, the simulation is conducted under the same scenario, except that the initial values of the three input channels are located at another side of the optimum. The initial values for the intermediate temperature, HTC and LTC superheats are set to be 30°C, 15°C and 2°C, respectively. As shown in Figure 5.8, with the ESC turned on at $t$ = 1 hour, the optimal intermediate temperature, HTC and LTC superheat setpoints settle at 34.9°C, 8.3°C and 4.9°C, respectively, which are nearly the same as those in the previous case. The total power and COP converge to 29.6 kW and 1.94, respectively, which again are almost identical to those of the previous case. Figure 5.9 shows the trajectories of control authorities: the HTC and LTC compressor speeds are settled to 51.8 Hz and 39.0 Hz, respectively, while the HTC and LTC EEV openings are settled to 8.99 $mm^2$ and 5.88 $mm^2$, respectively. All these values are consistent with those from the previous case starting from a different side of the optimum. Also, through the whole simulation, the water outlet temperature is well maintained at 85°C. Figure 5.10 shows the gradient trajectories for the intermediate temperature, the HTC and LTC superheat channels, which all have converged to the neighborhood of zero. Again, it validates that the ESC can successfully converges the system operation to the optimum with the initial inputs at a different side of the optimality.

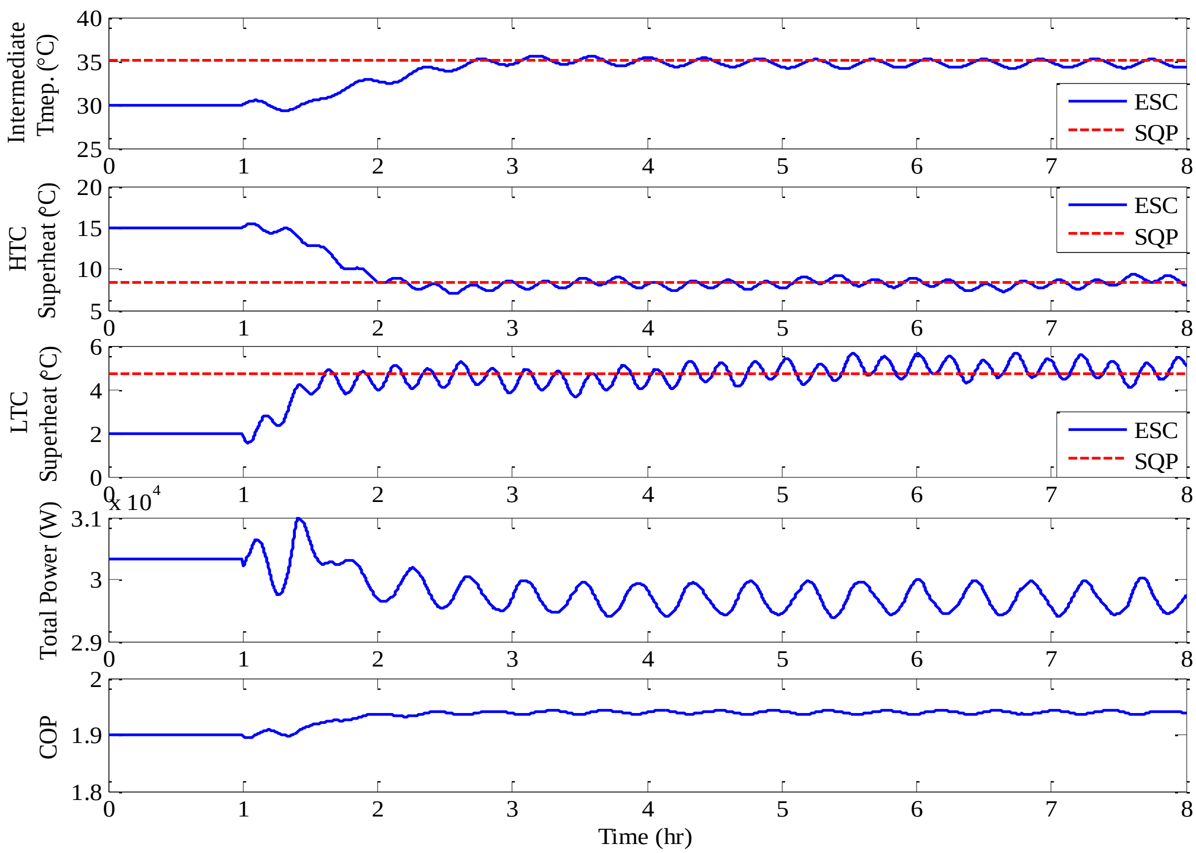


Figure 5.8. Trajectories of intermediate temperature, HTC and LTC superheats, total power and COP for ESC under fixed ambient temperature with initial intermediate temperature of 30°C.

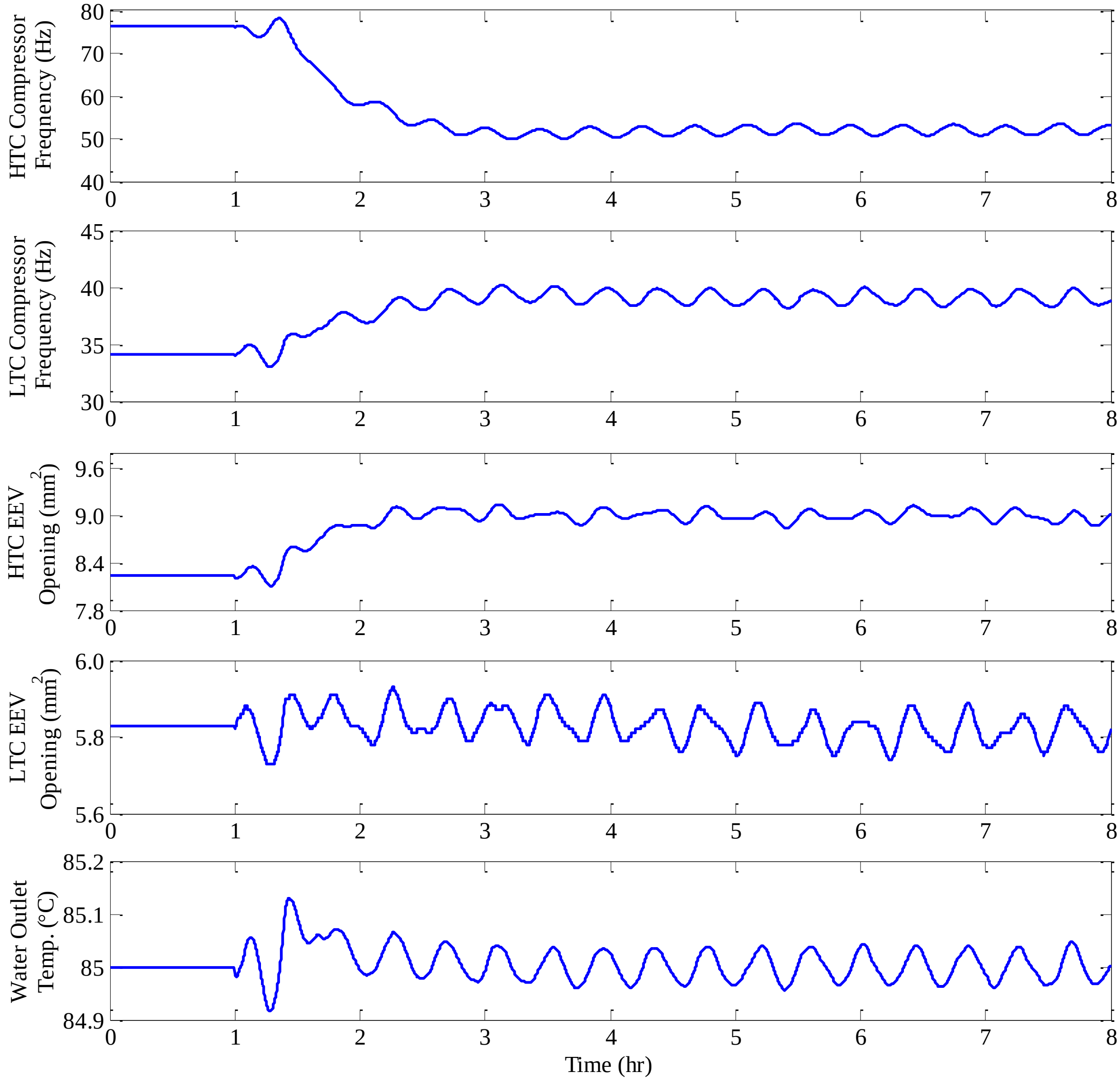


Figure 5.9. Trajectories of compressor speeds, EEV openings, water outlet temperature for ESC simulation under fixed ambient temperature with initial intermediate temperature of 30°C.

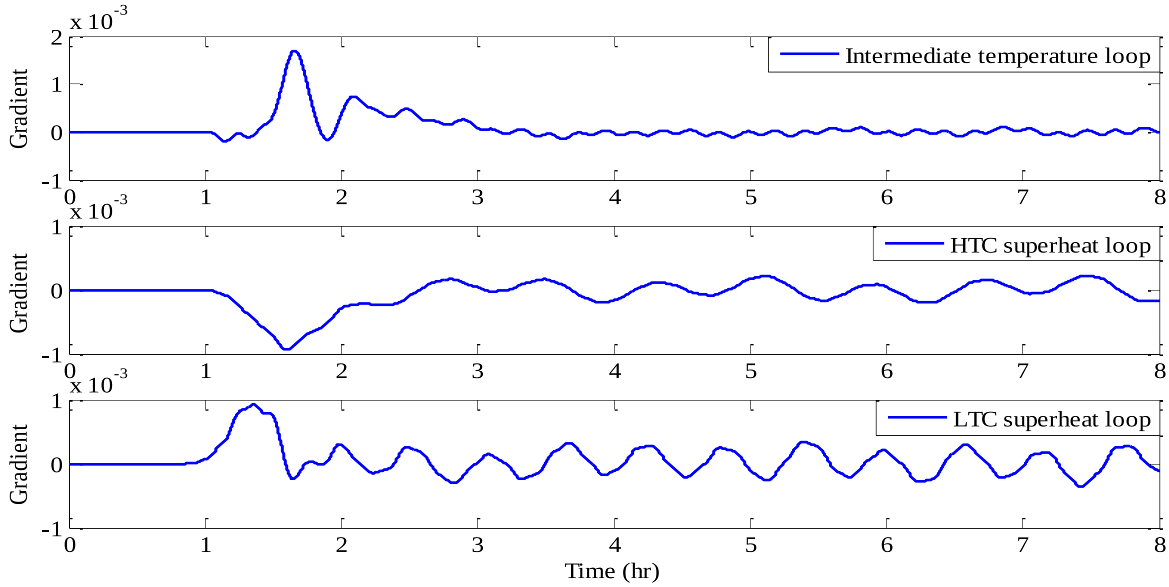


Figure 5.10. Gradient trajectories for ESC simulation of CASHP under fixed ambient temperature with initial intermediate temperature of 30°C.

To further evaluate the effectiveness of the ESC strategy, more simulations are conducted under ambient temperatures from 2°C to −15°C, with increment of 1°C. The steady-state and transient performance are summarized in Table 5.4, which includes the initial values and steady-state values of all three manipulated input as well as the settling time evaluated with the total power trajectories. The relative errors ('RE') of the manipulated inputs are calculated with respect to the respective optimum obtained by SQP procedure. It shows that the three manipulated inputs can all converge to the respective optimum very well across all ambient temperatures evaluated. The maximal RE between the ESC and SQP is 0.9%, 0.8% and 0.68% for the intermediate temperature loop, HTC superheat loop and LTC superheat loop, respectively. For these simulation cases, the settling time ranges from 2,450 seconds to 3,900 seconds. The moderate variation of convergence time is due to the nonlinear nature of the ESC system, i.e. the settling time depends on the initial condition.

Table 5.4. The optimal value comparison between the ESC and SQP under the different ambient temperature.

| Ambient Temp. (°C) | Initial values of Tint /SHHTC /SHLTC (all °C) | Intermediate Temp. (°C) | | | HTC Superheat (°C) | | | LTC Superheat (°C) | | | Settling Time (sec) |
|---|---|---|---|---|---|---|---|---|---|---|---|
| | | ESC | SQP | RE (%) | ESC | SQP | RE (%) | ESC | SQP | RE (%) | |
| 2 | (47/4/13) | 38 | 37.9 | 0.26 | 7.91 | 7.95 | 0.50 | 5.0 | 4.99 | 0.20 | 2870 |
| 1 | (47/4/13) | 37.6 | 37.5 | 0.26 | 7.94 | 7.98 | 0.50 | 4.98 | 4.97 | 0.20 | 2600 |
| 0 | (47/4/13) | 37.4 | 37.3 | 0.27 | 8.01 | 8.05 | 0.49 | 4.94 | 4.95 | 0.20 | 2450 |
| -1 | (28/15/2) | 36.9 | 36.8 | 0.27 | 8.05 | 8.09 | 0.49 | 4.89 | 4.91 | 0.41 | 3400 |
| -2 | (28/15/2) | 36.5 | 36.4 | 0.27 | 8.09 | 8.13 | 0.49 | 4.86 | 4.87 | 0.21 | 3680 |
| -3 | (28/15/2) | 36.2 | 36.2 | 0 | 8.12 | 8.15 | 0.37 | 4.84 | 4.82 | 0.42 | 3900 |
| -4 | (45/4/13) | 35.8 | 35.9 | 0.28 | 8.16 | 8.19 | 0.37 | 4.81 | 4.79 | 0.41 | 2910 |
| -5 | (45/4/13) | 35.4 | 35.5 | 0.28 | 8.21 | 8.24 | 0.36 | 4.79 | 4.77 | 0.42 | 2790 |
| -6 | (45/4/13) | 35.1 | 35.2 | 0.28 | 8.24 | 8.26 | 0.24 | 4.78 | 4.76 | 0.42 | 2450 |
| -7 | (45/4/13) | 34.9 | 35.0 | 0.28 | 8.30 | 8.34 | 0.48 | 4.75 | 4.72 | 0.64 | 2260 |
| -8 | (26/15/2) | 34.3 | 34.4 | 0.29 | 8.33 | 8.38 | 0.58 | 4.70 | 4.68 | 0.43 | 3650 |
| -9 | (26/15/2) | 33.9 | 34.0 | 0.29 | 8.39 | 8.44 | 0.59 | 4.65 | 4.64 | 0.22 | 3480 |
| -10 | (43/4/12) | 33.5 | 33.6 | 0.3 | 8.42 | 8.47 | 0.59 | 4.60 | 4.58 | 0.44 | 3100 |
| -11 | (43/4/12) | 33.0 | 33.1 | 0.3 | 8.51 | 8.56 | 0.58 | 4.58 | 4.56 | 0.44 | 2840 |
| -12 | (43/4/12) | 32.5 | 32.6 | 0.31 | 8.58 | 8.64 | 0.70 | 4.55 | 4.53 | 0.44 | 2570 |
| -13 | (24/15/2) | 31.9 | 32.1 | 0.6 | 8.69 | 8.76 | 0.80 | 4.49 | 4.46 | 0.67 | 3250 |
| -14 | (24/15/2) | 31.4 | 31.6 | 0.6 | 8.80 | 8.87 | 0.79 | 4.43 | 4.40 | 0.68 | 3000 |
| -15 | (24/15/2) | 30.8 | 31.1 | 0.9 | 8.91 | 8.98 | 0.78 | 4.34 | 4.35 | 0.23 | 2800 |

#### 5.3.2.2. Simulation under realistic ambient temperature

Then the ESC is simulated under a realistic ambient temperature profile. A 120-hour TMY3 (*Buildings.BoundaryConditions.WeatherData.ReaderTMY3*) record from January 1$^{st}$ to 5$^{th}$ of the ambient temperature profile at the O'Hare Airport in Chicago. As shown in the uppermost plot in Figure 5.11, this profile has the ambient temperature ranging from +2°C to −15°C, which covers all the ambient temperatures considered in the cases in Table 5.4. Such range of ambient temperature makes the evaluation more persuasive.

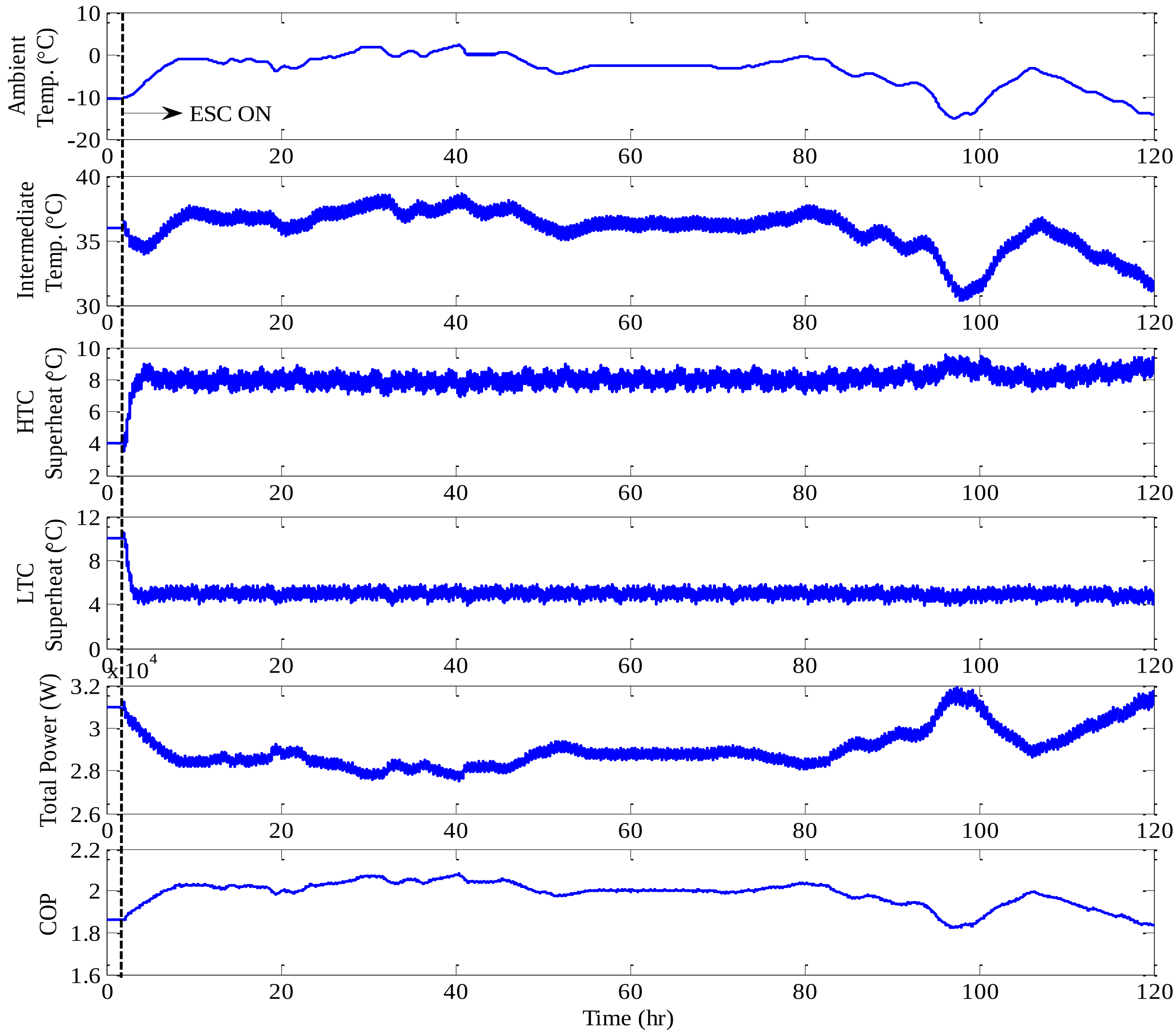


Figure 5.11. Trajectories of ambient temperature, intermediate temperature, HTC and LTC superheat, total power and COP for ESC simulation under the realistic ambient temperature profile.

First, the CASHP is operated with the initial values of intermediate temperature, HTC and LTC superheats at 36°C, 4°C and 10°C, respectively. Then the ESC is turned on at $t$ = 2 hours. Figure 5.11 shows the trajectories of the intermediate temperature, HTC and LTC superheat, as well as the total power consumption and COP. In Figure 5.12, the trajectory of water outlet temperature shows a quality load regulation, in spite of a dynamically varying ambient temperature. Other key process variables also demonstrate reasonable behavior. It is noteworthy that the optimal HTC and LTC superheats are shown not as sensitive to the ambient temperature as the intermediate temperature, and thus their optimum values do not change much through the whole simulation.

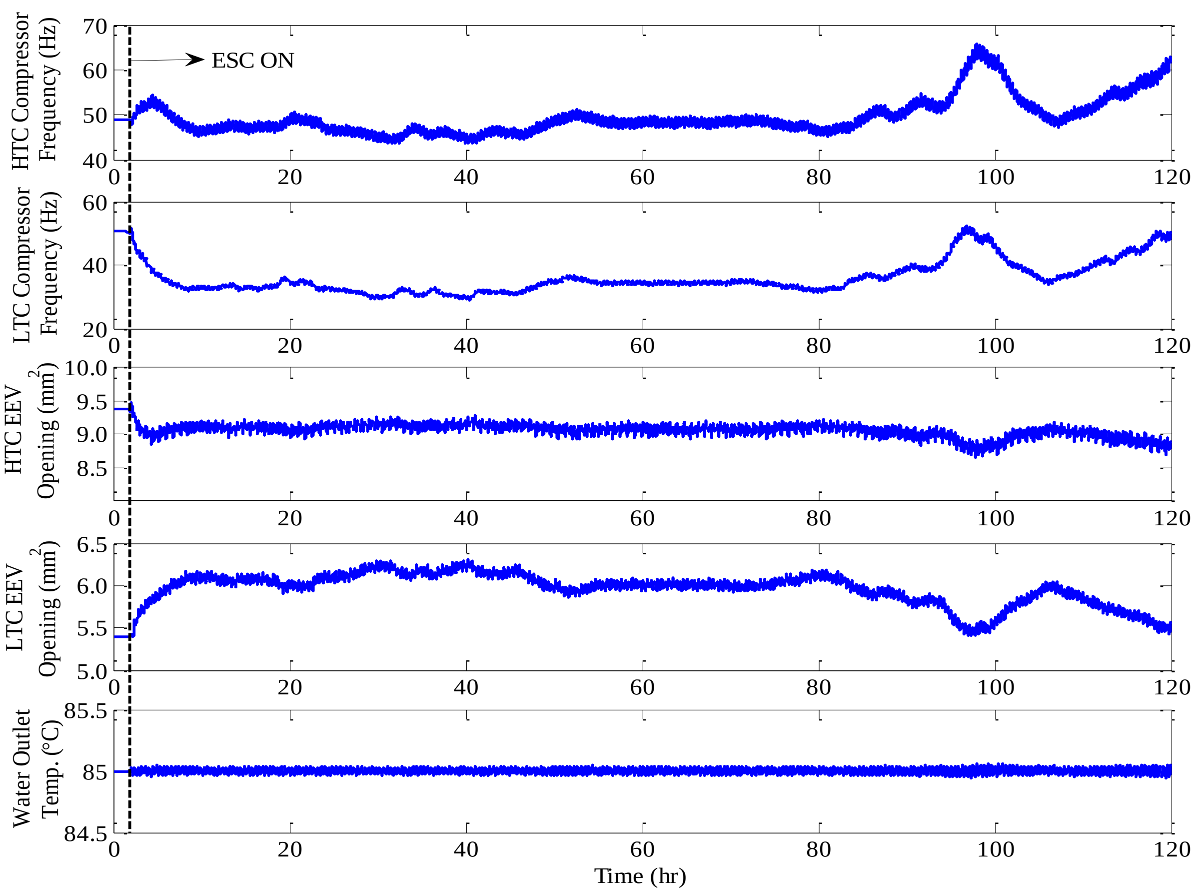


Figure 5.12. Trajectories of compressor speeds, EEV openings, water outlet temperature for ESC simulation under the realistic ambient temperature profile.

To evaluate the effectiveness of dynamic tracking of the actual optimum, Figure 5.13 plots the trajectories of the intermediate temperature found by the ESC (solid line) and that found by SQP (dashed line). The actual optimum is found with SQP under the ambient temperature ranging from +2°C to –15°C with increment of 0.1°C. The maximal gap between the ESC and SQP is 0.2°C (about 0.7% relative error) at the ambient temperature of –14°C. Overall, the ESC shows a nice and smooth dynamic tracking of actual optimum for a realistic ambient condition.

Figure 5.14 shows the gradient trajectories of for the intermediate temperature, the HTC and LTC superheat channels under the realistic ambient temperature profile. The gradients for the HTC and LTC superheats are nearly zero, that is consistent with the small changes in the HTC and LTC superheats shown in Figure 5.11.

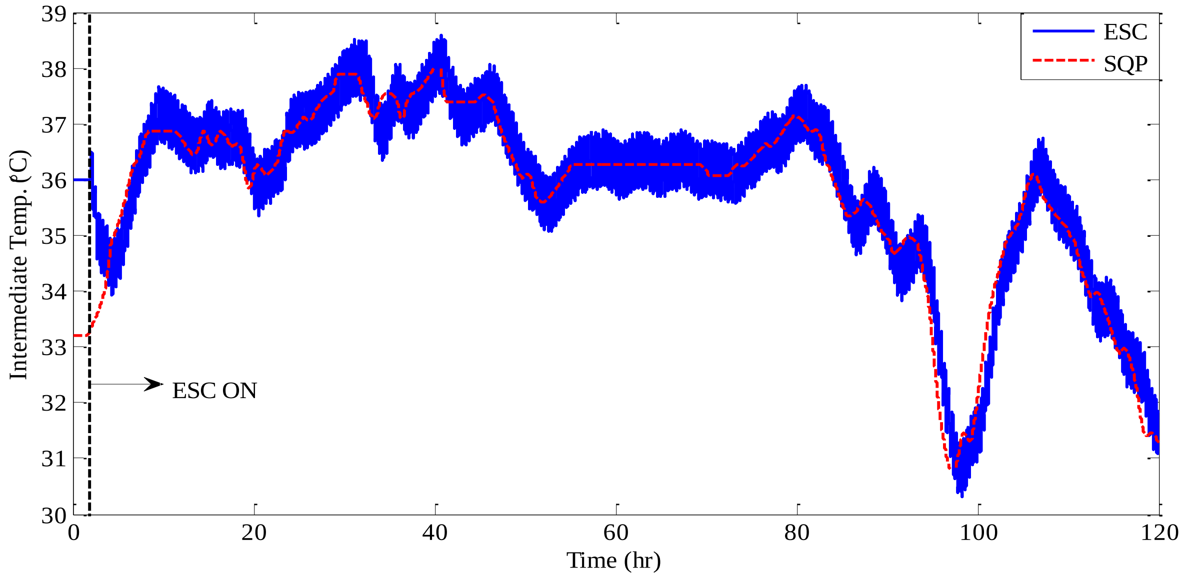


Figure 5.13. Comparison of intermediate temperature trajectories found by ESC and SQP under the realistic ambient temperature profile.

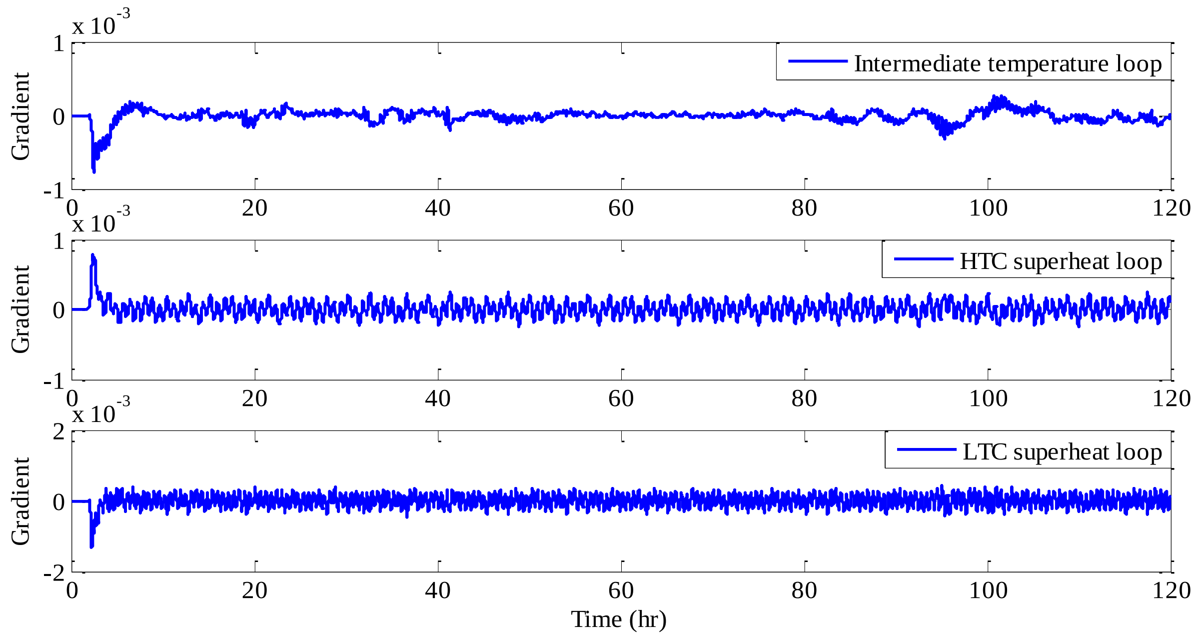


Figure 5.14. Trajectories of gradient for intermediate temperature, HTC and LTC superheat loop for ESC simulation under the realistic ambient temperature profile.

To further evaluate the proposed ESC control strategy, the ESC is benchmarked against a benchmark control strategy that has been adopted by a CASHP manufacturer. In this benchmark strategy, the LTC compressor speed is fixed at the nominal value of 50 Hz, and the HTC compressor is used to regulate the water outlet temperature. The HTC and LTC superheats are both set as constant of 5 K through the operation. In other words, the three manipulated inputs of the ESC are all set as constant in the benchmark method. Other operating conditions for the ESC and the benchmark are set the same. The water inlet temperature is 80°C, and the outlet temperature is regulated to 85°C by the HTC compressor speed via the PI controller. The mass flow rates of the evaporator fan and the water pump are both set the same as those in the ESC simulations. Figure 5.15 compares the primary simulation results under the same 120-hour ambient temperature profile as above. The water outlet temperature is again regulated well through the whole simulation period. With the ESC turned on at $t$ = 2 hour, the total power decreases rapidly and maintains a significantly lower level of power consumption through the whole simulation. The average total power is 29,060.6 Watt with the ESC as opposed to the 30,368.2 Watt with the benchmark, which indicates a 4.3% energy saving through the 5-day operation. The average COP for the ESC method is 1.98 as opposed to the 1.89 for the benchmark method.

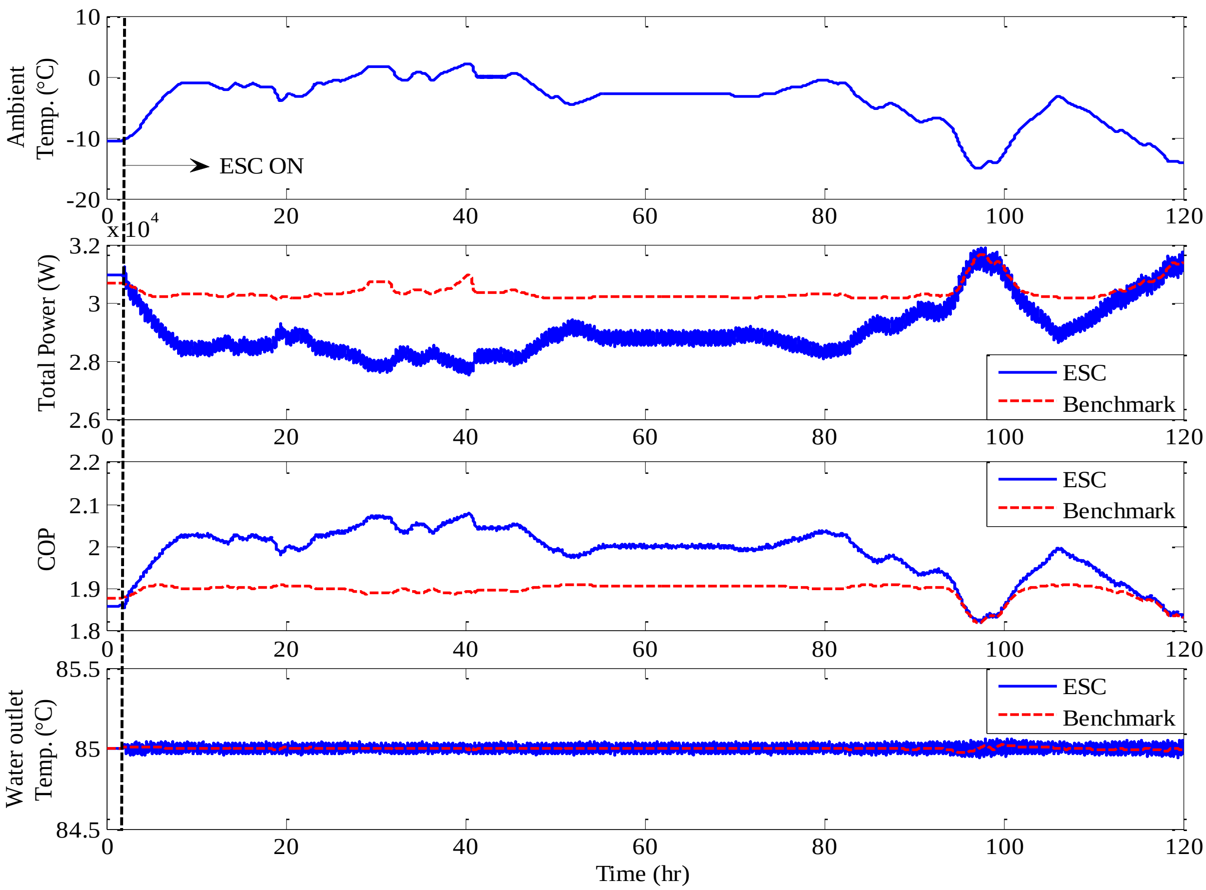


Figure 5.15. Trajectories of ambient temperature, total power, COP and water outlet temperature under the realistic ambient temperature condition with and without ESC.

In particular, it is noteworthy that the power consumption and COP of the two strategies are very close for $t \in [95, 102]$ hours, where the ambient temperature is around $-12$ to $-14$°C. This is because the nominal design was carried out under the ambient temperature of $-12$°C, i.e. the design parameters and operation settings have been somehow optimized for the nominal condition. Therefore, even without real-time optimization like ESC, the CASHP can achieve a high system performance near the nominal condition. Whereas for the periods when the ambient temperature deviates significantly from the nominal condition, the advantage of the ESC strategy is clearly revealed.

Based on the simulation results under fixed and realistic ambient temperature profiles, it has revealed that the ESC can successfully find the optimal settings for the intermediate temperature, HTC and LTC superheat without use of model knowledge, which implies significant energy saving for the CASHP operation. In other words, ESC can maintain a consistently energy efficient operation for practical operation of CASHP for the fixed heating capacity case. Furthermore, especially for the fixed heat capacity case, the ESC strategy does not need any particular measurements other than the total power metering, which makes itself a very cost-effective option for the HVAC practice.

## 5.4 ESC Design and Simulation for COP Maximization under Variable Heating Capacity

In this section, the water mass flow rate is variable, for which the optimum (i.e. maximum) COP can be searched for with the capability of ESC. For practical water heating systems, heat pumps with variable water flow can be operated by adding a water tank to meet the heat demand. With the aid of tank storage, it is possible to operate the CASHP system at the optimum COP under different ambient condition, with the heating capacity being adjusted by the water flow rate.

### 5.4.1. ESC design for COP maximization under variable heat capacity

For the ESC design for COP maximization under variable heating capacity, compared to the scenario of power minimization under fixed heating capacity, some changes are made to system operation. First, the water pump mass flow rate is used to regulate the water outlet temperature as 85°C setpoint with a PI controller, so the heating capacity is variable. Thus, the HTC compressor speed becomes a new manipulated input for ESC instead of maintaining the heating capacity.

Second, a different set of inputs are considered for ESC design. As shown in Table 5.4, the optimal superheat just shows a slight change under the different ambient temperature. To facilitate input selection for ESC design, a quantitative evaluation for the impact of HTC superheat, LTC superheat and the intermediate temperature is conducted under different ambient temperature. For each channel, the optimal values of the HTC superheat, LTC superheat and intermediate temperature are 8.3°C, 4.7°C and 35°C, respectively, under −7°C ambient temperature and the condensing water mass flow rate of 2.8kg/s. To evaluate the sensitivity of these inputs to the system COP, a number of steady-state simulations are performed with each of the manipulated inputs varied within an interval of ±4°C about the aforementioned optimum, for −7°C, −10°C and −15°C ambient temperature, respectively. For all cases, the water inlet and outlet temperatures are also set as 80°C and 85°C respectively. For each input channel, with all other inputs fixed their respective optimum value, the variation of COP is evaluated within the specified range of this input. The maximum percentage variations for the aforementioned three inputs are summarized in Table 5.5. The results show that the variations in system COP are significantly smaller for the two superheat channels, i.e. the corresponding dimensions of static map are much flatter. Therefore, for the COP based ESC, the HTC and LTC superheat setpoints are not considered as the manipulated inputs; rather, they are fixed at 8°C and 5°C, respectively. In addition, the evaporator fan is considered as an additional manipulated input for COP optimization. Finally, the manipulated inputs for the COP based ESC are determined as the HTC compressor speed, the LTC compressor speed, and the evaporator fan air mass flow rate.

Table 5.5. Maximum changes in COP for the CASHP water heater under three ambient temperatures.

| Ambient Temperature | HTC Superheat | LTC Superheat | Intermediate Temperature |
|---|---|---|---|
| −7°C | 0.31% | 0.54% | 3.11% |
| −10°C | 0.30% | 0.47% | 2.94% |
| −15°C | 0.27% | 0.42% | 2.77% |

Finally, a significant level of measurement noise is considered for COP feedback. As described earlier, the COP based ESC features larger measurement noise than the power feedback. Noise filtering is necessary for practical operation, which introduces nontrivial output dynamic that would affect the ESC design and achievable transient performance. Therefore, for the simulation study of the COP based ESC, two changes are made: 1) the water mass flow rate measurement is subject to a zero-mean Gaussian noise with the standard deviation being 3% of the mean measured value; 2) to reduce the impact of measurement noise, the COP measurement passes through a low-pass filter, as shown in Figure 5.2.

The COP based ESC for is then designed with the new set of inputs. The water inlet temperature is also fixed at 80°C, and the outlet temperature is regulated to 85°C by the water pump via a PI controller. The dry-bulb and wet-bulb ambient temperature are also set to be −7°C and −7.4°C, respectively. The HTC and LTC superheat setpoints are fixed at 8 K and 5 K respectively. For the HTC compressor speed channel, step changes of 5 Hz are applied from 45, 50 and 55 Hz, respectively. Then the input dynamics for the HTC compressor loop is estimated as

$$\hat{F}_{I,HTC\_COP}(s) = \frac{\omega_{n,HTC}^2}{s^2 + \xi_{HTC}\omega_{n,HTC}s + \omega_{n,HTC}^2} = \frac{0.04^2}{s^2 + 1.78 \times 0.04s + 0.04^2} \quad (5\text{-}11)$$

A dither signal of 0.015 rad/s and 1.5 Hz amplitude is then selected for the HTC compressor channel. The BP and LP filters are chosen as

$$F_{BP,HTC\_COP}(s) = \frac{\xi_{BP}\omega_{BP}s}{s^2 + \xi_{BP}\omega_{BP}s + \omega_{BP}^2} = \frac{1.5 \times 0.015s}{s^2 + 1.5 \times 0.015s + 0.015^2} \quad (5\text{-}12)$$

$$F_{LP,HTC\_COP}(s) = \frac{\omega_{LP}^2}{s^2 + \xi_{LP}\omega_{LP}s + \omega_{LP}^2} = \frac{0.002^2}{s^2 + 1.9 \times 0.002s + 0.002^2} \quad (5\text{-}13)$$

The phase compensation between dither and demodulation is found as

$$\psi_{HTC} = \angle F_{O,HTC}(j\omega_{HTC}) + \angle F_{I,HTC}(j\omega_{HTC}) + \angle F_{LP\_COP}(j\omega) = -0.71 \text{ rad.} \quad (5\text{-}14)$$

The same procedure repeats for the LTC compressor and evaporator fan channel, respectively. The ESC design parameters are summarized in Table 5.6.

Table 5.6. ESC design parameters for COP maximization under variable heating capacity.

| Parameter | HTC Compressor | LTC Compressor | Evaporator Fan |
|---|---|---|---|
| Dither Frequency (rad/s) | 0.015 | 0.007 | 0.012 |
| Dither Amplitude (Hz) | 1.5 | 1.5 | 0.3 |
| Demodulation Amplitude (Hz) | 2/1.5 | 2/1.5 | 2/0.3 |
| Gain | 0.5 | 0.5 | 0.4 |
| $\omega_{BP}$ (rad/s) | 0.015 | 0.007 | 0.012 |
| $\omega_{LP}$ (rad/s) | 0.002 | 0.0015 | 0.0018 |
| $\varphi$ (rad) | –0.71 | –0.46 | –0.63 |
| $\xi_{BP}$ | 1.5 | 1.4 | 1.6 |
| $\xi_{LP}$ | 1.9 | 2 | 1.9 |

For the case of COP maximization under the variable heating capacity, three inner-loop controllers are implemented. i) The water outlet temperature is regulated to also 85 °C by the water pump mass flow rate via a PI controller. ii) The LTC superheat setpoint is regulated to the fixed setpoint 5 °C by the LTC expansion valve opening with another PI controller. iii) The HTC superheat setpoint is regulated to the fixed setpoint 8 °C by the HTC expansion valve with a PI controller. The specific design specifications of the three PI controllers are shown in Table 5.7.

Table 5.7. Design specifications of the PI controllers

| | Proportional Gain ($k$) | Integral Time ($T_i$) | Initial Output of PI Controller |
|---|---|---|---|
| LTC Superheat PI | $1x10^{-5}$ | 100 | $2.5x10^{-7}$ |
| HTC Superheat PI | $1x10^{-5}$ | 100 | $2.5x10^{-7}$ |
| Water outlet temperature PI | 0.07 | 10 | 3 |

### 5.4.2. Simulation study for COP maximization under variable heating capacity

The ESC designed in the previous subsection is then simulated for fixed condition and realistic condition. The SQP also is used as the benchmark to find the 'true' optimal value for the variable heat capacity case.

#### 5.4.2.1. Simulation under fixed ambient temperature

The ESC strategy is first evaluated under the fixed ambient temperature, with the basic settings same as that in Section 5.4.1. As shown in Figure 5.16, ESC is turned on at $t$ = 1 hour, with the HTC, LTC compressor frequency and evaporator air mass flow rate initialized as 50 Hz, 50 Hz and 7 kg/s, respectively. At steady state, the HTC compressor frequency increases to 72 Hz, the LTC compressor frequency decreases to 23.2 Hz, and the evaporator air mass flow rate decreases to 4.6kg/s, all converged to their respective optimum found by SQP. The water outlet temperature is well maintained at the 85°C setpoint.

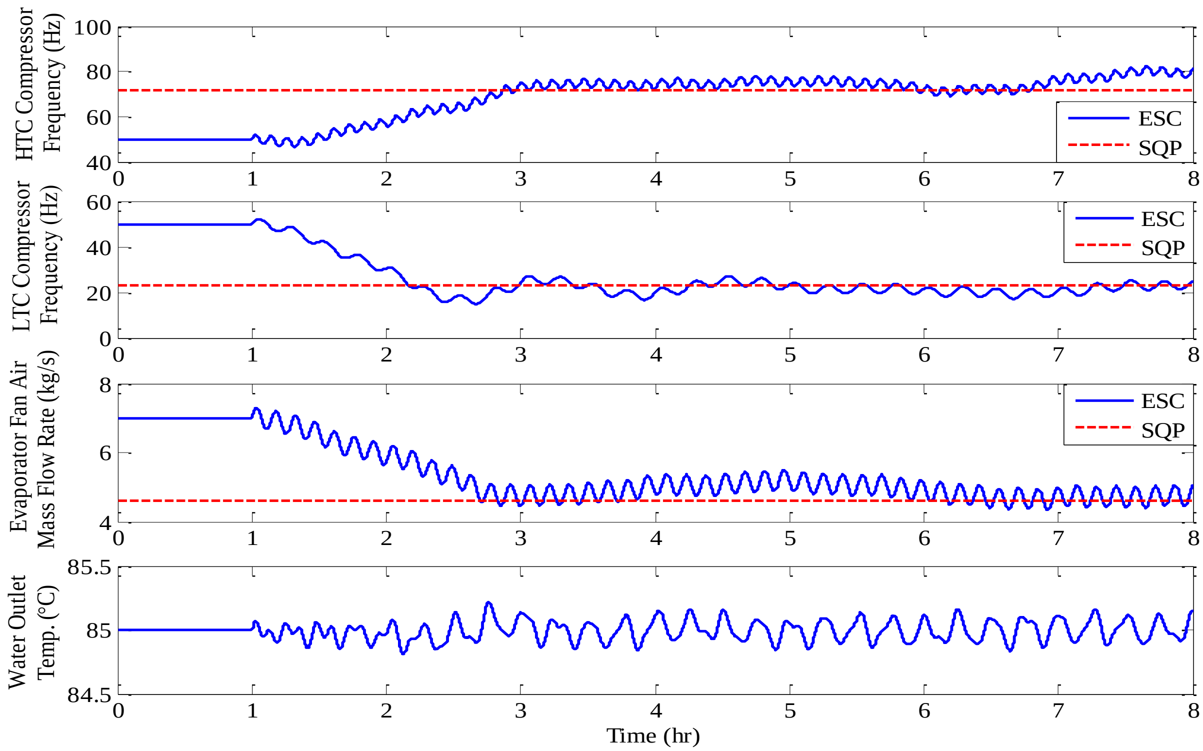


Figure 5.16. Trajectories of HTC and LTC compressor frequency, evaporator air mass flow rate, water outlet temperature for COP based ESC with under fixed ambient temperature.

As shown in Figure 5.17, the noise effect is clearly observed in the water mass flow rate, heating capacity and COP, and the COP demonstrates the largest fluctuation. In this simulation, the heating capacity and total power both decrease, while the total power decreases faster. the COP increases from the initial value of 1.98 to 2.15. Compared with the results for the fixed heating capacity case under the same ambient temperature, the COP is further improved with the flexibility of varying the heating capacity. In the fixed heating capacity case (see Figure 5.5), the COP is improved from 1.84 to 1.95 by applying the ESC strategy with power minimization; while in this case, the COP is improved up to 2.15 by ESC with COP maximization. In other words, the COP increases by 8.9% while the heating capacity decreases from 62.9 kW to 43.2 kW (i.e. by 31.3%).

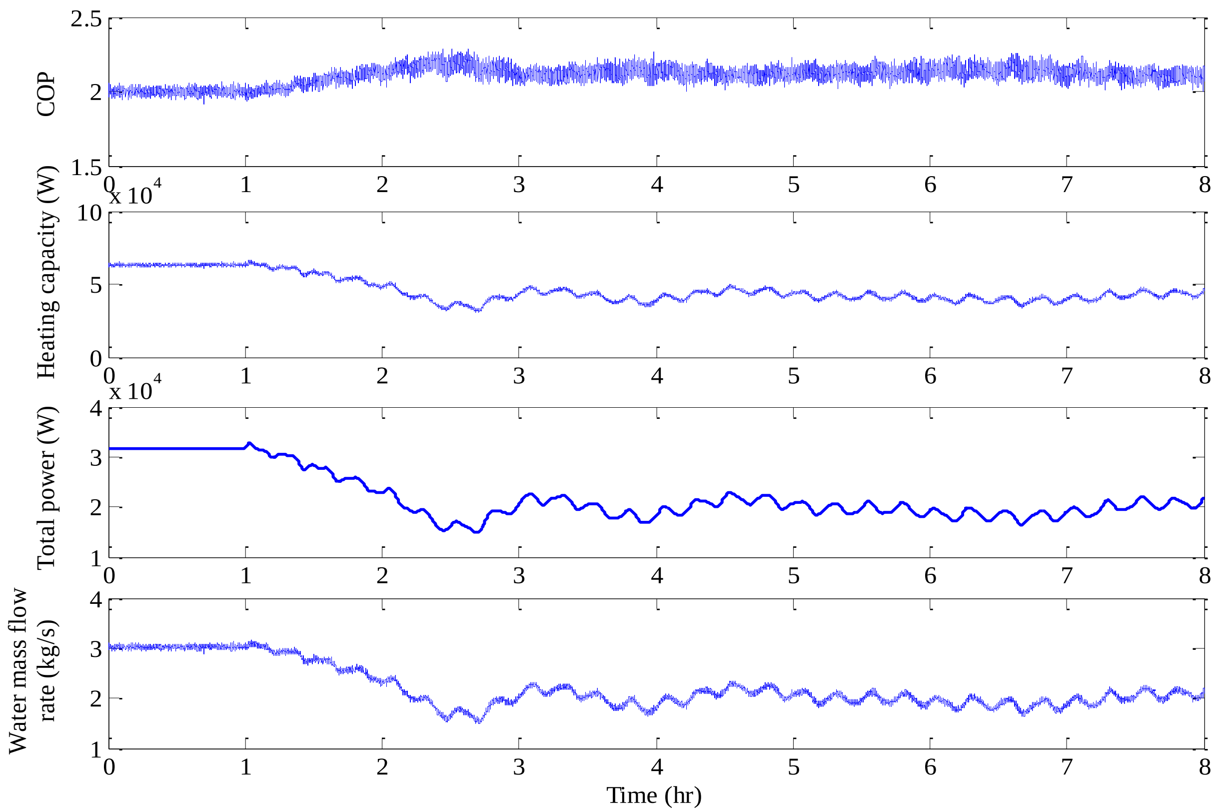


Figure 5.17. Trajectories of COP, heating capacity, total power and water mass flow rate for COP based ESC under fixed ambient temperature.

The gradients of three manipulated inputs are shown in Figure 5.18, which converge to the neighborhood of zero. Indeed, due to the noise effect, the gradients converge with moderate oscillations, which is acceptable.

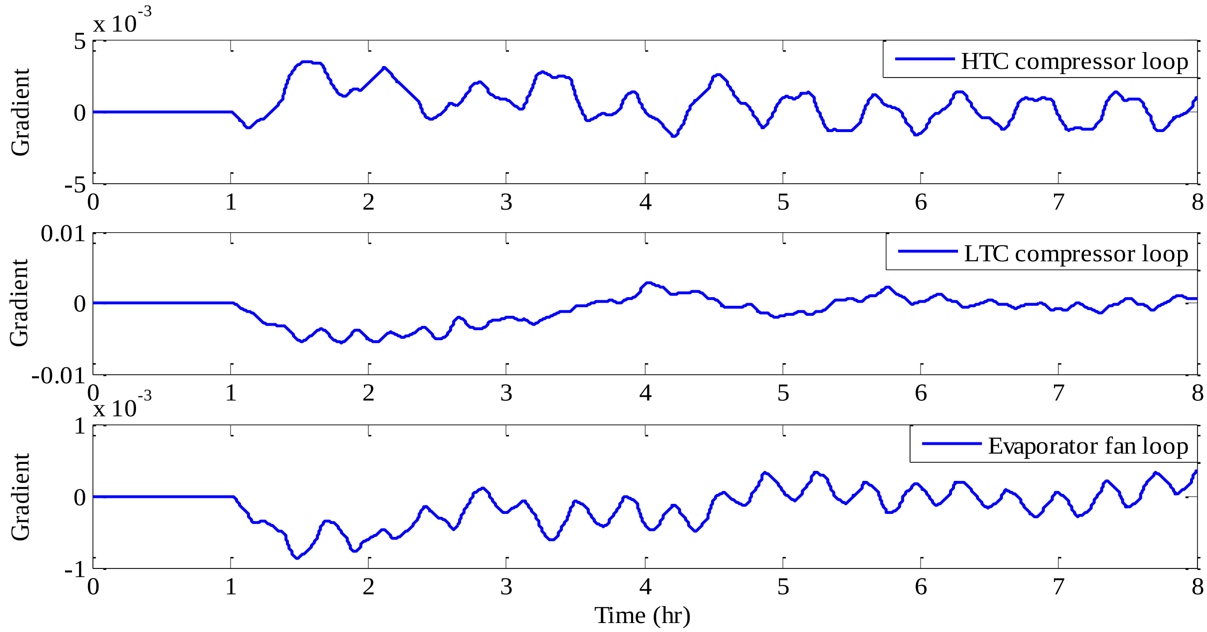


Figure 5.18. Trajectories of gradient for HTC, LTC compress and evaporator fan loo for COP based ESC under fixed ambient temperature.

### 5.4.2.2 Simulation under realistic condition

To evaluate the ESC strategy under a realistic condition, a 7-day ambient temperature profile is chosen from TMY3 for January 13$^{th}$ through 20$^{th}$ at the O'Hare Airport in Chicago. The temperature ranges from −13°C to 11°C, with most of temperature around or above 0°C. In this case, the proposed ESC strategy is benchmarked against the following control method: the HTC and LTC compressor speeds are both fixed at 50 Hz, the evaporator fan air mass flow rate is set as constant at 7 kg/s for all ambient temperate condition for the benchmark control strategy.

Figure 5.19 shows the trajectories of COP, heating capacity, total power and water mass flow rate. The average COP for ESC is 2.3 over the COP of 1.9 with the benchmark method, which implies a 21.1% improvement. However, the average heating capacity for ESC is 44,089 W compared to the 71,974 W with the benchmark method, which is a 38.7% decrease. That implies that a sacrifice of the heating capacity leads to the gain of COP. Therefore, with the COP based ESC control method, the heat pump can be operated with the maximum possible COP, although with an extended period to deliver the specific heating. By enhancing a heat pump (or CASHP) with a properly sized water tank, such control strategy can enable the optimum-COP operation.

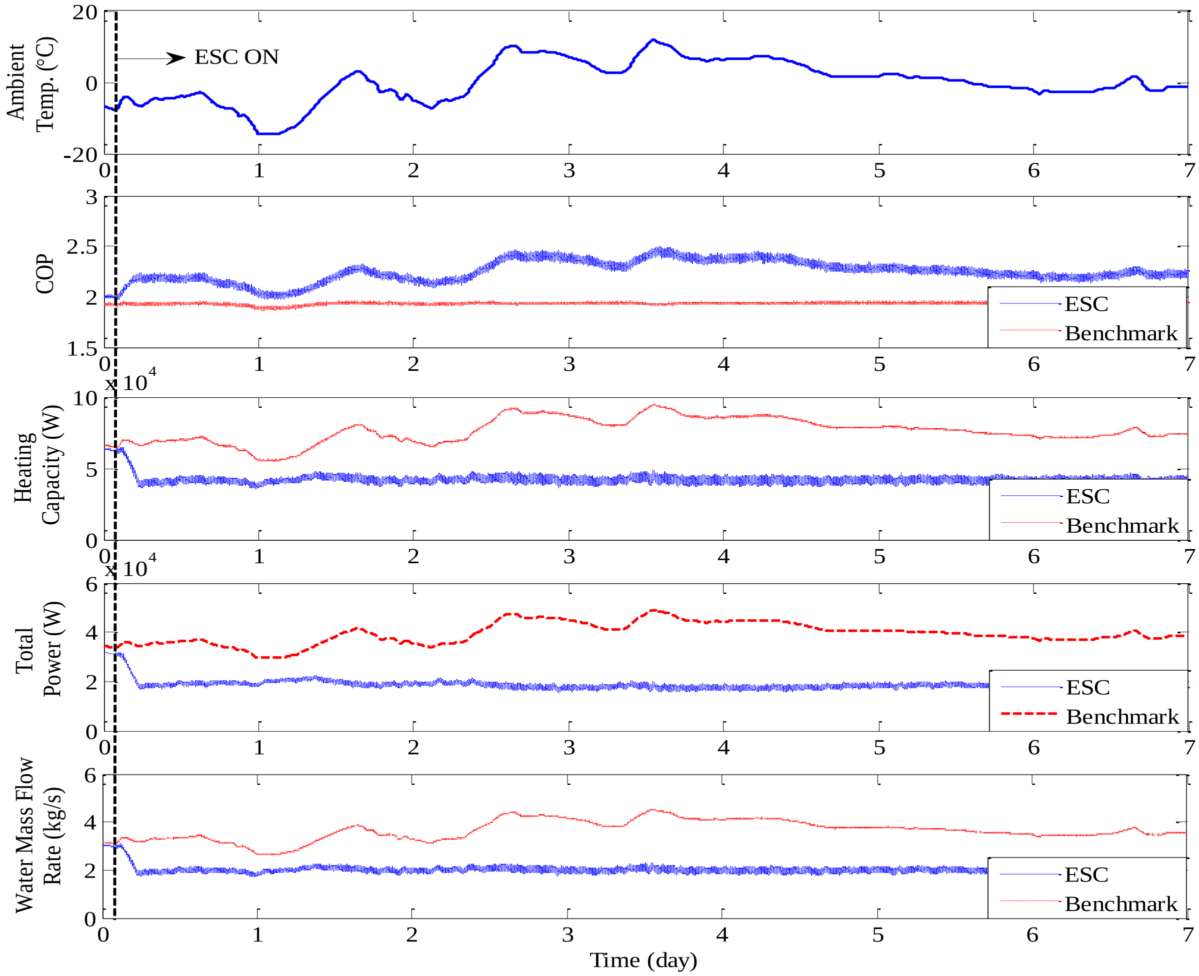


Figure 5.19. Trajectories of ambient temperature, COP, heating capacity, total power and water mass flow rate for ESC with variable heating capacity under realistic ambient temperature.

Figure 5.20 shows the results of HTC and LTC compressor frequencies, evaporator fan air mass flow rate and the water outlet temperature, with the ESC and benchmark method. For both cases, the water outlet temperature is well maintained. The gradient trajectories of the HTC, LTC

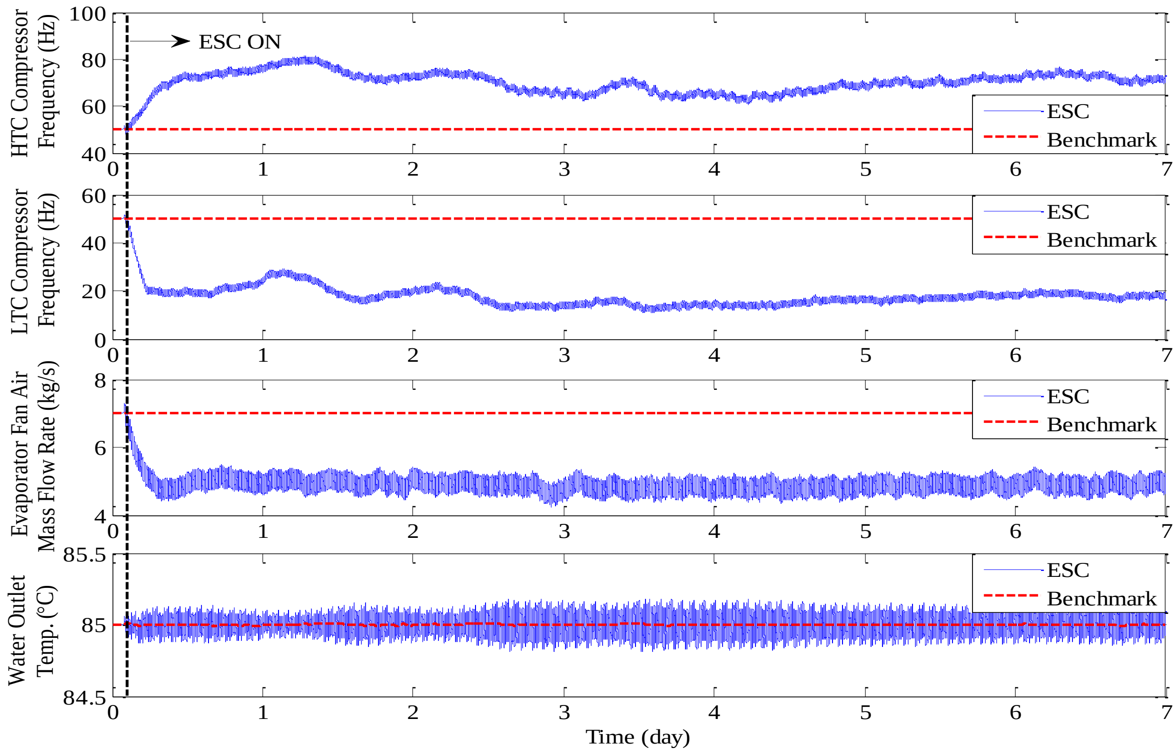


Figure 5.20. Trajectories of HTC, LTC compressor frequency, evaporator fan air mass flow rate, water outlet temperature for COP based ESC with under realistic ambient temperature.

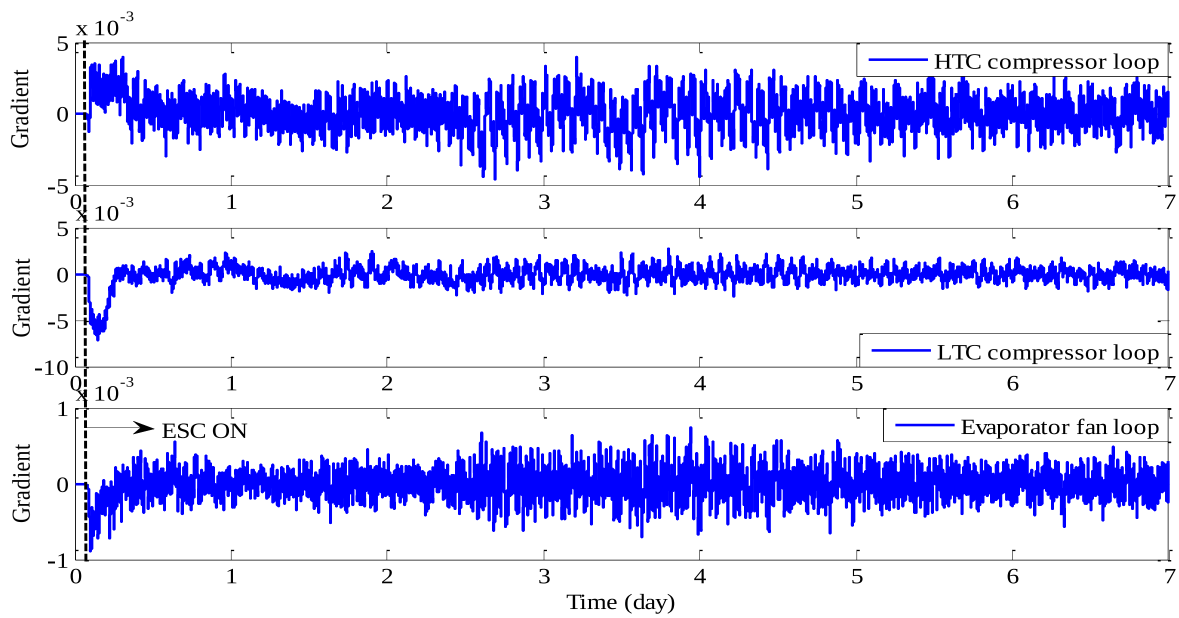


Figure 5.21. Trajectories of gradient for HTC, LTC compress and evaporator fan loop for COP based ESC under realistic ambient temperature.

compressor and the evaporator fan channels under the realistic ambient temperature profile are shown in Figure 5.21, which also converge to the neighborhood of zero with same moderate oscillations as the fixed ambient temperature case.

Furthermore, in order to evaluate capability of dynamic tracking of optimal COP in real time with the ESC, the results in Figure 5.19 are compared with the optimum COP trajectory found by the SQP method, as shown in Figure 5.22. The SQP procedure is applied for different ambient temperatures within the range being considered, with resolution of 0.1°C. The results reveal the capability of ESC in tracking the actual optimum COP in a realistic ambient temperature profile.

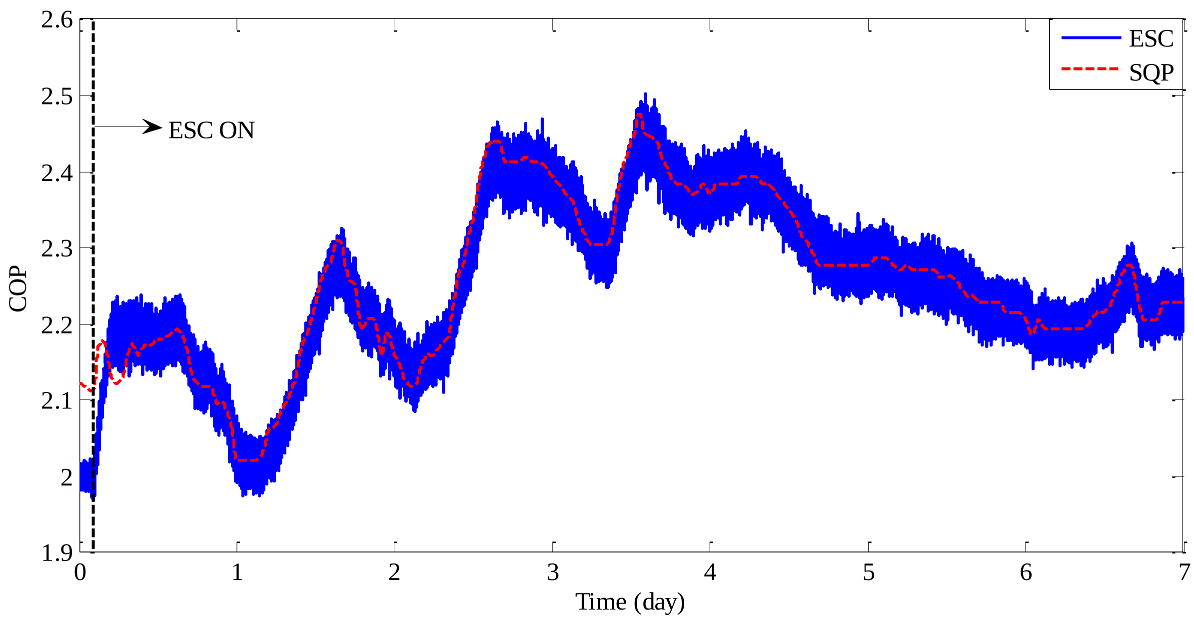


Figure 5.22. Comparison of COP trajectories found by ESC and SQP under the realistic ambient temperature profile for the variable heating capacity.

As Bertsch and Groll [10] indicated, cold-climate heat pumps typically have over-capacity for medium ambient temperatures, for which the actual optimal operation setting for off-design conditions can deviate significantly from that optimized for the low (design) ambient temperature.

The simulation results in this study shows that the ESC can successfully improve the efficiency of CASHP systems when operated under a mild ambient temperature condition.

### 5.5 Summary

In this chapter, the multivariable extremum seeking control is propose as a model-free real-time strategy for optimization of energy efficiency for the cascade heat pump. The scenarios of fixed and variable heating capacity are handled separately. For the fixed heating capacity case, the total power is used as the sole feedback, while the manipulated inputs of ESC include the intermediate temperature, the HTC and LTC superheat setpoints. For the variable heating capacity case, the system COP is used as the ESC feedback, while the HTC compressor speed, the LTC compressor speed and the evaporator fan air mass flow rate are the manipulated inputs. To validate the effectiveness of the proposed ESC strategies, a dynamic simulation model of a CASHP system is built in Modelica. Simulations are conducted under fixed and realistic ambient temperature profiles. The results show that the ESC strategies can converge the operation settings to the calibrated optimum well, with reasonably good transient performance. These results indicate that the system efficiency can be consistently optimized in a model-free and cost-effective fashion, which promises its great value for the practical operation of CASHP systems.

# CHAPTER 6

# CONCLUSIONS AND FUTURE RESEARCH

The contributions of this dissertation research are summarized in this chapter. Possibilities and directions are suggested for further research.

## 6.1 Conclusions and Research Contributions

Cold-climate heat pump systems present a unique control challenge, as such systems have their configurations evolved from the single-stage vapor compression cycle into various forms of multi-stage compression and cascaded-loop heat pumping, in order to achieve the overall compression ratio for meeting the unparalleled heating demand under the undesirable ambient condition. Maintaining the best possible energy efficiency of such systems can bring forth tremendous benefits in energy saving and emission reduction, which, however, is not easy to accomplish with model-based control/optimization techniques, mainly due to the complicated and coupled thermodynamic processes from the associate modifications introduced by the inherent designs.

This dissertation research has approached to this challenging problem with the Extremum Seeking Control as the model-free real-time optimization solution. Three dominant kinds of cold-climate ASHP systems have been used as illustrative examples: the IHXC vapor injection, the FTC vapor injection and a cascade heat pump system. In this dissertation, the standard ESC, Newton-based ESC and multivariable ESC are applied to the ASHP with IHXC, ASHP with FTC and cascade ASHP respectively to optimize their respective system performance. For evaluate the proposed control strategies for this proof-of-concept research, a great deal of efforts have been made to develop the Modelica based dynamic simulation models for these three systems so that simulations can be performed under various operating conditions.

First, a standard extremum seeking control framework is proposed as a model-free optimal control strategy for internal heat exchanger based VI-ASHP, minimizing the total power consumption in real time. The ESC takes the total power as the only feedback, and the intermediate pressure as the manipulated input. A Modelica-based dynamic simulation model of an IHXC-VI ASHP water heater is developed. The water outlet temperature is regulated by the compressor capacity, while the injection-loop expansion valve regulates the intermediate pressure. Under fixed, staircase and realistic ambient temperature profiles, simulation results show that ESC can optimize the intermediate pressure for system efficiency with good steady-state and transient performance.

Secondly, the Newton-based ESC is proposed for a two-stage air source heat pump water heater with flank-tank-cycle vapor injection. The intermediate pressure setpoint for the injection loop is regulated by the upper electronic expansion valve. Then, the ESC based real-time optimization framework adjusts the intermediate pressure setpoint to minimize the total power consumption, with the compressor capacity used to satisfy the load demand via an inner-loop controller. To evaluate the proposed control strategy, a Modelica based dynamic simulation model is developed for such system. Simulations under fixed, staircase and realistic ambient temperature profiles validate the effectiveness of the proposed control strategy. Besides real-time optimization of system efficiency, a major merit of this strategy is to retain the use of saturated vapor for the injection line, instead of levitating the superheat. The inherent efficiency of the flash tank cycle is thus maintained without additional devices, and the liquid level in the flash tank can be maintained in a proper range.

Finally, the multivariable extremum seeking control is proposed as a model-free strategy for real-time optimization of energy efficiency for the cascade heat pump water heater, with the effectiveness is well verified with a Modelica based model. The scenarios of fixed and variable heating capacity are handled separately. For the fixed heating capacity case, the total power is used as the sole feedback, while the manipulated inputs of ESC include the intermediate temperature, the HTC and LTC superheat setpoints. For the variable heating capacity case, the system COP is used as the ESC feedback, while the HTC compressor speed, the LTC compressor speed and the evaporator fan air mass flow rate are the manipulated inputs. The simulations results under fixed and realistic ambient temperature conditions indicate that the system efficiency can be consistently optimized in a model-free and cost-effective fashion, which promises its great value for the practical operation of the cascade heat pump water heaters.

## 6.2 Recommended Future Work

In this dissertation, different ESC algorithms have been applied to the three cold-climate ASHP systems for real-time efficiency optimization. The effectiveness has been validated by the simulation results based on the model built with Dymola and TIL library. In spite of the promising potential that has been demonstrated in the simulation studies, experimental validation has been missing for solid validation, which will be a certain next step.

In this dissertation, only the intermediate pressure is considered as a sole manipulated input for the VI-ASHP systems with IHXC and FTC. The main loop superheat and the evaporator fan speed can also be considered as other manipulated inputs for optimizing the system. In addition, for obtaining the highest system performance, the COP feedback can be considered with the multivariable inputs of main loop superheat, evaporator fan speed and the water pump mass flow rate.

The ESC based COP optimization for CASHP implies the use of slower flow rate of condensing water to trade for higher efficiency, which would be feasible by adding a water tank. Towards deployment, the overall economic analysis will be a critical step to justify the overall benefit. To a broader sense, such scenario is applicable for other types of heat pump systems.

# APPENDIX A

## MATHEMATICAL MODELING FOR SCROLL COMPRESSORS

In this dissertation, the scroll compressors are used in the different ASHP configurations, which are modeled with the *TIL.VLEFluidComponents.Compressors.ScrollCompressor* module in the TIL Library. Figure A.1 shows a schematic of the scroll compressor model construction [15].

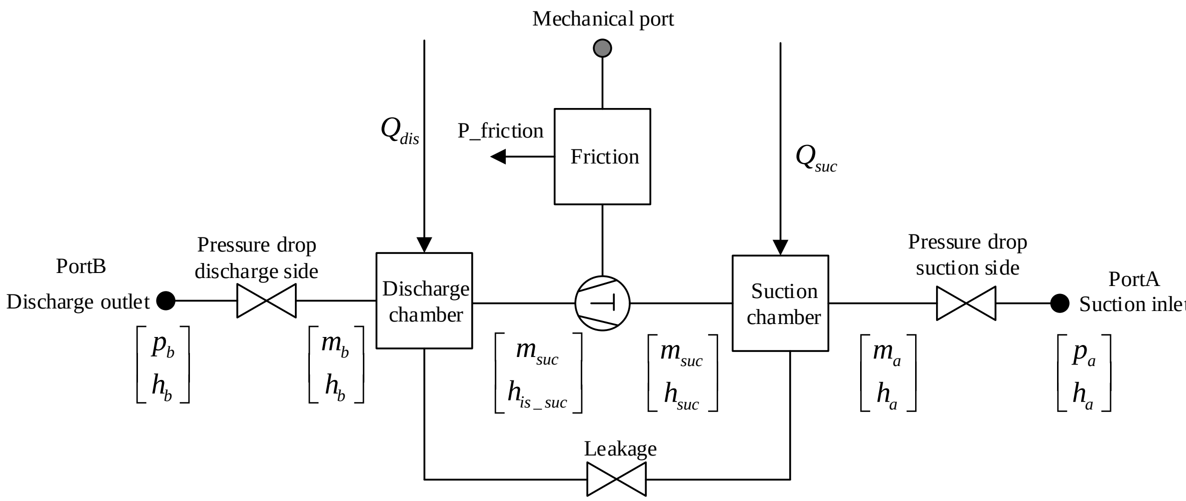


Figure A.1. Schematic of the scroll compressor model composition [15].

The dynamic modeling of the scroll compressor mainly involves the mass and energy balances in the suction chamber, discharge chamber, respectively. In addition, the refrigerant mass flow rate is calculated with the Saint Venant Wantzel formula. The compression stages are treated as a process of isentropic compression with the friction effect included. Pressure $p$ and enthalph $h$ are selected as the state variables in the model. First, the time derivative of density in the continuity equation can be expanded as follows:

$$\frac{d\rho}{dt} = \left.\frac{\partial \rho}{\partial h}\right|_p \frac{dh}{dt} + \left.\frac{\partial \rho}{\partial p}\right|_h \frac{dp}{dt} \tag{A-1}$$

where $\rho$ denotes the density, $h$ denotes the enthalpy, and $t$ denotes the time. The subscript 'p' refers to the pressure. Then, the transient mass and energy balances for the refrigerant inside the suction chamber can be established as

$$\frac{d\rho_{suc}}{dt}V_{suc} = \dot{m}_a - \dot{m}_{suc} \tag{A-2a}$$

$$\frac{dh_{suc}}{dt} = \frac{1}{V_{suc}\rho_{suc}}\left[\dot{m}_a\left(h_a - h_{suc}\right) + V_{suc}\frac{dp_{suc}}{dt}\right] \tag{A-2b}$$

where $V$ refers to the volume, $\dot{m}$ refers to the mass flow rate. The subscript 'suc' stand for the suction chamber, and 'a' stand for the suction inlet port. Similarly, the mass and energy balances of the refrigerant in the discharge chamber can be described as

$$\frac{d\rho_{dis}}{dt}V_{dis} = \dot{m}_{suc} - \dot{m}_b \tag{A-3a}$$

$$\frac{dh_{dis}}{dt} = \frac{1}{V_{dis}\rho_{dis}}\left[\dot{m}_{suc}\left(h_{is\_dis} - h_b\right) + V_{dis}\frac{dp_{dis}}{dt}\right] \tag{A-3b}$$

where subscripts '*dis*', '*b*' and '*is*' stand for the discharge chamber, the discharge outlet port, and isentropic, respectively. The refrigerant mass flow rate for the suction side and the discharge side is both calculated with the Saint Venant Wantzel fomula:

$$\dot{m}_a = A_{suc}\sqrt{2p_a\rho_a\frac{k}{k-1}\left[\left(\frac{p_{suc}}{p_a}\right)^{\frac{2}{k}} - \left(\frac{p_{suc}}{p_a}\right)^{\frac{k+1}{k}}\right]} \tag{A-4a}$$

$$\dot{m}_b = A_{dis}\sqrt{2p_{dis}\rho_{is\_dis}\frac{k}{k-1}\left[\left(\frac{p_b}{p_{dis}}\right)^{\frac{2}{k}} - \left(\frac{p_b}{p_{dis}}\right)^{\frac{k+1}{k}}\right]} \tag{A-4b}$$

where $p_{suc} = p_a - \Delta p_{suc}$ and $p_{dis} = p_b + \Delta p_{dis}$. $A$ refers to the area, and $k$ refers to the adiabatic exponent. Finally, the total power consists of the enthalpy rate for the two isentropic compression processes and power loss due to friction, i.e.

$$P_{total} = \dot{m}_{suc}(h_{is\_suc} - h_{suc}) + P_{fic} \quad \text{(A-5)}$$

where $P$ refers to the power consumption. Subscripts '*total*' and '*fic*' stand for the total and fiction power consumption, respectively.

## APPENDIX B

## MATHEMATICAL MODELING FOR HEAT EXCHANGERS

The heat exchanger (*TIL.HeatExchangers.HeatExchangersGuide*) is a major component used for the modeling in this dissertation. The tube-and-tube heat exchanger is used as a condenser for transfering heat between the refrigerent and water, while the fin-and-tube heat exchanger is used as a evaporator for transferring heat between the refrigerent and the ambient air. Figure B.1 shows a tube-and-tube heat exchagner model, which is discretied into many cells. The heat tranfer process is calculated in each cell. Every heat transfer cell consists of VLEFluid cell, Wall cell and Liquid cell, the VLEFluid cell refers to the refrigerant side and the Liquid cell refers to the water side [15].

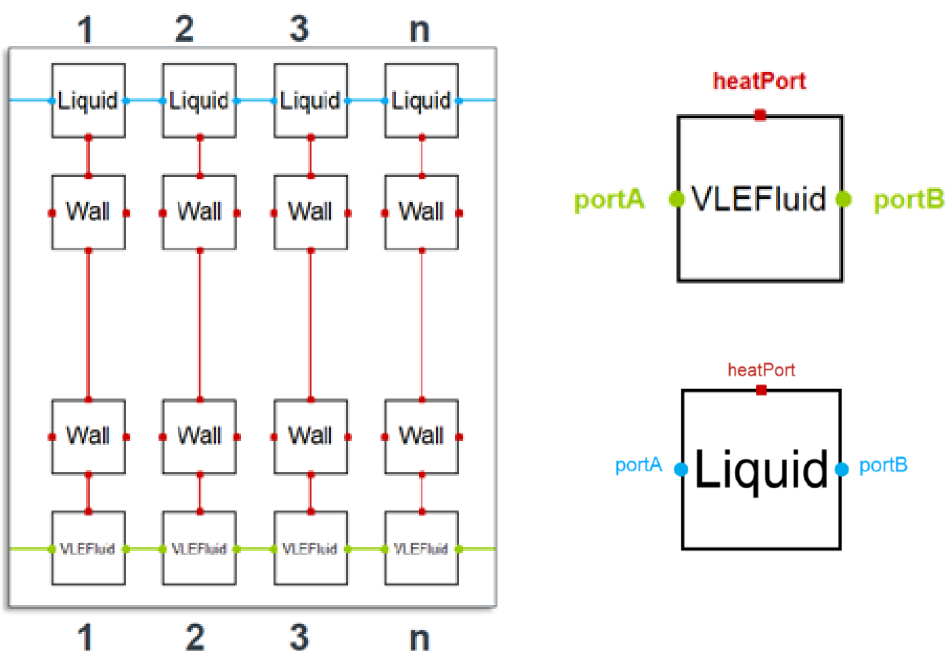


Figure B.1. The tube and tube heat exchanger model [15].

For the VLEFluid cell, the energy balance, continuity equation and momentum euqation is used to calculate the heat transfer process.

$$\frac{dh}{dt}=\frac{1}{M}[\dot{m}_A \bullet (h_A-h)+\dot{m}_B \bullet (h_B-h)+\dot{Q}+V \bullet \frac{dp}{dt}] \tag{B-1}$$

$$\frac{d\rho}{dt} \bullet V=\dot{m}_A+\dot{m}_B \tag{B-2}$$

$$p_A-p_B=\triangle p_{friction} \tag{B-3}$$

where Eqs. (B-1), (B-2) and (B-3) reflect the energy, the mass and the momentum conservations, respectively. $h$ refers to the enthlpy, $\dot{m}$ refers to the mass flow rate, $V$ , $p$ , and $M$ refers to the volume, pressure and mass, respectively. $\dot{Q}$ refers to the heat exchanged between the different fluid. Subscripts 'A' and 'B' refer to the port A and port B, respectively, in Figure B.1. Subscript 'friction' stands for the pressure loss due to the friciton.

The mass of referigerant in each cell is calculated by $M=V \bullet \rho$, but the density $\rho$ is a time-variable in the each cell calculaiton. For cell $i$, it can be calculated as:

$$\frac{d\rho(h,p,x_i)}{dt}=(\frac{\partial\rho}{\partial h})_{p,x_i}\frac{dh}{dt}+(\frac{\partial\rho}{\partial p})_{h,x_i}\frac{dp}{dt}+(\frac{\partial\rho}{\partial x_i})_{h,p}\frac{dx_i}{dt} \tag{B-4}$$

where the $x_i$ stands for the mass mass fraction of the refrigerant compoennt for the refrigerant which is made of several components. For the refrigernat made of pure substance, this can be ignored.

For the liqid cell, also the energy balance equation, continuity equation and momentum equation is used, and the density $\rho$ is also a time-variable.

$$c_p\frac{dT}{dt}=\frac{1}{M}[\dot{m}_A \bullet (h_A-h)+\dot{m}_B \bullet (h_B-h)+\dot{Q}] \tag{B-5}$$

$$\dot{m}_A + \dot{m}_B = V \bullet \frac{d\rho(T,p)}{dt} = -V \bullet \rho \bullet \beta \bullet \frac{dT}{dt} \tag{B-6a}$$

$$\beta = -\frac{1}{\rho}\left(\frac{\partial \rho}{\partial T}\right)_p \tag{B-6b}$$

$$p_A - p_B = \triangle p_{friction} \tag{B-7}$$

$$\frac{d\rho(T,p)}{dt} = \left(\frac{\partial \rho}{\partial T}\right)_p \frac{dT}{dt} + \left(\frac{\partial \rho}{\partial p}\right)_T \frac{dp}{dt} \tag{B-8}$$

$$M = V \bullet \rho \tag{B-9}$$

Again, Eqs. (B-5), (B-6) and (B-7) are the energy, mass and momentum balances, respectively. $c_p$ refers to the specific heat capacity, $T$ refers to temperature, and $\beta$ is the isobaric expansion coefficient.

Then the Newton cooling law $\dot{Q} = \alpha A \triangle T(t)$ is used to calculate the heat flow rate between the refrigerent side and the water side, where $\alpha$ is the heat transfer coefficient. The heat transfer between the two wall cells is the heat conduciton process across the cylinder. The thermal resistance bwteen the walls can be calculated with $R = \frac{\ln\left(R_2/R_1\right)}{2 \bullet \pi \bullet \lambda \bullet L}$, where $R_1$ and $R_2$ refer to the inner and outer diameter of the tube, respectively. $\lambda$ is the thermal conductivity, and $L$ is the tube length.

For the fin-and-tube heat exchanger used as the evaporator, the basic idea is the same as the above tube-and-tube heat exchanger, but the Liquid cell is replaced with the Gas cell. In the Gas cell, the energy balance, continuity equation, component mass balance, and momentum equation are established as:

$$\dot{m}_A \bullet h_A + \dot{m}_B \bullet (h_B - h) - \dot{Q}_{wall} + h_{Film} \bullet (\dot{m}_{evap} - \dot{m}_{cond}) = 0 \tag{B-10}$$

$$\dot{m}_A + \dot{m}_B - \dot{m}_{cond} + \dot{m}_{evap} = 0 \tag{B-11}$$

$$\dot{m}_A \bullet x_{air} + \dot{m}_B \bullet x_{air} = 0 \tag{B-12a}$$

$$\dot{m}_A \bullet x_{h2o} + \dot{m}_B \bullet x_{h2o} - \dot{m}_{cond} + \dot{m}_{evap} = 0 \tag{B-12b}$$

$$p_A - p_B = \triangle p_{friction} \tag{B-13}$$

Eq. (B-10) is the energy balance equation, Eq. (B-11) is the continuity equation, Eq. (B-12) is component mass balance equation, and Eq. (B-13) is the momentum equation. Subscripts 'Film' , 'evap' and 'cond' refer to the liquid film, evaporating water and the condense ring water, respectively. $x_{air}$ and $x_{h2o}$ refer to the dry-air and water proportions in the moist air, respectively.

## APPENDIX C

## MATHEMATICAL MODELING FOR OTHER COMPONENTS

The orifice valve module (*TIL.LiquidComponents.Valves.OrificeValve*) in the TIL library [15] is used to modeling the expansion valve. It can calculates the mass flow rate in dependency of the pressure drop using the equation of Bernoulli as follows.

$$\dot{m}_{ref} = A_{eff} * \sqrt{(p_{in} - p_{out}) * 2\rho_{in}} \tag{C-1}$$

where the $A_{eff}$ refers to the effective flow area. $p$ and $\rho$ denote the pressure and the density, respectively. Subscripts '*in*' and '*out*' refer to the inlet and the outlet of the valve, respectively.

A simple pump module in the TIL Library (*TIL.LiquidComponents.Pumps.SimplePump*) is used to model the water pump component [15]. In order to simulate the energy input into the liquid flow, the shaft power of the pump is calculated and entirely added to the energy balance of the medium. For the calculation of the shaft power, the pump efficiency $\eta$ is needed. Generally speaking, such efficiency ranges from 0.05 to 0.80 [15]. In this dissertation, the pump efficiency for every model is chosen as 0.8.

$$P_{hyd} = dp \bullet V_{flow} \tag{C-2}$$

$$P_{loss} = \eta_{drive} \bullet P_{drive} \bullet (1-\eta) \tag{C-3}$$

$$P_{drive} = \left(\frac{1}{\eta}\right)\left(\frac{1}{\eta_{drive}}\right) P_{hyd} \tag{C-4}$$

where $P$, $p$ and $V_{flow}$ refer to the power consumption, pressure and volume flow rate, respectively. Subscripts '*hyd*', '*loss*' and '*drive*' refer to the hydraulic power transmitted to the medium, the power losses during fluid acceleration, and the required power input of the pump, respectively.

A simple fan module (*TIL.GasComponents.Fans.SimpleFan*) is used to model the evaporator fan in the simulation [15]. In order to simulate the energy input into the gas flow, the shaft power of the fan is calculated and entirely added to the energy balance of the gas. Generally speaking, the fan efficiency $\eta$ range from 0.3 to 0.6. In this dissertation study, the fan efficiency for every model is chosen as 0.6. In addition, a drive efficiency $\eta_{drive}$ is needed in order to calculate the drive power, typically the drive efficiency is higher than 0.8. In this dissertation, the drive efficiency is set as 1 for all models.

$$P_{hyd} = dp \bullet V_{flow} \tag{C-5}$$

$$P_{shaft} = \frac{1}{\eta} P_{hyd} \tag{C-6}$$

$$P_{drive} = \frac{P_{hyd}}{\eta \bullet \eta_{drive}} \tag{C-7}$$

where $P$ , $p$ and $V_{flow}$ refer to the power consumption, pressure and volume flow rate, respectively.

# REFERENCES

[1] U.S. Energy Information Administration, *Residential Energy Consumption Survey 2015*. <https://www.eia.gov/todayinenergy/detail.php?id=37433#>.

[2] IEA Industrial Energy-related Systems and Technologies, *Application of Industrial Heat Pumps: IEA Industrial Energy-related Systems and Technologies Annex 13 & IEA Heat Pump Programme Annex 35*, Final Report, Part 1, 2014. <https://iea-industry.org/app/uploads/annex-xiii-part-a.pdf>.

[3] Chua, K.J., Chou, S.K. and Yang, W.M., 2010. Advances in heat pump systems: A review. Applied Energy, 87(12), pp. 3611-3624.

[4] Department of Energy, Air Source Heat Pumps 2018. <https://www.energy.gov/energysaver/heat-pump-systems/air-source-heat-pumps>.

[5] Mengjie, S., Ning, M., Yingjie, X. and Shiming, D., 2019. Challenges in, and the development of, building energy saving techniques, illustrated with the example of an air source heat pump. Thermal Science and Engineering Progress, 31, pp. 337-356.

[6] U.S. Energy Information Administration, What's New in How We Use Energy at Home, Analysis and Projections 2018. <https://www.eia.gov/consumption/residential/reports/2015/overview/index.php?src=%E2%80%B9%20Consumption%20%20%20%20%20Residential%20Energy%20Consumption%20Survey%20(RECS)-f3>.

[7] Graphical Research, *Europe Air Source Heat Pump Market Size by Product 2018*. <https://www.graphicalresearch.com/industry-insights/1025/europe-air-source-heat-pump-market>.

[8] China Heat Pump Industry Alliance, *China air source heat pump market development 2016*. <https://hpc2017.org/wp-content/uploads/2017/06/o211.pdf>.

[9] Shen, H., 2015. Cold Regions Science and Marine Technology. Eolss Publishers Company Limited.

[10] Bertsch, S.S. and Groll, E.A., 2008. Two-stage air-source heat pump for residential heating and cooling applications in northern US climates. International Journal of Refrigeration, 31(7), pp. 1282-1292.

[11] Park, C., Lee, H., Hwang, Y. and Radermacher, R., 2015. Recent advances in vapor compression cycle technologies. International Journal of Refrigeration, 60, pp. 118-134.

[12] Arpagaus, C., Bless, F., Schiffmann, J. and Bertsch, S.S., 2016. Multi-temperature heat pumps: A literature review. International Journal of Refrigeration, 69, pp. 437-465.
[13] Dassault Systems, Dymola: Multi-Engineering Modeling and Simulation based on Modelica and FMI, 2017. <https://www.3ds.com/products-services/catia/products/dymola>.

[14] Richter, C.C., 2008. Proposal of New Object-Oriented Model Libraries for Thermodynamic Systems. Ph. D. Thesis, Technical University at Braunschweig.

[15] TLK-Thermo GmbH. TIL3.4.2 - Engineering Services and Software for Thermal Systems, 2017. <http://www.tlk-thermo.com/index.php>.

[16] Xu, X., Hwang, Y. and Radermacher, R., 2011. Refrigerant injection for heat pumping/air conditioning systems: literature review and challenges discussions. International Journal of Refrigeration, 34(2), pp. 402-415.

[17] Wang, X., 2008. Performance investigation of two-stage heat pump system with vapor-injected scroll compressor. Ph.D. dissertation, Department of Mechanical Engineering at University of Maryland, College Park.

[18] Ma, G.Y. and Zhao, H.X., 2008. Experimental study of a heat pump system with flash-tank coupled with scroll compressor. Energy and Buildings, 40(5), pp. 697-701.

[19] Park, H., Kim, D.H. and Kim, M.S., 2013. Thermodynamic analysis of optimal intermediate temperatures in R134a–R410A cascade refrigeration systems and its experimental verification. Applied Thermal Engineering, 54(1), pp.319-327.

[20] Bhattacharyya, S., Mukhopadhyay, S. and Sarkar, J., 2008. CO2–C3H8 cascade refrigeration–heat pump system: heat exchanger inventory optimization and its numerical verification. International Journal of Refrigeration, 31(7), pp. 1207-1213.

[21] Wu, J., Yang, Z., Wu, Q. and Zhu, Y., 2012. Transient behavior and dynamic performance of cascade heat pump water heater with thermal storage system. Applied Energy, 91(1), pp. 187-196.

[22] Roh, C.W. and Kim, M.S., 2014. Effect of vapor-injection technique on the performance of a cascade heat pump water heater. International Journal of Refrigeration, 38, pp. 168-177.

[23] Kim, D.H., Park, H.S. and Kim, M.S., 2014. The effect of the refrigerant charge amount on single and cascade cycle heat pump systems. International Journal of Refrigeration, 40, pp. 254-268.

[24] Chae, J.H. and Choi, J.M., 2015. Evaluation of the impacts of high stage refrigerant charge on cascade heat pump performance. Renewable energy, 79, pp. 66-71.

[25] Song, Y., Li, D., Yang, D., Jin, L., Cao, F. and Wang, X., 2017. Performance comparison between the combined R134a/CO2 heat pump and cascade R134a/CO2 heat pump for space heating. International Journal of Refrigeration, 74, pp. 592-605.

[26] Song, Y., Li, D., Cao, F. and Wang, X., 2017. Theoretical investigation on the combined and cascade CO2/R134a heat pump systems for space heating. Applied Thermal Engineering, 124, pp. 1457-1470.

[27] Song, Y., Li, M. and Cao, F., 2018. Review on development of air source transcritical CO2 heat pump systems using direct-heated type and recirculating-heated type. International Journal of Refrigeration, 104, pp. 455-475.

[28] Shen, J., Guo, T., Tian, Y. and Xing, Z., 2018. Design and experimental study of an air source heat pump for drying with dual modes of single stage and cascade cycle. Applied Thermal Engineering, 129, pp. 280-289.

[29] Fine, J.P., Friedman, J. and Dworkin, S.B., 2017. Detailed modeling of a novel photovoltaic thermal cascade heat pump domestic water heating system. Renewable Energy, 101, pp.500-513.

[30] Li, Y., Wang, W., Ma, Y. and Li, W., 2018. Study of new cascade heating system with multi-heat sources based on exhausted steam waste heat utilization in power plant. Applied Thermal Engineering, 136, pp.475-483.

[31] Lv, X., Yan, G. and Yu, J., 2015. Solar-assisted auto-cascade heat pump cycle with zeotropic mixture R32/R290 for small water heaters. Renewable Energy, 76, pp. 167-172.

[32] Umezu, K. and Suma, S., 1984. Heat pump room air-conditioner using variable capacity compressor. ASHRAE Transactions, 90(1A), pp. 335-349.

[33] Winandy, E.L. and Lebrun, J., 2002. Scroll compressors using gas and liquid injection: experimental analysis and modelling. International Journal of Refrigeration, 25(8), pp. 1143-1156.

[34] Cho, I.Y., Ko, S.B. and Kim, Y., 2012. Optimization of injection holes in symmetric and asymmetric scroll compressors with vapor injection. International Journal of Refrigeration, 35(4), pp.850-860.

[35] Navarro, E., Redón, A., Gonzálvez-Macia, J., Martinez-Galvan, I.O. and Corberán, J.M., 2013. Characterization of a vapor injection scroll compressor as a function of low, intermediate and high pressures and temperature conditions. International Journal of Refrigeration, 36(7), pp. 1821-1829.

[36] Roh, C.W. and Kim, M.S., 2012. Comparison of the heating performance of an inverter-driven heat pump system using R410A vapor-injection into accumulator and compressor. International Journal of Refrigeration, 35(2), pp. 434-444.

[37] Oquendo, F.M.T., Peris, E.N., Macia, J.G. and Corberán, J.M., 2016. Performance of a scroll compressor with vapor-injection and two-stage reciprocating compressor operating under extreme conditions. International Journal of Refrigeration, 63, pp. 144-156.

[38] Guoyuan, M., Qinhu, C. and Yi, J., 2003. Experimental investigation of air-source heat pump for cold regions. International Journal of Refrigeration, 26(1), pp. 12-18.

[39] Ma, G.Y. and Chai, Q.H., 2004. Characteristics of an improved heat-pump cycle for cold regions. Applied Energy, 77(3), pp. 235-247.

[40] Tian, C., Liang, N., Shi, W. and Li, X., 2006. Development and experimental investigation on two-stage compression variable frequency air source heat pump. In Proceedings of International Refrigeration and Air Conditioning Conference at Purdue, West Lafayette, p. R040.

[41] Roh, C.W. and Kim, M.S., 2011. Effects of intermediate pressure on the heating performance of a heat pump system using R410A vapor-injection technique. International Journal of Refrigeration, 34(8), pp.1911-1921.

[42] Feng, C., Kai, W., Shouguo, W., Ziwen, X. and Pengcheng, S., 2009. Investigation of the heat pump water heater using economizer vapor injection system and mixture of R22/R600a. International Journal of Refrigeration, 32(3), pp. 509-514.

[43] Joppolo, C.M., Vecchi, G., Bianchi, C., Magni, F. and Winandy, E., 2010. Performance assessment of an air-to-water R-407C heat pump with vapor injection scroll compressor. ASHRAE Transactions, 116, pp. 310-317.

[44] Hwang, Y.H., Celik, A. and Radermacher, R., 2004. Performance of CO2 cycles with a two-stage compressor. In Proceedings of International Refrigeration and Air Conditioning Conference at Purdue, West Lafayette, p. R105.

[45] Hickman, C. and Neal, W.E.J., 1984. Implications of cooling rotary sliding vane heat-pump compressors. International Journal of Ambient Energy, 5(4), pp. 207-212.

[46] Shcherba, V.E., Berezin, I.S. and Danilenko, S.S., 1987. Efficient injection of cooling liquid into a rotary compressor with a rolling rotor. Chemical and Petroleum Engineering, 23(12), pp. 606-610.

[47] Berezin, I.S., 1987. Effect of the method of a liquid coolant on the productivity and efficiency of a compressor. Khimicheskoe I neftyanoe Mashinostroenie, 5, pp. 18-19.

[48] Liu, F., Ma, Y. and Zhuang, R., 2008. An experimental study on the heat pump water heater system with refrigerant injection. In Proceedings of International Refrigeration and Air Conditioning Conference at Purdue, West Lafayette, p. 2211.

[49] Baek, C., Lee, E., Kang, H. and Kim, Y., 2008. Experimental study on the heating performance of a CO2 heat pump with gas injection. In Proceedings of International Refrigeration and Air Conditioning Conference at Purdue, West Lafayette, p. 2250.

[50] Cavallini, A., Cecchinato, L., Corradi, M., Fornasieri, E. and Zilio, C., 2005. Two-stage transcritical carbon dioxide cycle optimisation: A theoretical and experimental analysis. International Journal of Refrigeration, 28(8), pp.1274-1283.

[51] Liu, Z. and Soedel, W., 1994. An investigation of compressor slugging problems. In Proceedings of International Compressor Engineering Conference at Purdue, West Lafayette, pp. 433-440.

[52] Liu, Z. and Soedel, W., 1995. A mathematical model for simulating liquid and vapor two-phase compression processes and investigating slugging problems in compressors. HVAC&R Research, 1(2), pp.99-109.

[53] Ishii, H., Matsuda, M. and Sanuki, M., Denso Corp and Soken Inc, 1998. Compressor having refrigerant injection ports. U.S. Patent 5,722,257.

[54] Cho, H., Chung, J.T. and Kim, Y., 2003. Influence of liquid refrigerant injection on the performance of an inverter-driven scroll compressor. International Journal of Refrigeration, 26(1), pp. 87-94.

[55] Dutta, A.K., Yanagisawa, T. and Fukuta, M., 2001. An investigation of the performance of a scroll compressor under liquid refrigerant injection. International Journal of Refrigeration, 24(6), pp. 577-587.

[56] Schein, C. and Radermacher, R., 2001. Scroll compressor simulation model. Journal of Engineering for Gas Turbines and Power, 123(1), pp.217-225.

[57] Skinner, R.G., Tecumseh Products Co, 2008. Scroll compressor with refrigerant injection system. U.S. Patent, No. 0184733A1.

[58] He, S., Guo, W. and Wai, E.W., 2006. Northern china heat pump application with the digital heating scroll compressor. In Proceedings of International Refrigeration and Air Conditioning Conference at Purdue, West Lafayette, p. R116.

[59] Chen, Y., Halm, N.P., Groll, E.A. and Braun, J.E., 2002. Mathematical modeling of scroll compressors—part I: compression process modeling. International Journal of Refrigeration, 25(6), pp. 731-750.

[60] Chen, Y., Halm, N.P., Braun, J.E. and Groll, E.A., 2002. Mathematical modeling of scroll compressors—part II: overall scroll compressor modeling. International Journal of Refrigeration, 25(6), pp. 751-764.

[61] Wang, B., Li, X., Shi, W. and Yan, Q., 2007. Design of experimental bench and internal pressure measurement of scroll compressor with refrigerant injection. International Journal of Refrigeration, 30(1), pp. 179-186.

[62] Wang, B., Shi, W., Li, X. and Yan, Q., 2008. Numerical research on the scroll compressor with refrigeration injection. Applied Thermal Engineering, 28(5-6), pp.440-449.

[63] Tello-Oquendo, F.M., Navarro-Peris, E. and Gonzálvez-Maciá, J., 2017. New characterization methodology for vapor-injection scroll compressors. International Journal of Refrigeration, 74, pp. 528-539.

[64] Leimbach, J.G. and Heffner, J.H., 1992. Injection Valve for A Refrigeration System, U.S. Patent, No. 5148684.

[65] Lifson, A. and Taras, M.F., Carrier Corp, 2008. Economized Refrigerant System with Vapor Injection at Low Pressure. U.S. Patent, No. 0256961A1.

[66] Wang, X., Hwang, Y. and Radermacher, R., 2009. Two-stage heat pump system with vapor-injected scroll compressor using R410A as a refrigerant. International Journal of Refrigeration, 32(6), pp. 1442-1451.

[67] Nguyen M, Hewitt N, Huang M., 2007. Performance evaluation of an air source heat pump using economized vapor injection compressor and flash tank coupled with capillary tubes. In: Proceedings of 22nd International Congress of Refrigeration, Beijing, China, ICR07-E2-1110.

[68] Heo, J., Jeong, M.W. and Kim, Y., 2010. Effects of flash tank vapor injection on the heating performance of an inverter-driven heat pump for cold regions. International Journal of Refrigeration, 33(4), pp. 848-855.

[69] Ma, G.Y. and Zhao, H.X., 2008. Experimental study of a heat pump system with flash-tank coupled with scroll compressor. Energy and Buildings, 40(5), pp.697-701.

[70] Heo, J., Jeong, M.W., Baek, C. and Kim, Y., 2011. Comparison of the heating performance of air-source heat pumps using various types of refrigerant injection. International Journal of Refrigeration, 34(2), pp. 444-453.

[71] Ko, Y., Park, S., Jin, S., Kim, B. and Jeong, J.H., 2013. The selection of volume ratio of two-stage rotary compressor and its effects on air-to-water heat pump with flash tank cycle. Applied Energy, 104, pp. 187-196.

[72] Redón, A., Navarro-Peris, E., Pitarch, M., Gonzálvez-Macia, J. and Corberán, J.M., 2014. Analysis and optimization of subcritical two-stage vapor injection heat pump systems. Applied Energy, 124, pp. 231-240.

[73] Qi, H., Liu, F. and Yu, J., 2017. Performance analysis of a novel hybrid vapor injection cycle with subcooler and flash tank for air-source heat pumps. International Journal of Refrigeration, 74, pp. 540-549.

[74] Xu, X., Hwang, Y. and Radermacher, R., 2013. Performance comparison of R410A and R32 in vapor injection cycles. International Journal of Refrigeration, 36(3), pp. 892-903.

[75] Qiao, H., Aute, V. and Radermacher, R., 2015. Transient modeling of a flash tank vapor injection heat pump system – part I: model development. International Journal of Refrigeration, 49, pp. 169-182.

[76] Qiao, H., Xu, X., Aute, V. and Radermacher, R., 2015. Transient modeling of a flash tank vapor injection heat pump system–part II: simulation results and experimental validation. International Journal of Refrigeration, 49, pp. 183-194.

[77] Reynolds, T.W., 1950. Design of the flash tank. Heating and Ventilating, 74-76.

[78] Reynolds, T.W., 1955. Flash tank design. Heating and Ventilating, 96-97.

[79] Lord, R.G., Rabbia, M.R. and Glover, K.J., Carrier Corp, 1997. Flash Tank Economizer. U.S. Patent 5692389.

[80] Hill IV, F.H., Crane, C.C., Buckley, M.L. and Stabley, B.E., York International Corp, 2005. Flash tank economizer refrigeration systems. U.S. Patent, No. 6941769.

[81] Lifson, A., Taras, M.F. and Dobmeier, T.J., Carrier Corp, 2006. Flash tank for heat pump in heating and cooling modes of operation. U.S. Patent, No. 7137270.

[82] Pham, H., Caillat, J.L. and Van Hoose, R., Emerson Climate Technologies Inc, 2007. Flash tank design and control for heat pumps. U.S. Patent, No. 0251256A1.

[83] Pham, H.M., Caillat, J.L.M. and Van Hoose, R.L., Emerson Climate Technologies Inc, 2009. Flash tank design and control for heat pumps. U.S. Patent, No. 7484374.

[84] Wang, B., Shi, W., Han, L. and Li, X., 2009. Optimization of refrigeration system with gas-injected scroll compressor. International Journal of Refrigeration, 32(7), pp. 1544-1554.

[85] Wang, B., Shi, W. and Li, X., 2009. Numerical analysis on the effects of refrigerant injection on the scroll compressor. Applied Thermal Engineering, 29(1), pp.37-46.

[86] Heo, J., Yun, R. and Kim, Y., 2013. Simulations on the performance of a vapor-injection heat pump for different cylinder volume ratios of a twin rotary compressor. International Journal of Refrigeration, 36(3), pp. 730-744.

[87] Park, Y.C., Kim, Y. and Cho, H., 2002. Thermodynamic analysis on the performance of a variable speed scroll compressor with refrigerant injection. International Journal of Refrigeration, 25(8), pp. 1072-1082.

[88] Li, Y. and Yu, J., 2016. Theoretical analysis on optimal configurations of heat exchanger and compressor in a two-stage compression air source heat pump system. Applied Thermal Engineering, 96, pp. 682-689.

[89] Hwang, Y., Xu, X., Radermacher, R. and Pham, H., 2010. Control strategy of vapor injection cycle. In Proceedings of International Refrigeration and Air Conditioning Conference at Purdue, West Lafayette, p. 2249.

[90] Xu, X., Hwang, Y. and Radermacher, R., 2011. Transient and steady-state experimental investigation of flash tank vapor injection heat pump cycle control strategy. International Journal of Refrigeration, 34(8), pp. 1922-1933.

[91] Bansal, P.K. and Jain, S., 2007. Cascade systems: past, present, and future. ASHRAE Transactions, 113, p. 245.

[92] Kim, D.H., Park, H.S. and Kim, M.S., 2013. Optimal temperature between high and low stage cycles for R134a/R410A cascade heat pump based water heater system. Experimental Thermal and Fluid Science, 47, pp.172-179.

[93] Kim, D.H. and Kim, M.S., 2014. The effect of water temperature lift on the performance of cascade heat pump system. Applied Thermal Engineering, 67(1-2), pp.273-282.

[94] Lee, T.S., Liu, C.H. and Chen, T.W., 2006. Thermodynamic analysis of optimal condensing temperature of cascade-condenser in CO2/NH3 cascade refrigeration systems. International Journal of Refrigeration, 29(7), pp. 1100-1108.

[95] Bingming, W., Huagen, W., Jianfeng, L. and Ziwen, X., 2009. Experimental investigation on the performance of NH3/CO2 cascade refrigeration system with twin-screw compressor. International Journal of Refrigeration, 32(6), pp. 1358-1365.

[96] Dopazo, J.A., Fernández-Seara, J., Sieres, J. and Uhía, F.J., 2009. Theoretical analysis of a CO2–NH3 cascade refrigeration system for cooling applications at low temperatures. Applied Thermal Engineering, 29(8-9), pp. 1577-1583.

[97] Krstić, M. and Wang, H.H., 2000. Stability of extremum seeking feedback for general nonlinear dynamic systems. Automatica, 36(4), pp. 595-601.

[98] Ghaffari, A., Krstić, M. and NešIć, D., 2012. Multivariable Newton-based extremum seeking. Automatica, 48(8), pp.1759-1767.

[99] Mu, B., 2015. Self-optimizing control for building ventilation and air conditioning systems. Ph. D. Thesis, The department of mechanical engineering at University of Texas at Dallas.

[100] Xiao, Y., Li, Y. and Seem, J.E., 2014. Multi-variable extremum seeking control for mini-split air-conditioning system. In Proceedings of International Refrigeration and Air Conditioning Conference at Purdue, West Lafayette, p. 2508.

[101] Krstić, M., 2000. Performance improvement and limitations in extremum seeking control. Systems & Control Letters, 39(5), pp.313-326.

[102] Leblanc, M., 1922. Sur l'electrification des chemins de fer au moyen de courants alternatifs de frequence elevee. Revue générale de l'électricité, 12(8), pp. 275-277.

[103] Draper, C.S. and Li, Y.T., 1951. Principles of Optimizing Control Systems and An Application to The Internal Combustion Engine. American Society of Mechanical Engineers.

[104] Frey, A.L., Deem, W.B. and Altpeter, R.J., 1966. Stability and optimal gain in extremum-seeking adaptive control of a gas furnace. In Proceedings of the Third IFAC World Congress, London, p. 48A.

[105] Jacobs, O.L.R. and Shering, G.C., 1968, January. Design of a single-input sinusoidal-perturbation extremum-control system. In Proceedings of the Institution of Electrical Engineers (Vol. 115, No. 1, pp. 212-217). IET Digital Library.

[106] K. J. Åström and B. Wittenmark, Adaptive Control, 2nd ed., New Jersey: Prentice Hall, 1995.

[107] Ariyur, K.B. and Krstic, M., 2003. Real-time optimization by extremum-seeking control. John Wiley & Sons.

[108] Rotea, M.A., 2000, June. Analysis of multivariable extremum seeking algorithms. In Proceedings of the 2000 American Control Conference, Chicago, pp. 433-437.

[109] Walsh, G.C., 2000, June. On the application of multi-parameter extremum seeking control. In Proceedings of the 2000 American Control Conference, Chicago, pp. 411-415.

[110] Scheinker, A. and Krstić, M., 2014. Extremum seeking with bounded update rates. Systems & Control Letters, 63, pp. 25-31.

[111] Guay, M. and Dochain, D., 2015. A time-varying extremum-seeking control approach. Automatica, 51, pp. 356-363.

[112] Gelbert, G., Moeck, J.P., Paschereit, C.O. and King, R., 2012. Advanced algorithms for gradient estimation in one-and two-parameter extremum seeking controllers. Journal of Process Control, 22(4), pp. 700-709.

[113] Moase, W.H. and Manzie, C., 2011. Semi-global stability analysis of observer-based extremum-seeking for Hammerstein plants. IEEE Transactions on Automatic Control, 57(7), pp. 1685-1695.

[114] Dürr, H.B., Stanković, M.S., Ebenbauer, C. and Johansson, K.H., 2013. Lie bracket approximation of extremum seeking systems. Automatica, 49(6), pp.1538-1552.

[115] Guay, M. and Dochain, D., 2017. A proportional-integral extremum-seeking controller design technique. Automatica, 77, pp.61-67.

[116] Li, Y. and Seem, J.E., 2012. Extremum seeking control with actuator saturation control. U.S. Patent 8200345.

[117] Li, P., Li, Y. and Seem, J.E., 2010. Efficient operation of air-side economizer using extremum seeking control. ASME Journal of Dynamic Systems, Measurement, and Control, 132(3), p. 031009.

[118] Tan, Y., Li, Y. and Mareels, I.M., 2013. Extremum seeking for constrained inputs. IEEE Transactions on Automatic Control, 58(9), pp. 2405-2410.

[119] Kutadinata, R.J., Moase, W.H. and Manzie, C., 2014. Dither re-use in Nash equilibrium seeking. IEEE Transactions on Automatic Control, 60(5), pp. 1433-1438.

[120] Poveda, J. and Quijano, N., 2013, June. Distributed extremum seeking for real-time resource allocation. In 2013 American Control Conference, Washington, pp. 2772-2777.

[121] Dougherty, S. and Guay, M., 2014, December. Extremum-seeking control of distributed systems using consensus estimation. In 53rd IEEE Conference on Decision and Control, Los Angeles, pp. 3450-3455.

[122] Poveda, J.I. and Quijano, N., 2015. Shahshahani gradient-like extremum seeking. Automatica, 58, pp. 51-59.

[123] Azar, F.E., Perrier, M. and Srinivasan, B., 2011. A global optimization method based on multi-unit extremum-seeking for scalar nonlinear systems. Computers & Chemical Engineering, 35(3), pp. 456-463.

[124] Khong, S.Z., Nešić, D., Tan, Y. and Manzie, C., 2013. Unified frameworks for sampled-data extremum seeking control: global optimisation and multi-unit systems. Automatica, 49(9), pp. 2720-2733.

[125] Leyva, R., Alonso, C., Queinnec, I., Cid-Pastor, A., Lagrange, D. and Martinez-Salamero, L., 2006. MPPT of photovoltaic systems using extremum-seeking control. IEEE Transactions on Aerospace and Electronic Systems, 42(1), pp. 249-258.

[126] Yamanaka, O., Onishi, Y., Namba, R., Obara, T. and Hiraoka, Y., 2017. A total cost minimization control for wastewater treatment process by using extremum seeking control. Water Practice and Technology, 12(4), pp. 751-760.

[127] Tehrani, R.D., Shabani, F., 2017. Performance improvement of fuel cells using perturbation-based extremum seeking and model reference adaptive control. Asian Journal of Control, 19(6), pp. 2178-2191.

[128] Matveev, A.S., Hoy, M.C. and Savkin, A.V., 2014. 3D environmental extremum seeking navigation of a nonholonomic mobile robot. Automatica, 50(7), pp. 1802-1815.

[129] Dinçmen, E., Güvenç, B.A. and Acarman, T., 2012. Extremum-seeking control of ABS braking in road vehicles with lateral force improvement. IEEE Transactions on Control Systems Technology, 22(1), pp. 230-237.

[130] Brunton, S.L., Fu, X. and Kutz, J.N., 2013. Extremum-seeking control of a mode-locked laser. IEEE Journal of Quantum Electronics, 49(10), pp. 852-861.

[131] Guay, M., Dochain, D. and Perrier, M., 2004. Adaptive extremum seeking control of continuous stirred tank bioreactors with unknown growth kinetics. Automatica, 40(5), pp. 881-888.

[132] Creaby, J., Li, Y. and Seem, J.E., 2009. Maximizing wind turbine energy capture using multivariable extremum seeking control. Wind Engineering, 33(4), pp. 361-387.

[133] Yang, Z., Li, Y. and Seem, J.E., 2015. Optimizing energy capture of cascaded wind turbine array with nested-loop extremum seeking control. ASME Journal of Dynamic Systems, Measurement, and Control, 137(12), p.121010.

[134] Li, Y., Rotea, M.A., Chiu, G.C., Mongeau, L.G. and Paek, I.S., 2005. Extremum seeking control of a tunable thermoacoustic cooler. IEEE Transactions on Control Systems Technology, 13(4), pp.527-536.

[135] Sane, H.S., Haugstetter, C. and Bortoff, S.A., 2006, June. Building HVAC control systems-role of controls and optimization. In 2006 American Control Conference, Minneapolis, pp. 1121-1126.

[136] Seem, J.E., Johnson Controls Technology Co., 2010. Adaptive real-time optimization control. U.S. Patent 7,827,813.

[137] Li, P., Li, Y. and Seem, J.E., 2010. Efficient operation of air-side economizer using extremum seeking control. Journal of Dynamic Systems, Measurement, and Control, 132(3), p. 031009.

[138] Mu, B., Li, Y. and Seem, J.E., 2014. Experimental study on extremum seeking control for efficient operation of air-side economizer. In International High Performance Buildings Conference, West Lafayette, No. 127.

[139] Gall, J. and Fisher, D.E., 2016. Minimization of unitary air-conditioning system power with real-time extremum seeking control. Science and Technology for the Built Environment, 22(1), pp. 75-86.

[140] Li, X., Li, Y., Seem, J.E. and Li, P., 2013. Dynamic modeling and self-optimizing operation of chilled water systems using extremum seeking control. Energy and Buildings, 58, pp. 172-182.

[141] Mu, B., Li, Y. and Seem, J.E., 2013. Comparison of several self-optimizing control methods for efficient operation for a chilled water plant. In Proceedings of ASME 2013 Dynamic Systems and Control Conference, California, V002T25A006.

[142] Mu, B., Li, Y., Hu, B. and Seem, J.E., 2014. A multi-variable Newton-based extremum seeking control for a chilled water plant with variable water and air flow. In Proceedings of ASME 2014 Dynamic Systems and Control Conference, San Antonio, V002T21A005.

[143] Mu, B., Li, Y., Salsbury, T.I. and House, J.M., 2015. Extremum seeking based control strategy for a chilled-water plant with parallel chillers. In Proceedings of ASME 2015 Dynamic Systems and Control Conference, Columbus, V002T29A005.

[144] Mu, B., Li, Y., House, J.M. and Salsbury, T.I., 2017. Real-time optimization of a chilled water plant with parallel chillers based on extremum seeking control. Applied Energy, 208, pp. 766-781.

[145] Burns, D. and Laughman, C., 2012. Extremum seeking control for energy optimization of vapor compression systems. In Proceedings of International Refrigeration and Air Conditioning Conference at Purdue, West Lafayette, p. 2192.

[146] Weiss, W.K., Burns, D.J. and Guay, M., 2014. Real-time optimization of MPC setpoints using time-varying extremum seeking control for vapor compression machines. In Proceedings of International Refrigeration and Air Conditioning Conference at Purdue, West Lafayette, p. 2273.

[147] Dong, L., Li, Y., Mu, B. and Xiao, Y., 2015. Self-optimizing control of air-source heat pump with multivariable extremum seeking. Applied Thermal Engineering, 84, pp. 180-195.

[148] Koeln, J.P. and Alleyne, A.G., 2014. Optimal subcooling in vapor compression systems via extremum seeking control: theory and experiments. International Journal of Refrigeration, 43, pp. 14-25.

[149] Hu, B., Li, Y., Cao, F. and Xing, Z., 2015. Extremum seeking control of COP optimization for air-source transcritical CO2 heat pump water heater system. Applied Energy, 147, pp.361-372.

[150] Hu, B., Li, Y., Wang, R.Z., Cao, F. and Xing, Z., 2018. Real-time minimization of power consumption for air-source transcritical CO2 heat pump water heater system. International Journal of Refrigeration, 85, pp. 395-408.

[151] Guay, M. and Burns, D.J., 2014, June. A comparison of extremum seeking algorithms applied to vapor compression system optimization. In 2014 American Control Conference, Portland, pp. 1076-1081.

[152] Tiller, M. ed., 2012. Introduction to Physical Modeling with Modelica. Springer Science & Business Media.

[153] Fritzson, P., 2010. Principles of object-oriented modeling and simulation with Modelica 2.1. John Wiley & Sons.

[154] Li, P., Li, Y., Seem, J.E., Qiao, H., Li, X. and Winkler, J., 2014. Recent advances in dynamic modeling of HVAC equipment. Part 2: Modelica-based modeling. HVAC&R Research, 20(1), pp.150-161.

[155] Li, P., Qiao, H., Li, Y., Seem, J.E., Winkler, J. and Li, X., 2014. Recent advances in dynamic modeling of HVAC equipment. Part 1: Equipment modeling. HVAC&R Research, 20(1), pp.136-149.

[156] Li, P., Li, Y. and Seem, J.E., 2010. Modelica-based dynamic modeling of a chilled-water cooling coil. HVAC&R Research, 16(1), pp.35-58.

[157] Li, P., Li, Y. and Seem, J.E., 2010. Modelica based dynamic modeling of water-cooled centrifugal chillers. In Proceedings of International Refrigeration and Air Conditioning Conference at Purdue, West Lafayette, p. 2316.

[158] Li, P., Li, Y. and Seem, J.E., 2012. Consistent initialization of system of differential-algebraic equations for dynamic simulation of centrifugal chillers. Journal of Building Performance Simulation, 5(2), pp.115-139.

[159] Mortada, S., Zoughaib, A., Clodic, D. and Arzano-Daurelle, C., 2012. Dynamic modeling of an integrated air-to-air heat pump using Modelica. international journal of refrigeration, 35(5), pp.1335-1348.

[160] Qiao, H., Aute, V. and Radermacher, R., 2012. Comparison of equation-based and non-equation-based approaches for transient modeling of a vapor compression cycle. In Proceedings of International Refrigeration and Air Conditioning Conference at Purdue, West Lafayette, p. 2190.

[161] Gall, J., Fisher, D.E., Corti, G., Marelli, S. and Cremaschi, L., 2015. Modeling of R-410A variable capacity compressor with Modelica and experimental validation. International Journal of Refrigeration, 58, pp.90-109.

[162] Tian, W., Sevilla, T.A., Zuo, W. and Sohn, M.D., 2017. Coupling fast fluid dynamics and multizone airflow models in Modelica Buildings library to simulate the dynamics of HVAC systems. Building and Environment, 122, pp.269-286.

[163] Zhou, G., Ye, Y., Wang, J., Zuo, W., Fu, Y. and Zhou, X., 2018. Modeling air-to-air plate-fin heat exchanger without dehumidification. Applied Thermal Engineering, 143, pp.137-148.

[164] Van Kenhove, E., De Backer, L., Janssens, A. and Laverge, J., 2019. Simulation of Legionella concentration in domestic hot water: comparison of pipe and boiler models. Journal of Building Performance Simulation, pp.1-25.

[165] Pfafferott, T. and Schmitz, G., 2004. Modelling and transient simulation of CO2-refrigeration systems with Modelica. International Journal of Refrigeration, 27(1), pp.42-52.

[166] Schulze, C., Gräber, M., Huhn, M. and Grätz, U., 2011, June. Real-time simulation of vapor compression cycles. In Proceedings of the 8th International Modelica Conference at Technical University, Dresden Germany, pp. 48-55.

[167] Skoglund, T., Årzén, K.E. and Dejmek, P., 2006. Dynamic object-oriented heat exchanger models for simulation of fluid property transitions. International Journal of Heat and Mass Transfer, 49(13-14), pp.2291-2303.

[168] Li, X., Li, Y. and Seem, J.E., 2010. Dynamic modeling of mechanical draft counter-flow wet cooling tower with Modelica. Proceedings of SimBuild, 4(1), pp.193-200.

[169] Wetter, M., 2009. Modelica-based modelling and simulation to support research and development in building energy and control systems. Journal of Building Performance Simulation, 2(2), pp.143-161.

[170] Wetter, M., Bonvini, M. and Nouidui, T.S., 2016. Equation-based languages–A new paradigm for building energy modeling, simulation and optimization. Energy and Buildings, 117, pp.290-300.

[171] Delgoshaei, P., Heidarinejad, M. and Austin, M.A., 2017. Semantic Inference-Based Control Strategies for Building HVAC Systems Using Modelica-Based Physical Models. Procedia Engineering, 205, pp.1975-1982.

[172] Eborn, J., 2001. On model libraries for thermo-hydraulic applications. Doctoral dissertation. Department of Automatic Control, Lund Institute of Technology, Lund, Sweden.

[173] Tummescheit, H., 2002. Design and implementation of object-oriented model libraries using modelica. Doctoral dissertation, Department of Automatic Control, Lund Institute of Technology, Lund, Sweden.

[174] Modelon. 2013. Solutions for Systems Modeling, Simulation and Optimization. http://www.modelon.com.

[175] Casella, F., Otter, M., Proelss, K., Richter, C. and Tummescheit, H., 2006. The Modelica Fluid and Media library for modeling of incompressible and compressible thermo-fluid pipe networks. In Proceedings of the 5th Modelica Conference, Vienna, pp. 631-640.

[176] Videla, J.I. and Lie, B., 2006. A new energy building simulation library. In Proceedings 3rd Modelica Conference, Vienna.

[177] Ljubijankic, M., Nytsch-Geusen, C. and Unger, S., 2009. Modelling of complex thermal energy supply systems based on the Modelica-Library FluidFlow. In Proceedings of the 7th International Modelica Conference, Como Italy, pp. 335-340.

[178] Lawrence Berkeley National Laboratory. 2019. Modelica Building Library: open source library for building energy and control systems. https://simulationresearch.lbl.gov/modelica/.

[179] The Modelica Assocaition 2019, Modelica standard Library. https://www.modelica.org.

[180] DLR Institute of System Dynamics and Control, 2017. Multi-criteria Optimization Library. https://www.dlr.de/sr.

[181] Pfeiffer, A., 2012. Optimization library for interactive multi-criteria optimization tasks. In Proceedings of the 9th International Modelica Conference. Munich, Germany, pp. 669-679.

[182] Gill, P.E. and Wong, E., 2012. Sequential quadratic programming methods. In Mixed integer nonlinear programming (pp. 147-224). Springer, New York, NY.

[183] Collier, J.G. and Thome, J.R., 1994. Convective Boiling and Condensation. Clarendon Press.

[184] Shah, M.M., 1979. A general correlation for heat transfer during film condensation inside pipes. International Journal of Heat and Mass Transfer, 22(4), pp.547-556.

## BIOGRAPHICAL SKETCH

Wenyi Wang was born in Shaanxi, China. He received his Bachelor of Science degree in Mechanical Engineering from Xi’an University of Architecture and Technology, Xi’an, China in 2007. He was admitted to the School of Energy and Power Engineering at Xi’an Jiaotong University in 2009, where he received his Master of Science degree in Mechanical Engineering in 2012. Then he worked as a HVAC designer in China Northwest Architecture Design and Research Institute Co. Ltd from 2012 to 2015. Since June 2016, he has been a PhD student in Mechanical Engineering at The University of Texas at Dallas. His research interests include control, optimization and dynamical modeling for air source heat pumps and HVAC systems.

**CURRICULUM VITAE**

Wenyi Wang wxw161230@utdallas.edu

**EDUCATION**

**The University of Texas at Dallas** **Richardson, Texas, USA**

*PhD, Mechanical Engineering* *June 2016 – December 2019*

*Supervisor: Prof. Yaoyu Li*

**Xi'an Jiaotong University** **Xi`an, China**

*Master, Refrigeration Engineering* *September 2009 – July 2012*

*Supervisor: Prof. Feng Cao*

**Xi'an University of Architecture and Technology** **Xi`an, China**

*Bachelor, HVAC* *September 2003 – July 2007*

**RESEARCH PROJECTS**

**HVAC system and equipment modeling & efficiency optimization**

*Supervisor: Prof. Yaoyu Li* *June 2016 – August 2019*

- HVAC system and equipment modeling with the Medolica in the Dymola platform. Including air source heat pump, air-handling unit and chiller plant.
- The energy efficiency optimization of the above modeling with Extremum Seeking Control (ESC) and Model Predictive Control.

**PUBLICATIONS** *June 2016 – August 2019*

- **Wang W**, Li Y, Cao F. Extremum seeking control for efficient operation of an air-source heat pump water heater with internal heat exchanger cycle vapor injection. International Journal of Refrigeration 2019;99:153-165.
- **Wang W**, Li Y. Intermediate pressure optimization for two-stage air-source heat pump with flash tank cycle vapor injection via extremum seeking. Applied Energy 2019;238:612-626.
- **Wang W**, Li Y, Cao F. Real-time Optimization of Vapor-Injection Air-Source Heat Pump based Water Heating with Extremum Seeking. 2018 ASHRAE annual conference. Houston, TX.

- **Wang W**, Li Y. Extremum Seeking Control for an Air-source Heat Pump Water Heating System with Flash Tank Cycle based Vapor Injection. 2018 Purdue international refrigeration and air conditioning conference. West Lafayette, IN.
- **Wang W**, Li Y. Real-time optimization of intermediate temperature for a cascade heat pump via extreme seeking. Proceedings of the 13th International Modelica Conference 2019, Regensburg, Germany.

**WORK EXPERIENCE**

**China Northwest Architecture Design and Research Institute Co. Ltd**

*HVAC designer* *July 2012 –July 2015, Xi`an, China*

- HVAC system design for large commercial and residential buildings.

**CERTIFICATE**

- Registered National Utility Professional Engineer (HVAC) in China